A Non-Radial Oscillation Model for Radio Pulsars

by

Rachel Rosen

A dissertation submitted to the faculty of the University of North Carolina at Chapel Hill in partial fulfillment of the requirements for the degree of Doctor of Philosophy in the Department of Physics & Astronomy.

Chapel Hill

2007

Approved by:

Dr. J. Christoper Clemens, Advisor
Dr. Wayne Christensen, Reader
Dr. Charles Evans, Reader
Dr. Robert McMahan, Reader
Dr. Dan Reichart, Reader
Dr. Sean Washburn, Reader

ABSTRACT
RACHEL ROSEN: A Non-Radial Oscillation Model for Radio Pulsars
(Under the Direction of Dr. J. Christoper Clemens)

We present a non-radial oscillation model that can successfully reproduce
many properties of drifting subpulses in pulsars. By demonstrating the presence
of oscillation modes in pulsars, we hope to pave the way for astroseismology
of neutron stars. This model is an alternative to the drifting spark model of
Ruderman & Sutherland (1975). Our non-radial oscillation model reproduces
pulsar morphology in terms of the total intensity and linear polarization. We
associate the displacement and velocity of the oscillations to two orthogonal
polarization modes. From this, we recreate the Stokes' parameters to model
the intensity, linear polarization, and polarization angle. We use our model to
qualitatively reproduce the behavior of several pulsars, including PSR 1919+21,
PSR 1237+25, and PSR 0809+74. This behavior includes the time-averaged
pulse properties, the individual pulse properties, and the subpulse phase jumps.
In addition, we are able to reproduce the orthogonal polarization modes observed
in most pulsars. We then show that our model can be successfully fit to the data
by conducting a quantitative analysis of PSR 0943+10.

Dedicated to: My parents, Ellen and Isaac.

ACKNOWLEDGMENTS

In the late 1980s and early 1990s, Time-Life books published a series called *Voyage Through the Universe.* As a early teenager at the time, I would scavenge the used book stores and the library for copies of the books. At the time, I was too young to understand all the text and its implications, nor did I have the patience to read each book in its entirety. Yet, the vibrant pictures fascinated me. My interest in astronomy began many years before this, but these books solidified in my mind what was to be the obvious course of my education. The completion of this dissertation marks the culmination of my formal education (at least for the immediate future) and, like most things in my life, I did not accomplish this on my own.

My parents have been a constant source of support, encouragement, and inspiration. My father, a wonderful physicist in his own right, fostered in me a love and interest for science at an early age. After a bout of bronchitis in fifth grade caused me to miss the lecture on atoms, I remember with vivid clarity sitting with my father at the kitchen table, explaining to me about protons, electrons, and neutrons. Many science fairs and high school classes did not diminish his patience for my curiosity, his endless knowledge on any topic (science or otherwise), and his willingness to make time for me whether for homework help (even if I did leave it for the last minute) or to have fun. My mother, at the opposite end of the academic spectrum, enlightened me in literature, reading, and writing, and to my astonishment, I found that I loved this as much as science. To this day, I still prefer reading as a pastime to anything else. She instilled in me, to my chagrin at the time, the rules of proper writing and the necessity of being

articulate, along with the importance of communication and good interpersonal skills. I now recognize the importance of these qualities, and even if I lack them sometimes, I am eternally thankful for her foresight. In addition to their academic contributions to my life, my parents also taught me the value of hard work, the importance of moral values and being honest, the necessity of fun and laughter, and the true meaning of unconditional love.

The transformation from a childhood dream of studying astronomy into a reality occurred in the hands of my advisor and friend, Dr. Chris Clemens. When I first started working for him as an undergraduate, I had no background in astronomy, mediocre grades, and much to prove. But I had a willingness to learn and was eager to work. Chris agreed to take me as a graduate student after I finished my undergraduate degree, and by this time, I knew that he was someone that I worked well with professionally, liked personally, and admired greatly. Near the end of my first year of graduate school, we went one Tuesday evening to Miami Subs to discuss possible projects for my thesis. The question he asked himself – which I will no doubt ask myself at various points in the future – was: if I could work on anything, what would it be? He gave me two options: to continue on his work on pulsations in white dwarf stars or to determine if drifting subpulses in pulsars was evidence of pulsations. Despite his knowing very little about pulsars, and the likelihood of a difficult and possibly unsuccessful road ahead, we tackled this question, and this dissertation was born.

I could not have asked for a better mentor than Chris. He has put as much work into this project as I have, and this dissertation is a product of both of our efforts. He has met my ignorance, my errors, and my frustrations with grace and patience. His enthusiasm is contagious and instead of being tired of pulsars and astronomy after six years of graduate school, I am just as eager as the day I started. He taught me the importance of thinking a logical argument through to its conclusion, playing the devil's advocate, and having moral integrity in all parts of life, scientific or otherwise. On a more personal level, both he and his

wife, Georgie, have welcomed me into their home and have adopted me into their family. The occasional feelings of homesickness and solitude that I experience from being away from my own family are usually eased by time spent with Chris, Georgie, and whichever of their wonderful children happen to be home at the time. I am eternally thankful to Chris and his family for everything they have done for me and words cannot express my gratitude.

Along with Chris, I have had the pleasure of being the student of some fantastic professors. Chuck Evans, in addition to being a valuable advisor in regards to my research, has been a role model for me as a teacher. I have attended every class he taught and enjoyed them all thoroughly. I appreciate his well-organized lectures, his time and patience for his students, his clear explanations, and his devotion to teaching. He has inspired me to be a better student, and hopefully one day, a great teacher. Sean Washburn advised me both academically and personally during my undergraduate years. I am gratefully for his patience and time, and for seeing potential in me, even when I did not.

Through this arduous journey of graduate school, I have relied on my friends for emotional support and to help me grow and mature in other areas not related to science. After living in Chapel Hill for 11 years, my friends have become my family. Even though I have told them repeatedly home much I love them and how important they are to me, it seems fitting that I should acknowledge them here, because without them, I would not have kept my sanity long enough to finish school. Two of my closest friends are in actuality, my family: my sisters, Laura and Emily. Despite time and distance, they know me better than anyone else and no explanations or excuses are ever necessary. Their constant love and support, and their ability to always make me smile, have been a great source of comfort. Sarah Honer has listened to all my triumphs, my disappointments, my struggles, and my joys, and through them all, she has always been full of wisdom and sound advice, and had faith in my abilities, even when I did not. Michelle Manges has supported my body as well as my mind, making sure I ate and slept

as well constantly reminding me by example that hard work and perseverance lead to great rewards. I would also like to express my gratitude to Adam Brooks, Adam Crain, Erika Ceseare, John Daniels, Terri Exum, Rachel Garrison, Toby Helmstetter, Mark Kosiewski, Paul Marshall, Atsuko Negishi, Leslie Prochaska, Kimberlee Shaw, and Sara Williamson.

<div align="right">

Rachel Rosen.

July 13, 2007

</div>

CONTENTS

LIST OF TABLES

LIST OF FIGURES

xiv

xviii

Chapter 1

INTRODUCTION

> *"If some one loves a flower,*
> *of which just one single blossom grows*
> *in all the millions and millions of stars,*
> *it is enough to make him happy*
> *just to look at the stars."*
> Antoine de Saint-Exupéry
> The Little Prince

1.1 Introduction

The short, regular radio signal observed by Jocelyn Bell in 1968 with a telescope at the Mullard Radio Astronomy Observatory was thought at first to be instrumental noise or even "little green men". Anthony Hewish, her advisor and the observatory director, and Bell, after determining the noise was indeed coming from space, published the first detection of the radio pulsar PSR 1919+21 (Hewish et al., 1968), later earning Hewish a Nobel Prize. Interestingly, this is one of several pulsars that has driven our current efforts to develop the nonradial oscillation model presented in this work. The discovery of pulsars was a surprise; while astrophysical theory predicted the existence of neutron stars, the assumption at the time was that neutron stars would be undetectable.

Baade & Zwicky (1934) proposed the idea that the remnants of supernova explosions would be stars consisting of neutrons with high density and small radius and coined the term "neutron stars". This prediction lead to work on theoretical models of neutron stars. Oppenheimer & Volkoff (1939) created models assuming the equation of state for a cold Fermi gas for the stellar interiors and treated the neutrons as if they were behaving under general relativistic gravity rather than Newtonian gravity. Work continued on the equation of state for neutrons (Harrison et al., 1958; Cameron, 1959; Ambartsumyan & Saakyan, 1960; Hamada & Salpeter, 1961; Harrison et al., 1965). Among the properties predicted for neutron stars were that they would be rapidly rotating (Hoyle et al., 1964; Tsuruta & Cameron, 1966) with large magnetic fields (Woltjer, 1964; Hoyle et al., 1964). It also became clear, with advancements in nuclear fusion, that neutron stars, depleted of elements for fusion reactions, would only emit via thermal radiation and thus be too dim to observe unless they were in close proximity to Earth.

The short pulsed signal that was detected by Hewish and Bell indicated that whatever object was producing the signal was fairly small. The emitting region, which has the same angular size as the pulse width (in this case, a few milliseconds or about $20°$), cannot be larger than the distance it takes for light to travel across the emitting region (Gold, 1968). It was later agreed that the radius of a neutron star was about 10 km. Yet pulsars have very high luminosity. A pulsar measured at 400 MHz with a pulse width of $10°$ at 1 kpc with a luminosity of 1 mJy will have a total luminosity on the order of 10^{25} erg s^{-1} (Manchester & Taylor, 1977; Michel, 1991). This seems to be the lower limit; a typical pulsar has radio luminosities in the range of 10^{25} to 10^{29} erg s^{-1} (Melikidze et al., 2000). The natural explanation for such a small object to have such a high luminosity is that it must be radiating coherently (Gold, 1968) with radiation that is beamed along the magnetic field toward the observer (Radhakrishnan & Cooke, 1969).

Prior to the discovery of pulsars, Pacini (1967, 1968) proposed that a neutron star oblique rotator in a dipole magnetic field could be responsible for converting

the rotational energy into electromagnetic radiation and would not only power a supernova remnant, like the Crab nebula, but could increase the expansion of the nebula. But it was Gold (1968) that guessed that the pulsed astronomical objects detected by Bell and Hewish were rotating neutron stars with magnetic fields of about 10^{12} Gauss. Gold (1968) further predicted that the emission of electromagnetic radiation would cause a loss in rotational energy which would result in an increase in pulsation period, and that a bunching mechanism produced the coherent observed emission. He suggested that the pulsed nature of the radio emission from the neutron star was associated with the magnetic field. As the magnetic pole, offset from the rotational axis, swept by an observer's line-of-sight on Earth, they would detect a pulse of radiation (thus the term "pulsar"). Gold (1969) later showed that the energy loss of a pulsar was enough to power the Crab nebula.

1.2   Direct Observations

Pulsars emit extremely regular bursts of radio emission, the length of each burst of emission is called the *pulse window* (Radhakrishnan et al., 1969). The length of time from one pulse window to the next is a measure of the spin period of the pulsar (Drake & Craft, 1968), typically ranging from 0.5-4 seconds. Pulsars generally fall into three categories: normal, millisecond, and young pulsars. These normal, or slow, pulsars are the ones examined in this work. The millisecond pulsars are old, recycled pulsars with spin periods usually less than 10 ms due to the transfer of momentum from a binary companion; these pulsars also have the weakest magnetic field of the three classes of pulsars (Graham-Smith, 2003). The young pulsars, like the Crab and Vela, also tend to have shorter spin periods. While most normal pulsars emit radiation only in the radio frequencies, the young pulsars can emit in the high frequency regime. The Crab pulsar was originally discovered as sporadic radio pulses (Staelin & Reifenstein, 1968); later

it was observed in the optical (Cocke et al., 1969) and gamma (Agrinier et al., 1990) part of the electromagnetic spectrum. Similarly, it took many years for the optical (Wallace et al., 1977) and gamma (Thompson et al., 1975) counterparts to the radio pulses (Large et al., 1968) in the Vela pulsar to be discovered.

For most of these normal pulsars, each pulse window only last a fraction of the spin period, giving it a low duty cycle, usually only 1-5%. However, some radio pulsars have high duty cycles; PSR 0826-34 is observable in the radio frequency for most of its spin period (Manchester et al., 1978; Biggs et al., 1985). In general, the duty cycle increases as the period of the pulsar decreases (Goldreich & Julian, 1969). The substructure within the pulse window can be very complex and varies pulse-to-pulse. Yet the average of many pulses (approximately 100) generates a very stable average shape that is specific to each pulsar and persists over time. The regularity of the pulses is defined by its "Q" value, where $Q = \Delta P/P$ which is typically on the order of 10^{11} (Michel, 1991) Pulsars slow down over time with a time scale of T $= P/\dot{P} = 10^7$ yr, where $\dot{P}$ is about 10^{-15} s s^{-1} (Shapiro & Teukolsky, 1983).

It is regular bursts of radio emission and low duty cycles, along with the elimination of other possibilities, that have lead to the conventional pulsar model consisting of a rapidly rotating neutron star. Rotation and pulsation are the two phenomena that would naturally explain the pulsed emission. If the pulsed emission was due to rotation, either by the rotation of a single star or an eclipsing binary system, the short pulse window would suggest dense, compact objects. However, a single rotating white dwarf star cannot remain intact and have a short enough period to match the observations. The break-up period, calculated by setting the centrifugal acceleration at the stellar surface to the gravitational acceleration, has a minimum of 2.43 seconds, even assuming a maximum central density of 10^8 g cm^{-3}. For the same reason, in binary white dwarf system, the radial distance between the white dwarf and its companion would have to be less than the radius of the white dwarf itself to match a 1 second period. Since white

dwarf stars cannot match the observations, neutron stars remain the only alternative, short of invoking exotic new physics to describe a new type of compact object. A pulsating neutron star at its fundamental frequency, with a density of 10^{14} g cm^{-3}, has too short a period to match the 1 second pulse window. A binary neutron star system with a radii and geometry suitable to produce the observed 1 second periods would also produce large amounts of gravitational waves causing an decrease in pulse period, neither of which are detected. Furthermore, the timescales do not match; a binary neutron star system would have a lifetime much shorter than the observed $P/\dot{P} = 10^7$ (Shapiro & Teukolsky, 1983). Thus, the only remaining plausible explanation is the rotation of a neutron star. The conventional model of a pulsar, discussed in detail in §1.5 consists of a rotating neutron star with a large magnetic field, typically 10^{12} Gauss, which is offset from the rotation axis. Observable emission only occurs from the magnetic pole, and appears as short burst of radiation as the magnetic axis sweeps past Earth's line-of-sight. While this model is generally accepted by the scientific community, other theories exist (Michel, 1991).

Most pulsar models predict a pulsar mass of $1.4 M_\odot$, near the white dwarf Chandrasekhar limit. The star is assumed to be supported by degenerate nuclear matter. The only other obvious candidate to support such a star would be electron degenerate matter. White dwarf stars, even at maximum density, are supported by electron degeneracy (Fowler, 1926), and as mentioned above cannot reproduce the 1 second pulsation observations. Pulsar models supported by nuclear degeneracy have a central density 10^{15} g cm^{-3} (Pandharipande et al., 1976). With this density, a neutron star with a mass of $1.4 M_\odot$, would have a radius of 15 km (Pandharipande et al., 1976). Ostriker & Gunn (1969) successfully created neutron star models with a mass of $1.4 M_\odot$, a radius of 1.2×10^6 cm, and a moment of inertia for the star of 1.4×10^{45} g cm^2. These predictions are dependent on the equation of state used in the neutron star model and have some degree of variation. Direct observations of binary pulsar Hulse-Taylor system

(Taylor et al., 1976) have limited the pulsar mass to $1.4M_\odot$ to $1.9M_\odot$ (Joss & Rappaport, 1976). Further, more recent measurements of many pulsars narrowed the pulsar mass to $1.3M_\odot$ to $1.4M_\odot$ (Thorsett & Chakrabarty, 1999). No direct measurements of pulsar radii have been reported (Shapiro & Teukolsky, 1983).

A distribution of pulsars within the sky show that they mostly lie within the galactic plane (Terzian & Davidson, 1976) indicating the most the observed pulsars are located in our galaxy, although some have been detected as far away as the Large Magellanic Cloud (McCulloch et al., 1983). Only one pulsar is close enough to measure the distance using parallax, PSR 1929+10, and it is 50 parsecs away (Salter et al., 1979). Distances to other pulsars are calculated using the dispersion measure, since the electromagnetic radiation emitted from the pulsar at lower frequencies arrives later than that at higher frequencies. The dispersion characteristics are consistent with other object known galactic objects, further confirming that most observed pulsars lie in our galaxy (Shapiro & Teukolsky, 1983).

1.3   Magnetic Field Strength

Pacini (1967) originally estimated the magnetic field strength based on the collapse of a star with an ordinary magnetic field. Assuming flux conservation, he calculated the magnetic field strength to be related to the radius as $1/R^2$, resulting in a magnetic field of 10^{10} to 10^{14} Gauss. The slowdown of pulsars was discovered in the Crab pulsar (Richards & Comella, 1969), which confirmed the magnetic strength of around 10^{12} Gauss (Gunn & Ostriker, 1969). From the pulsar slowdown, Gunn & Ostriker (1969) also calculated the lifetime of the Crab pulsar. The radio output from the pulsar accounts only a small fraction of the energy loss. Even including emission at other observable frequencies, the radiation loss still does not account for the loss in rotational energy, as measured by $\dot{P}$ (Gunn & Ostriker, 1969). The logical assumption is that the magnetic

field is very large, exhibiting enough torque on the rotating star to slow it down.

The rotational energy loss can be calculated from the moment of inertia I and the period and spindown of the pulsar. The rotational kinetic energy is given by:

$$E = \frac{1}{2}I\Omega^2 \tag{1.1}$$

The energy loss rate is then:

$$\dot{E} = I\Omega\dot{\Omega} \tag{1.2}$$

where $\dot{\Omega}$ can be calculated from the spindown, $\dot{P}$, as: $\dot{\Omega} = -2\pi(\dot{P}/P^2)$. For older pulsars with a period of about 1 second and a $\dot{P}$ of 10^{-15}, the energy loss rate is about 10^{31} erg s^{-1}. The radio luminosity from pulsars is about 10^{25} erg s^{-1}, so the radio luminosity contributes only 10^{-4} percent of the energy loss.

Classically, the energy loss rate can be a magnetic dipole rotating in vacuum will radiate according to the Larmor formula (Gunn & Ostriker, 1969; Shapiro & Teukolsky, 1983):

$$\dot{E} = -\frac{2}{3c^3}|\ddot{\mathbf{m}}|^2 \tag{1.3}$$

where the dipole is at an angle α to the rotation axis:

$$\ddot{\mathbf{m}} = \Omega^2\mathbf{m} = \Omega^2\frac{BR^3\sin\alpha}{2} \tag{1.4}$$

so that:

$$\dot{E} = -\frac{B^2R^6\Omega^4\sin^2\alpha}{6c^3} \tag{1.5}$$

In spite of the 10^6 mismatch between the radio luminosity and total energy loss, theorists normally assume the that neutron star is magnetic dipole rotating in vacuum, dissipating all its energy through radiation, with the usual assumed properties ($R = 10$ km, $B = 10^{12}$ Gauss, $P = 1$ second) then the energy loss rate is about 10^{31} erg s^{-1} (Gunn & Ostriker, 1969). This order of magnitude estimate agrees with the energy loss calculated from the spindown rate of the pulsar, indicating that the estimate of a 10^{12} Gauss magnetic field is a reasonable approximation (Gunn & Ostriker, 1969). Yet, the calculated energy loss of a radiating dipole makes the incorrect assumption that the star is in vacuum (§1.5) and that all the energy loss of the star is due to dipole radiation, which does not correlate with the observed energy loss, where radiation is responsible for only 10^{-4} percent of the energy loss. The energy loss is more accurately calculated from the spindown which is based on observational properties (P, $\dot{P}$) and well-constrained measurements (the mass, radius, and moment of inertia; see §1.2).

While this large amount of energy being radiated away is too low in frequency to be observable, it is enough to power a nebula. In the case of the Crab pulsar, with $P = 0.033$ seconds and $\dot{P} = 10^{-13}$, the energy loss is about 10^{38} erg s^{-1}, which is the amount of energy predicted by Gold (1969) needed to power the Crab nebula.

The characteristic age of the pulsar is given as:

$$\tau = \frac{P}{2\dot{P}} \tag{1.6}$$

1.4   Emission Properties

As discussed in the previous section, pulsars are rotating neutron stars with a very large magnetic field. Because the star and its associated magnetic field are rotating, an electric field is induced at the stellar surface, creating a magneto-sphere (Goldreich & Julian, 1969). The electric potential around the star draws

particles off of the stellar surface and accelerates them along the magnetic field. As the particles are accelerated, they emit radiation, resulting in the observed emission.

The actual emission mechanism for pulsars, the manner in which the particles leave the stellar surface and then radiate coherent radio emission has been, and is still, a matter of theoretical debate. The properties of pulsar emission narrows the field of possible explanations. Pulsar emission is coherent in the radio frequencies, but some pulsars, like the Crab, have also been observed at higher frequencies, from the optical through the gamma ray part of the electromagnetic spectrum. There is no indication that the emission at frequencies higher than the radio is coherent. Romani (1996) shows that curvature and synchrotron radiation in the outer magnetosphere can explain gamma rays and optical through x-rays, respectively. Daugherty & Harding (1996) created simulations which explain the gamma ray production near the polar cap. Furthermore, any pulsar emission mechanism must be able to account for the coherent radio luminosities which range from 10^{25} to 10^{29} erg s^{-1} (Melikidze et al., 2000).

A feature in all relativistic emission mechanisms is the beaming of radiation. The basic features of pulsar emission can be explained by the relativistic outflow of particles from the magnetic polar cap along the magnetic field. The relativistic beaming of radiation is the confinement of radiation along the direction of the magnetic field to a cone (Melrose, 1995). Most of the viable emission mechanisms can explain a host of observational properties, such as radius-to-frequency mapping (see §1.6), smaller substructure (called microstructure) within each pulse, and partial circular polarization (see §1.7). These observational properties do not favor one mechanism over another (Melrose, 1995).

Synchrotron and curvature radiation cannot account for the high radio luminosities in pulsars. Particles moving in a magnetic field produce synchrotron or cyclotron radiation, for relativistic and non-relativistic particles, respectively. Synchrotron radiation is the radiation due to the motion of a charged particle

with circular motion perpendicular to the magnetic field. If the particle also has a parallel component to its velocity, the motion of the particle will be helical, where the radius of the curvature of the motion of the particle is based on its momentum. Sturrock (1971) concluded that charged particles accelerated from the surface of the star will have negligible motion transverse to the magnetic field and thus not produce significant synchrotron radiation. The lifetime of a relativistic electron in a $B = 10^{12}$ Gauss magnetic field is

$$\tau = \frac{8.86x10^8}{B^2\gamma}\text{seconds} \tag{1.7}$$

so lifetime of the particle is negligible; it loses its perpendicular energy instantly (Michel, 1991) and thus cannot emit synchrotron radiation. Furthermore, since the particles do not emit below the fundamental frequency at which the particle moves in their circular motion perpendicular to the magnetic field, $\omega_c(0) = eB/m\gamma$, for a 10^{12} Gauss magnetic field, the minimum energy of a synchrotron photon is 11.5 B keV. Thus the pulsar would not emit radio or optical synchrotron radiation, but only at the x-ray and higher frequencies (Michel, 1991).

Many of the earliest mechanisms to explain the coherent radio emission were based on the bunching of particles emitting due to curvature radiation (Sturrock, 1971; Gunn & Ostriker, 1971; Ruderman & Sutherland, 1975). The bunches of particles are in phase, thus making the radiation due to the curvature of the magnetic field coherent. Curvature radiation is produced from particles moving along a curve parallel to the magnetic field, where the radius of curvature is based on the strength and shape of the magnetic field. Lesch et al. (1998) estimated the power radiated via incoherent curvature radiation by a particle with energy $E = \gamma m_e c^2$:

$$P = \frac{2}{3}\gamma^4\frac{q_e^2 c}{4\pi\epsilon_o R_c^2} \tag{1.8}$$

where R_c is the radius of curvature. The power radiated is inversely proportional to the radius of curvature. Thus the place where the power radiated is the greatest where the radius of curvature is the smallest, specifically at altitudes far from the polar cap. Lesch et al. (1998) shows that incoherent curvature radiation cannot produce both the observed luminosities and the observed pulse width. To match the lowest observed luminosity of 10^{25} erg s^{-1}, the emission region must be 4000 km, which would result in a profile width of about 180 degrees (Lesch et al., 1998), which does not match the typical profile width (or pulse window) of 20-25 degrees.

Melrose (1978) criticizes models which rely on the bunching of particles because none of the models propose a bunching mechanism and because of the rapid dispersion of bunches due to the back-reaction of the emission they produce. Lesch et al. (1998) also dismisses coherent curvature radiation as the source of emission because it does not match the observed emission heights of 10-100 km (Gil, 1983) or the change in the the size of the pulse window as a function of observational frequency.

Masers and antenna mechanisms are an alternative type of coherent emission process. Ginzburg & Zhelezniakov (1975) makes the analogy of the two processes: an antenna is like a tuned LC-circuit for it requires a variable electromotive source while a maser is like a self-excited oscillator (for example, a klystron) as it needs a constant electromotive force to maintain its inverted energy population. The antenna mechanism requires the bunching of particles match the density of particles being emitted and coherence occurs because the particles radiate in phase which each other (Melrose, 1995). However, no mechanism for the bunching of particles has been suggested and the bunches will quickly disperse (Graham-Smith, 2003). Maser mechanisms require an inverted population, where particles overpopulate higher energy levels compared to lower ones, but the phase of the particles is irrelevant (Melrose, 1995). Work has continued on maser (Melrose,

1991; Lyutikov et al., 1999a) and laser (Fung & Kuijpers, 2004) mechanisms with no firm conclusion.

1.5 The Standard Pulsar Model

Radial oscillations and rotation were the first two proposed explanations for the observed pulsed behavior of pulsars. Thorne & Ipser (1968) dismissed the idea of radial oscillations because neutron stars should pulsate about 1000 times a second, rather than the observed 1 second pulse. They did not consider non-radial g-modes (see §1.9), whose higher overtones have a lower frequency. The observations of Radhakrishnan et al. (1969) showed that the measured polarization in successive individual pulses did not change over time, indicating that we view the same part of the magnetic field at each pulse. For a radial oscillation model to explain why we view the same portion of the magnetic field for each spin of the pulsar, either the rotation and pulsation axes are aligned or the magnetic field is stationary to our frame of reference, both of which are unlikely (Radhakrishnan et al., 1969). These observations supported the dismissal of the radial pulsation model.

Goldreich & Julian (1969) presented the aligned rotator model for pulsars as shown in Figure 1.1, which is a description of what causes the pulsing behavior in neutron stars. The model consists of a rapidly rotating neutron star whose rotation and magnetic axis are aligned. The angle α is the offset between the two axes, in this case, it is zero. One of the significant calculations presented by Goldreich & Julian (1969) is that the dipole magnetic field is not in a vacuum, but that a magnetosphere is produced by the strong parallel electric field at the surface of the star. The magnetosphere corotates with the star out as far as the light cylinder, an imaginary cylinder whose boundary is where the velocity of the corotating magnetosphere is equal to the speed of light. The light cylinder is defined as $R_c = c/\Omega$ and is about 10^4 km for a 1 second pulsar (Ruderman
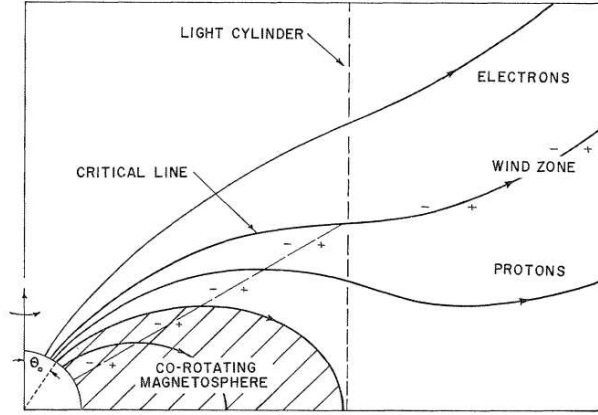
Figure 1.1: The aligned rotator pulsar model as described by Goldreich & Julian (1969). The neutron star has a corotating magnetosphere that extends out to the light cylinder. The parts of the magnetic field near the polar cap do not corotate and extend out into the interstellar medium. The emission we observe is from this part of the magnetosphere.

& Sutherland, 1975). Within the light cylinder, particles are trapped within in the magnetic field and rotate with the star. Outside the light cylinder, particles escape out into the interstellar medium. The electric field potential reaches the same value of that as the interstellar medium at an imaginary line called the critical field line. At small angles between the magnetic pole and the critical line, electrons escape; on the other side of the line, protons escape. The aligned rotator model is a simple model for pulsars because it allows for magnetospheric calculations, like the space charge density which is the number of charges per volume in the magnetosphere (Goldreich & Julian, 1969).

The magnetic polar cap is the part of the stellar surface from which particles freely leave the star. The size of the magnetic polar cap is related to the spin period using Equations 1.9 and 1.10. For a 1 second pulsar with a 10 km radius the angular radius is $\theta_s = 2°$ (Graham-Smith, 2003):

$$\theta_s = (\frac{2\pi r_o}{c})^{1/2} P^{-1/2} \tag{1.9}$$

which translates into a radius of $r_s = 140$ m:

$$r_s = r_o (\frac{\omega r_o}{c})^{1/2} \tag{1.10}$$

However, the aligned rotator model does not actually "pulse" and cannot reproduce pulsar-like behavior. The alignment of the magnetic and rotation axis means that particle emission, which occurs at the magnetic pole, is either always occurring if the rotation/magnetic pole is pointing toward the observer, or never occurring (and is then not observable) if the rotation/magnetic pole is not pointing to the observer. It is the offset in the two axes as shown in Figure 1.2 - an oblique rotator (Mestel, 1971) - that reproduces the pulses, assuming that the magnetic pole points toward Earth at some point in its cycle. Analogously, pulsars are like lighthouses. They rotate on one axis and as the magnetic pole passes across an observer's line-of-sight, the observer receives a flash of radiation. The angle between the magnetic pole and the observer's line-of-sight is the impact parameter, β. Emission at the surface occurs from the magnetic pole out to some distance along the stellar surface, as long as the emitting particles are not trapped within the corotating magnetosphere. Thus, β does not have to be zero for us to observe the pulsar, but it does have to be small enough to keep our viewing window within the emitting region, otherwise the star is not observable. Variations exist on the standard pulsar model but have not been explored as thoroughly as the aligned rotator (Michel, 1991).

The radiation that we observe from pulsars is a function of frequency and is an indication of which part of the magnetic pole we are observing. As the particle travels away from the star along the magnetic field, it emits radiation. What we observe is, in essence, looking down into the radiation cone produced by particles emitting as they move along the magnetic field as illustrated in Figure 1.3. Particles closer to the stellar surface have higher energy and thus emit at higher frequency. The reverse is true for lower frequency observations, which are

14
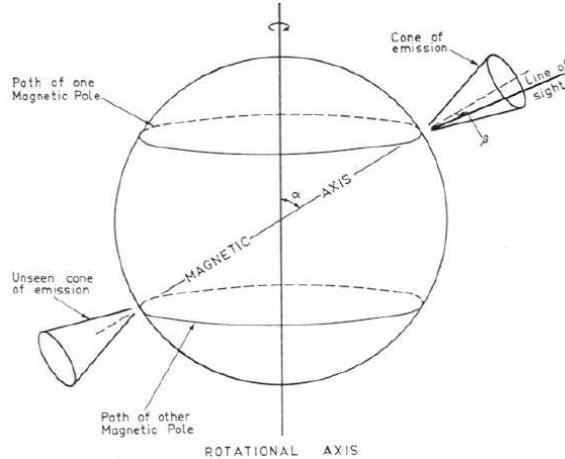
Figure 1.2: Radhakrishnan & Cooke (1969) show an oblique rotator pulsar model where the rotation and magnetic axes are not aligned. Observers receive a flash of radiation each time the magnetic pole sweeps toward Earth.

interpreted to be emission at higher altitudes from the surface.

The mechanisms of what actually occurs at the polar cap was and is still a matter of debate. To preserve charge neutrality, some models propose emission of both positive and negative particles, as in the models suggested by Goldreich & Julian (1969); Sturrock (1971). Goldreich & Julian (1969) proposed that electrons leave the magnetic cap near the magnetic pole (see Figure1.1). Protons leave the stellar surface on the other side of the critical line, which is the imaginary line where the star and its magnetosphere have the same electric potential as the interstellar medium. Sturrock (1971) suggests there are both electron and proton streams of charge that leave each of the polar caps. Particles are accelerated off of the surface due to the electric field as shown in Figure 1.4. The electrons, moving along the magnetic field, produce γ-rays due to the curvature radiation. The γ-rays interact with the magnetic field, producing a cascade of positron-electron pairs. These secondary particles emit the observed radio emission. The protons also create electron-positron pairs, but further out from the stellar surface. The resulting synchrotron emission from the pair-production accounts for the observed optical and x-rays as seen in the Crab pulsar.
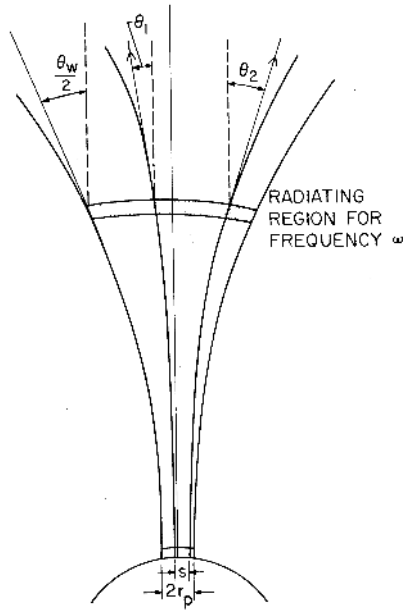
Figure 1.3: The observed radiation of the pulsar is essentially looking down the throat of the open region of the magnetic field down onto the stellar surface. Higher frequency radiation, occurs closer to the stellar surface (Ruderman & Sutherland, 1975).
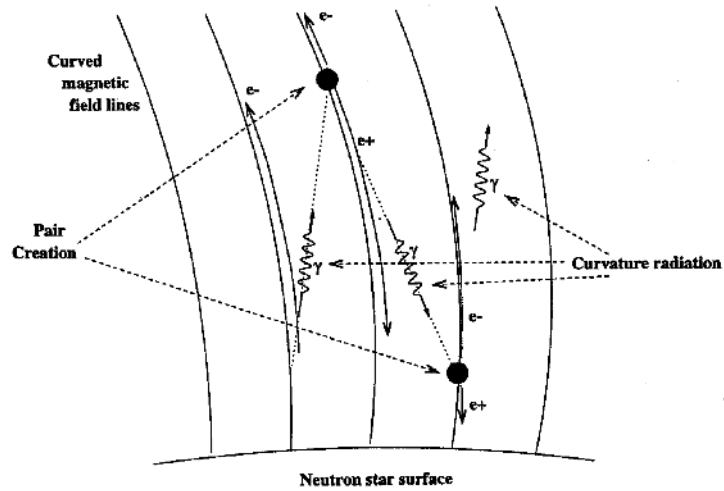
Figure 1.4: The pair-production model introduced by Sturrock (1971) proposes that emission is caused by a secondary cascade of electron-positron production due to an initial particle radiating due to curvature radiation from the magnetic field.

16
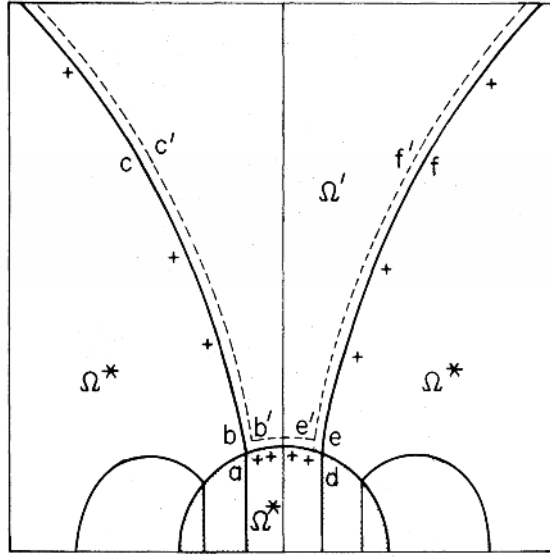
Figure 1.5: The vacuum gap model proposed by Ruderman & Sutherland (1975). A vacuum is created between the stellar surface *ad* and the dashed line as a result of the induced surface electric potential. The region from the equator to *abc* and from the equator to *def* is the corotating magnetosphere. The region bounded by *c'b'e'f'* is the source of the observed emission and rotates at a speed slower than the rotation rate of the star.

Ruderman & Sutherland (1975) furthered this theory by suggesting that that a vacuum ("gap") is formed above the polar cap of about 10^4 cm due to a deletion of charge. As electrons leave the star due to the electric potential created by the magnetic field, a gap forms between the magnetosphere and the stellar surface. Figure 1.5 is a schematic of the vacuum gap of an antipulsar: the magnetic dipole is antiparallel to the spin axis, resulting in positrons leaving the stellar surface rather than electrons. In Figure 1.5, a gap is formed between the stellar surface (*ad*) at the magnetic polar cap and the magnetosphere (*b'e'*). Along with this gap, a gap also occurs between the corotating and non-corotating parts of the magnetosphere. In Figure 1.5, a vacuum gap is formed between the dashed and the dotted lines. The corotating part of the magnetosphere, bounded by the equator and *abc* and the equator and *def*, rotates with the star at an angular speed $\Omega*$. The charged separated portion of the magnetosphere is the

17
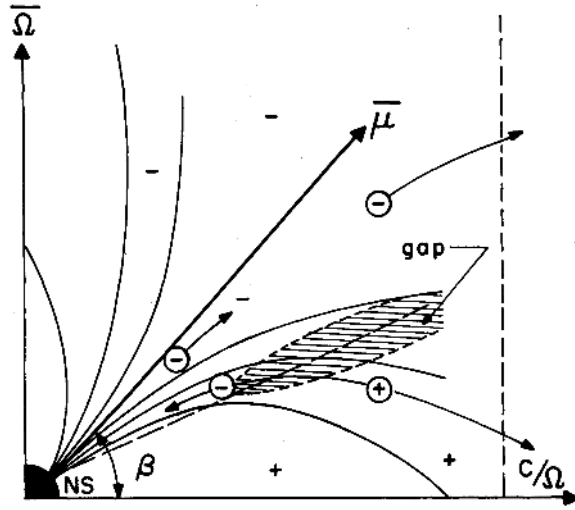
Figure 1.6: Cheng et al. (1976) proposed a current return flow model where parts of the magnetic field that have an electric field close to that of the interstellar medium carry away charges of opposite sign of those leaving the magnetic cap and return charges of the same sign.

cone-shaped region bounded by $c'b'e'f'$. Since charge separated magnetosphere is separated by a gap from the corotating portions of the magnetosphere, it rotates at a slower angular speed Ω'. The gap would grow indefinitely except for "sparking", which is the electron-positron creation that occurs on a millisecond timescale and causes the gap to break down. Ruderman & Sutherland (1975) used the charge separated magnetosphere and the sparking in the vacuum gap to explain the smaller subpulses within the pulse window. The observed drifting subpulses (see §1.8) are smaller pulses which move through the pulse window in a regular fashion. According to the drifting spark model of Ruderman & Sutherland (1975), the smaller subpulses which drift through the pulse window are a result a persistent pattern of circular sparks in the charge separated magnetosphere. Since the circular spark pattern is rotating with an angular speed less than the angular speed of the star, the sparks, which are manifested as subpulses, would drift through the pulse window.

Other models, instead of assuming both positive and negative charges leave

the star, propose that only one charge leaves the star but a return current of opposite charge maintains charge neutrality. Cheng et al. (1976) proposes a model where gaps occur in the magnetosphere, similar to those proposed by Ruderman & Sutherland (1975), above the polar cap near the critical line. If electrons (positrons) are carried away from the star from the regions of the magnetic field that open into space and do not corotate with the star, as shown in Figure 1.6, then the part of the magnetic field that crosses this critical line carry away positrons (electrons) and return electrons (positrons).

1.6   Average Pulse Shapes

Returning to the observational properties that our model must reproduce, we describe here the properties of the average pulse shape. Since each pulse from the pulsar changes in shape and radio luminosity, the average or integrated pulse shape is the average of many successive pulses, usually hundreds to thousands. While the average pulse shape may have several modes, in each mode it is very stable and unique for each pulsar. The width of the average pulse shape combined with the measured spin period gives a measure of the angular size of the star that we are seeing. Typically, for a 1 second pulsar, the pulse width spans about 20° of rotational longitude (Graham-Smith, 2003). The average pulse shapes can have one to five components and can be fitted with a Gaussian curve (Kramer et al., 1994). There are enough similarities in the average pulse shape between different pulsars that they can be classified by the number and location of the components in the average pulse profile. Figure 1.7 from Backer (1976) shows the time-averaged pulse profiles for the most common classification groups based on the number of components: single, double, double unresolved and triple/multiple components. While most of the profiles in Figure 1.7 are symmetrical, some average profiles are asymmetrical. The asymmetry is usually explained by missing components due to weak emission from the star
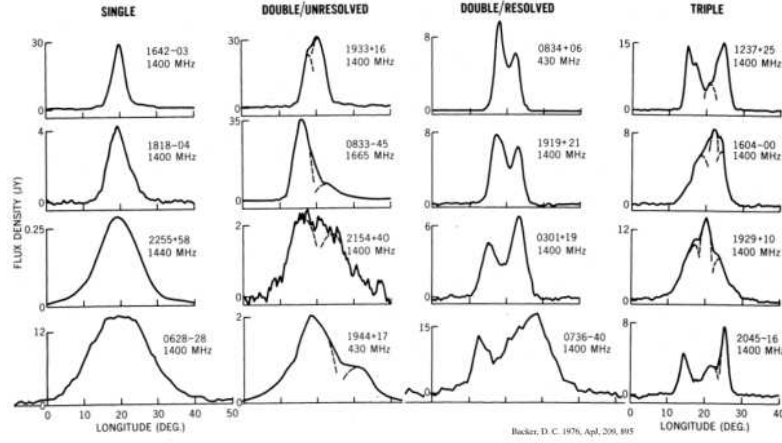
Figure 1.7: The different average pulse shapes classified by Backer (1976).

(Graham-Smith, 2003), an asymmetry in the magnetic field, or an offset between the viewing window and the magnetic polar cap.

To explain the variety of average pulse shapes with a unified model, Komesaroff (1970); Backer (1976) proposed that the magnetic cap was target-shaped: a core surrounded by a hollow cone, which explained the symmetry of the components and their apparent spacing. Single component profiles usually indicate a sightline cut through the core or cone, which one is usually determined by the steepness polarization angle swing (see §1.7,§3). A slice through the core will have a steeper polarization angle swing as the vector that points toward the magnetic pole goes through more degrees of rotation; in Figure 1.8 the core slice would have to have a smaller profile width to show just a single component. A slice through the cone, since it is further from the magnetic pole, will have a shallower polarization angle swing. Other sightline slices through the core or cone, as shown in Figure 1.8 will produce pulse shapes with two or three components. The discovery of profiles with four or five components led to the addition of a second hollow cone (Rankin, 1993a). The lack of pulsars with more than 5 components within an average pulse window of 20° indicates that there cannot be more than two hollow cones, or as we will show in the case of our non-radial os-
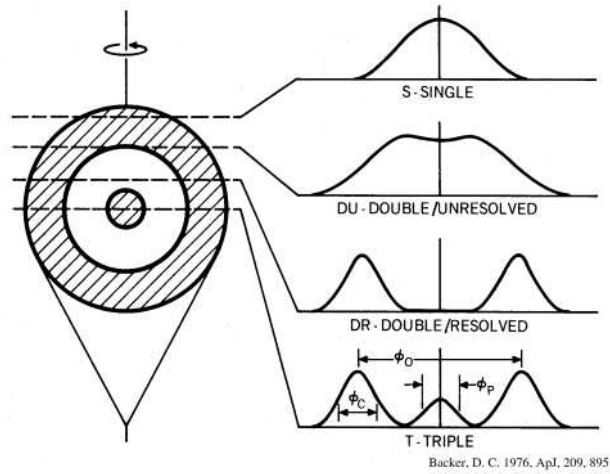
Figure 1.8: Backer (1976) proposed a hollow cone model where different sightline slices through the core and cone reproduced the different average pulse shapes.

cillation model, no more than two nodal regions within the magnetic cap. Lyne & Manchester (1988) showed that the components of pulsar components were randomly distributed in the magnetic cap.

A few pulsars have unique geometries that can be measured precisely and can offer more insight to pulsar behavior, namely pulsars with interpulses and pulsars that are always "on". Pulsars with interpulses, have $\alpha = 90°$ and small β so that both magnetic poles sweep towards Earth. Pulsars such as PSR B1702-19 show that pulse phase between both polar caps is correlated (Weltevrede et al., 2007). Pulsars that are always "on", have very small α and β, so that our line-of-sight wanders around the magnetic pole without ever leaving the emission region (Esamdin et al., 2005).

Furthermore, several geometric effects also take place. The magnetic field becomes more disperse with an increase in distance from the star because of the curvature of the magnetic field. If particles moving along the magnetic field emit radiation at high frequency, they will have radiated near the stellar surface and the angular width of the observed pulse will be closely correlated to the angular
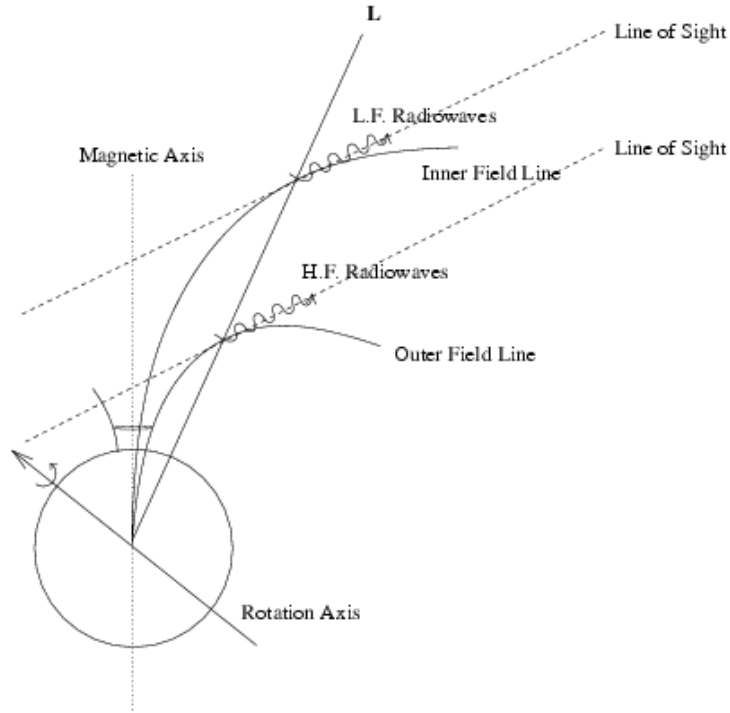
Figure 1.9: While emission at lower frequencies occurs at higher altitudes than emission at high frequencies, lower frequency emission also is associated with emission closer to the magnetic pole in a radial direction (Smits et al., 2006).

size of the emitting region near the stellar surface. If the same particles emit radiation at lower frequency, they will have traveled further along the magnetic field and will emit at a higher altitude. Because the magnetic field is more diffuse at higher altitudes, the observed pulse of radiation emitted at the lower frequency will appear broadened and the angular width of the pulse will have an effective magnification factor compared to the angular size of the stellar surface from where the particles originated.

Multi-frequency measurements, like that of Lyne & Manchester (1988) in Figure 1.10, show this behavior. The profile of PSR 2045+16 at 1420 MHz shows narrower component spacing and sharper components than the same star at 170 MHz. This is true for most of the pulsars in Figure 1.10 and other stars (Rankin et al., 2006) supporting the theory that the lower frequency emission occurs at

higher altitudes than the high frequency emission, and the lower frequency profile is broadened due to a widening and dispersing of the magnetic field.

Even though lower frequency emission occurs at higher altitudes, the part of the magnetic field that emits the low frequency radio waves is closer to the magnetic pole in longitude (Smits et al., 2006). As can be seen in Figure 1.9, the lower frequency radio waves are emitted further from the stellar surface in altitude but closer to the magnetic pole in latitudinal angle than the higher frequency emission. Since our sightline with respect to the magnetic field does not change with observational frequency, the plane of emission remains parallel regardless of the altitude or frequency of emission. More curvature in the magnetic field results in a higher frequency of emission. While the curvature is greatest closest to the stellar surface, it is also furthest in latitude from the magnetic pole. So while high frequency emission more closely correlates with the condition on the stellar surface, low frequency emission is more representative of the conditions at the magnetic pole. Measurements verify this effect: in average pulse shapes, the width of the components and the separation between the components increases with a decrease in observation frequency. The growth of the pulse shapes can be fit with a power law (Thorsett, 1991; Xilouris et al., 1996).

1.7 Polarization Properties

Just as the average pulse shape, calculated from the intensity, is unique for each pulsar, so are its polarization properties. The polarization is measured in three Stokes' parameters: two linear polarizations measured 45° apart (Q and U) and a circular polarization (V). We refer the reader to section §3.3 for a more detailed discussion of the how the polarization is measured. Individual pulses in a pulsar tend to be highly linearly polarized but the linear polarization in average pulse shapes may not have the same degree of polarization. This is because the polarization of individual pulses may average away after many
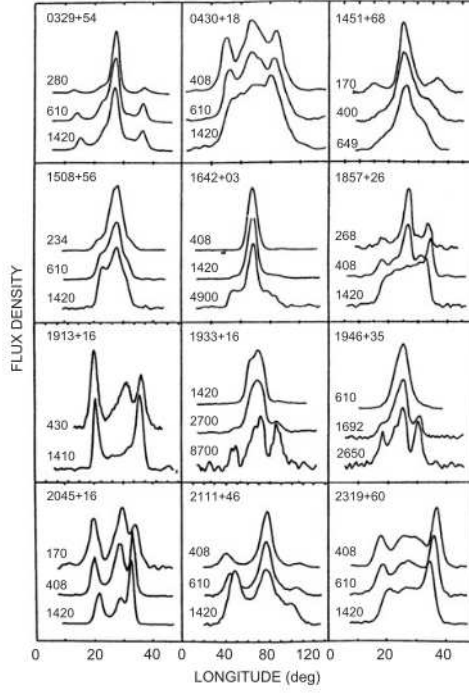
Figure 1.10: The evolution of average pulse shapes at different frequencies (Lyne & Manchester, 1988).

pulses (Michel, 1991). The circular polarization tends not to be as strong as the linear polarization. The circular polarization can change handedness in the center of components and/or at the point that it closest approaches the magnetic pole. PSR 0525+21, a highly polarized double component pulsar shown in Figure 1.11, appears to be only partially linearly polarized and the linear polarization has the same shape as the total intensity. The circular polarization, clearly is not as strong as the linear polarization and changes handedness at about 8° in the component on the right side, but does not have a handedness change in the left component.

The average polarization angle for most pulsars has an S-shaped curve to it, as is obvious in the lower panel of Figure 1.11. The polarization angle is calculated from the two measured linear polarizations, Q and U (see 3.3), and is therefore an indication of the direction of linear polarization. The curve in the
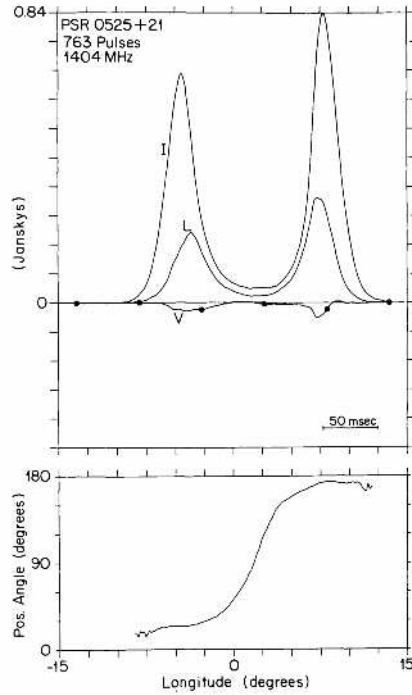
Figure 1.11: Top panel: Average intensity (I), linear (L), and circular (V) polarization of PSR 0525+21. Bottom panel: Average polarization angle (Stinebring et al., 1984a).

polarization angle can be understood according to the single vector model where (Radhakrishnan & Cooke, 1969) define a vector that lies in the plane of curvature of the dipole magnetic field. As the magnetic pole sweeps past our line-of-sight, the vector, which is always pointing toward the magnetic pole, rotates through the pulse window. At the closest approach to the magnetic axis, the vector also points toward the rotation axis. In the special case where our sightline traverses across the magnetic pole, the polarization angle, instead of making a rotation swing, will have a constant polarization angle with a sharp 180° jump when our sightline is directly over the magnetic pole. In this situation, the vector that lies in the plane of curvature always remains parallel to our line-of-sight and points toward the magnetic pole, resulting in a lack of curvature. When our sightline crosses directly over the magnetic pole, the orientation of the vector does not change except for a reversal in sign, which results in a 180° jump in

25

the polarization angle. Therefore, the amount that the polarization swing is less that 180° is an indication of the geometry of the star: the offset between the rotation and magnetic axes (α) and the magnetic axis and our line of sight (impact parameter β). The single vector model describing the polarization angle swing is also referred to as the rotating vector model or the Radhakrishnan & Cooke polarization angle swing.

This single vector model is based on three assumptions: the radiation is beamed tangent to the magnetic field, the polarization angle is aligned to the plane of curvature of the magnetic field, and the magnetic field is a dipole (Hibschman & Arons, 2001). As Radhakrishnan et al. (1969) point out, PSR 0833-45 has a change in polarization angle greater than 45° through a pulse window of only 20°, indicating that the emission must occur near the surface of the star. If emission occurred at high altitudes, the vector swing would not be able to rotate the full 45° degrees through the given pulse window.

Cordes (1978) used the profile widths of different pulsars at various frequencies to place limits on the emission radius from a minimum of few percent of the velocity of light radius to a maximum of 5-10 times the neutron star radius. The shape of the curve is also partially dependent on the viewing geometry, namely the offset between the rotation and magnetic poles, α, and the angle between the magnetic pole and our line of sight β. The steeper the curve, the closer our sightline is radially to the magnetic pole, as discussed in detail in §3.2. The polarization angle in PSR 0525+21 swings through about 150°, indicating that our sightline transverses only 0.7° away from directly crossing the magnetic pole (Lyne & Manchester, 1988).

More detailed information about a pulsar can be gained from examining individual pulses. In addition to the polarization angle swing described by the single vector model, in individual pulses the polarization angle can undergo 90° jumps. Backer et al. (1976) first noticed this phenomena and called it "orthogonal polarization modes". The orthogonal polarization modes represent the superposition
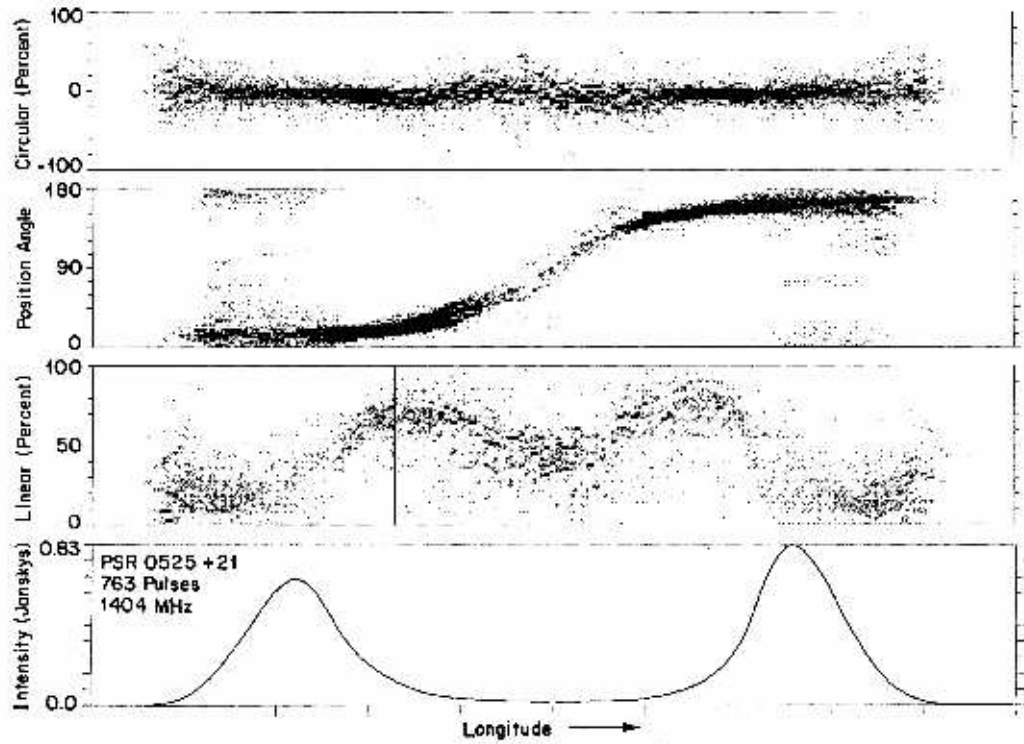
Figure 1.12: Histograms of circular, linear, and polarization angle of PSR 0525+21 (Stinebring et al., 1984a).

of two polarization modes: one polarization mode lies in the plane of curvature of the magnetic field, and the other polarization mode lies perpendicular to the plane of curvature. Since both polarization planes rotate with the magnetic field, they trace the same polarization angle swing through the pulse window, only separated by 90°. In many cases, one polarization mode tends to be more dominant than the other.

The switching between the two orthogonal polarization modes in the individual pulses can be masked in the average pulse shapes, as the average polarization angle follows the angle of the dominant plane. Stinebring et al. (1984a,b) created histograms of the circular, linear, and polarization angles of individual pulses to explore the orthogonal polarization mode switching. Figure 1.12 is of the same data as Figure 1.11 but in histogram form. Several things become quite obvious

when examining the histogram compared to the average profile. The highest linear polarizations in the average profile occur around $-3°$ and $7°$, more or less matching the shape of the total intensity but with the peaks offset. In the polarization angle histogram, the S-shaped curve is quite distinct, but at longitudes corresponding with a maximum in the total average intensity, there appears to be a switching in the polarization angle both $90°$ and $180°$ away from the main polarization angle track. By definition of the polarization angle (see §3.3), a change of $180°$ is meaningless; a polarization angle of $0°$ and $180°$ have the same polarization mode. However, a polarization angle change of $90°$, barely seen in PSR 0525+21, indicates some polarization in a plane orthogonal to the main polarization angle track. Backer et al. (1976) first observed the existence of these two simultaneous orthogonal polarization modes and noted that the sum of the two modes would be depolarization with the polarization angle following the stronger mode (Graham-Smith, 2003). Indeed, the average polarization angle of PSR 0525+21 in Figure 1.11 does not show the second, fainter polarization mode. It is generally accepted that the two modes are orthogonal and that a mixture of the two modes would have the polarization state of the dominant mode (Graham-Smith, 2003). Gil et al. (1992) finds the polarization angle through another method; in the presence of two polarization angle modes, the total intensity, linear, and circular polarization profile are calculated. He finds that the orthogonality of the two modes can deviate as much as $30°$ or more, but this may only apply to cases involving complex profiles and more than one simultaneous (emission) source (Graham-Smith, 2003). In a proper motion study, Johnston et al. (2005) measured the polarization angle at the closest approach to the magnetic pole for 20 pulsars. Of these, half of the pulsars where the polarization angle was within $10°$ of one of the two orthogonal polarization modes, indicating that the rotation vector was aligned to the proper motion vector.
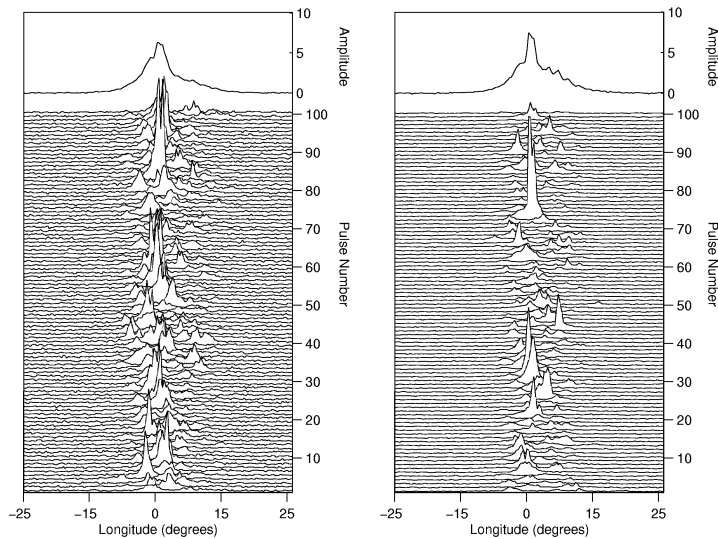
Figure 1.13: Individual pulses and average pulse shape for PSR 0943+10, reproduced from archival data taken by Deshpande & Rankin (2001).

1.8 Drifting Subpulses

Drake & Craft (1968) first observed an system of organized subpulses that move through the pulse window, called drifting subpulses. This phenomena is easily seen in PSR 0943+10 because it has a simple, single component in the average pulse shape. The individual pulses, shown in Figure 1.13 vary wildly in amplitude and shape, but consistently build up a stable average pulse shape. Each panel, left and right, in Figure 1.13 show a hundred successive pulses of PSR 0943+10. Despite the variations in the individual pulses, the average pulse shapes for those two sections of hundred pulses each (top panels of Figure 1.13) are remarkably similar. The individual pulses tend to be highly polarized, although not as obvious in the average linear polarization (dashed line in the top panel of Figure 1.14). The polarization angle histogram clearly shows the two orthogonal polarization modes. The gradual slope of the polarization angle swing, especially as compared to that of PSR 0525+21 in Figure 1.11, indicates the sightline is a least several degrees from the magnetic pole.

29
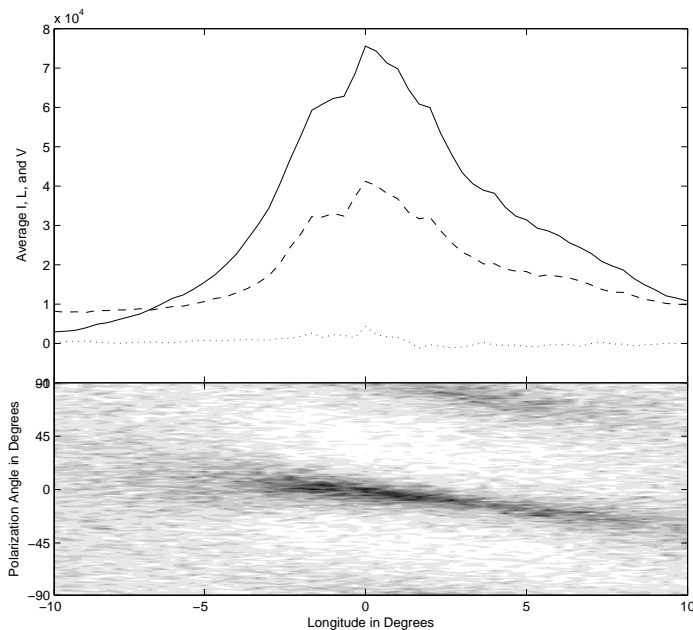
Figure 1.14: Top panel: Average intensity (solid line), linear polarization (dashed line), and circular polarization (dotted line) for PSR 0943+10 at 430 MHz. Bottom panel: Polarization angle histogram.

The drifting subpulses are characterized by three main timescales. The first is the spin period of the pulsar, P_1. Typical of these types of pulsars, the spin period for PSR 0943+10 is 1.097608 seconds. The second is P_2, the spacing in time (represented as longitude in Figure 1.15) between adjacent subpulses within the same pulse, as illustrated in Figure 1.15. Most subpulses have a period around 30 msec, although our own observations have found subpulses in the range of 15-50 msec. The value of P_2 must be incommensurate with P_1 for the subpulses to "drift". The low duty cycle of the pulsars makes it difficult to find an exact period for the subpulses. Pulsars that have at least two subpulses in a pulse window make the problem of determining P_2 more tractable, but the apparent value of P_2 can be highly influenced by the viewing geometry and multiple components in the average pulse profile (see §2). The last parameter is P_3, the time it takes for a subpulse at a given longitude to return to the same
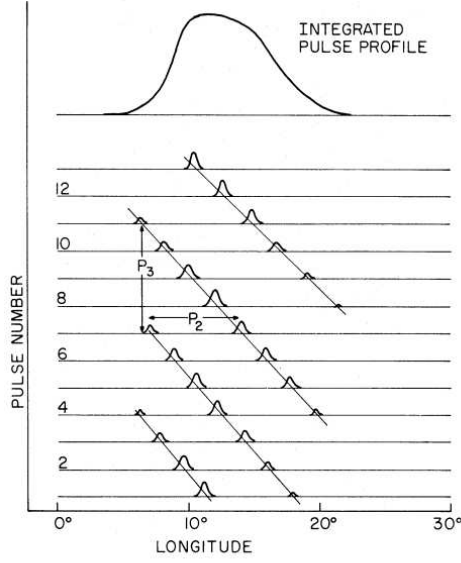
Figure 1.15: Definitions of P_1, P_2, and P_3(Ruderman & Sutherland, 1975).

longitude in subsequent spins of the star.

If P_2 is stable with regular spacing between adjacent subpulses, then the following relationship should hold:

$$\frac{1}{P_3} = \frac{1}{P_2} - \frac{n}{P_1} \qquad (1.11)$$

where n is a integer indicating the number of spins needed for the subpulse to return to its original longitude. In the non-radial oscillation model we will present, P_2 is the oscillation frequency, and is thus required to be a stable underlying clock. The original idea that non-radial oscillation in pulsars could explain the drifting subpulses was discarded because the *apparent* measured value of P_2 was not stable enough to indicate an underlying clock mechanism. In §2, we show that this argument is not valid. The value of P_2 can be extremely stable and regular, but be pulled around by the nodal structure of the star, causing P_2 to *seem* to be irregular even though it is not.

31

In each consecutive spin P_2 changes slightly with longitude and a line drawn through the maximum of each subpulse produces, as in Figure 1.15, a driftband. In Figure 1.15, the subpulses are completely regular and P_2 is stable, so the driftband is a straight line. As mentioned, the structure of the pulse can make P_2 *appear* to wander, creating curvature in the driftband. Two types of curvature are usually observed and the explanation of this curvature in light of our non-radial oscillation model is detailed in Appendix §A.

Most pulsars also display two other, sometimes related, phenomena: mode changes, a change in the subpulse period P_2, and nulls, a cessation of the pulsar emission all together at all frequencies. Mode changes may or may not be accompanied by nulls. The mode changes can be cyclic, rotating though several different values of P_2, as in PSR 0031-07 (Vivekanand & Joshi, 1997). Nulls are a lack of emission, usually defined as 1% below the mean pulse power (Graham-Smith, 2003). Like all other behaviors, nulling varies between pulsars but can be characterized and unique for each pulsar. Some pulsars have nulls that last only two or three pulses for every hundred or so regular pulses (Backer, 1970c). Some nulls can last hours or days (Esamdin et al., 2005) and be in the "null" state longer than the time when the pulsar is emitting. Pulsars that are weak emitters can have undetermined nulling behavior as the signal is so low that individual pulses can not be resolved and only the average pulse shape can be determined for the pulsar (Graham-Smith, 2003). PSR 0809+74 has both mode-changes and nulls. In Figure 1.16, pulses 1 through 140 show a stable P_2, followed by a null. When the subpulses resume, they have a different P_2, as seen by the change in slope of the driftband. Around pulse 280, the subpulse seem to change back to their original value of P_2, but unaccompanied by a null.
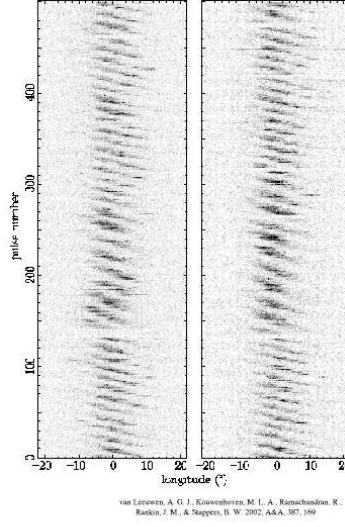
Figure 1.16: Mode changes and nulls in PSR 0809+74 (van Leeuwen et al., 2002)

1.9   Non-radial Oscillation Modes

One of the objectives of this thesis is to account for all the properties of pulsars, particularly drifting subpulses, mentioned in the previous sections using pulsations. To this end, we give a brief description of non-radial oscillation theory, the types of non-radial oscillation modes, and the required stellar conditions for the modes to exist.

Simple stellar models assume stars are in hydrostatic equilibrium: the gravitation pressure exerted inwards toward the stellar core is balanced by the outward pressure from the stellar interior. In variable stars, hydrostatic equilibrium is not maintained due to local motions of the stellar fluid, and in which case the stars can oscillate. The two main oscillation modes are due to the two forces balanced in hydrostatic equilibrium: p-modes in which the restoring force is pressure and g-modes in which the restoring force is gravity. The p-modes are acoustic modes and are related to the speed of sound in the stellar interior. The g-modes are related to the buoyancy force and can be thought of as standing gravity waves. The fundamental radial oscillation frequency is the dynamic timescale, given by

33

1.12 (Hansen & Kawaler, 1994).

$$t_{dyn} = (\frac{R^3}{GM})^{1/2} \tag{1.12}$$

The fundamental frequency and higher frequencies for a given star are p-modes; frequencies lower than the fundamental frequency are g-modes. The fundamental radial oscillation p-mode for the sun is 26.53 minutes and higher frequency 5-minute p-mode oscillations have also been detected. The fundamental mode has no nodes, but the 5-minute oscillation modes have 20-30 nodes in the radial direction (Christensen-Dalsgaard, 2003). White dwarf stars have a fundamental p-modefrequency, according to Equation 1.12 of about 2 seconds. However, they have observed oscillation periods of 3-10 minutes, indicating that the oscillation modes are g-modes.

Non-radial oscillation modes can be characterized by three numbers: l, m, and n. The oscillations on the stellar surface are described by a Legendre polynomial, a function l and m, which determine the nodes (ie. zeros in the Legendre polynomial). The oscillations from the stellar core to the surface can be described by a standing wave with n zeros. Thus, number of nodes from one pole to the other is l, the number of nodes that cross equator is m, and the number of nodes from the center of the star to the surface is n. Non-radial oscillations do not assume axial symmetry is preserved; radial oscillations are a special case of the more general non-radial oscillations.

While we will not delve into the mathematics of non-radial oscillation theory and refer the reader to Hansen & Kawaler (1994) or Christensen-Dalsgaard (2003), suffice it to say that the second order differential equation of the displacement vector of the oscillation, ξ can be given by:

$$\frac{d^2\xi_r}{dr^2} = -K(r)\xi_r \tag{1.13}$$

where

$$K(r) = \frac{\omega^2}{c^2}\left(\frac{N^2}{\omega^2} - 1\right)\left(\frac{S_l^2}{\omega^2} - 1\right) \tag{1.14}$$

The two important frequencies in Equation 1.14 are the buoyancy, or Brunt-Väisälä, frequency, N (Hansen & Kawaler, 1994):

$$N^2 = -g\left[\frac{d\ln\rho}{dr} - \frac{1}{\Gamma_1}\frac{d\ln P}{dr}\right] \tag{1.15}$$

and the acoustic, or Lamb, frequency, S_l:

$$S_l^2 = \frac{l(l+1)}{r^2}\frac{\Gamma_1 P}{\rho} = \frac{l(l+1)}{r^2}v_s^2 \tag{1.16}$$

where

$$\Gamma_1 = \frac{\partial \ln P}{\partial \ln \rho} \tag{1.17}$$

If $\omega^2 > N^2, S_l^2$ or $\omega^2 < N^2, S_l^2$, then $K(r)$ is positive, the solution to Equation 1.13 is oscillatory motion. If $N^2 < \omega^2 < S_l^2$ or $S_l^2 < \omega^2 < N^2$, then $K(r)$ is negative, the solution is either exponentially increasing or decreasing. If the solution is oscillatory, then the solution for Equation 1.13 is:

$$\xi_r \ \cos\left(\int (K^{(1/2)}dr + \phi\right) \tag{1.18}$$

For a given oscillation mode, there may be oscillatory solutions interspersed with exponential solutions. In the regions where the solution is oscillatory, one of the two frequencies (acoustic or buoyancy) dominates and the solution is said to be "trapped". The boundaries of the trapping region are where $K(r) = 0$. As the frequency increases, $K(r)$ increases, and as $K(r)$ increases, so does the number of zeros in Equation 1.18, which characterizes the order of the mode.

For the oscillatory condition $\omega^2 > N^2, S_l{}^2$ the frequency is high, resulting in p-modes where pressure is the restoring force. In this case, $\omega >> N$ and Equation 1.14 becomes

$$K(r) \simeq \frac{1}{c^2}(\omega^2 - S_l{}^2) \tag{1.19}$$

Thus as the mode order increases, so does the frequency and $K(r)$. For dense, compact objects like neutron stars, oscillations of this order have too high a frequency to match the subpulse frequency and an increase in the radial order will only increase the oscillation frequency.

For the oscillatory condition $\omega^2 < N^2, S_l{}^2$, the resulting modes are g-modes are are lower frequency than the p-modes and the restoring force is gravity. These modes are based on the buoyancy frequency. In the stellar interior, if a parcel of fluid is displaced upward adiabatically (ie., there is no heat exchange between the parcel and its surroundings), then the condition for g-modes to take place depends on whether the element is more or less dense than its surroundings. If the parcel is more dense than the fluid it displaces, $N^2 > 0$, the buoyancy force will return the parcel to its original position and the parcel oscillates around its original position. If the parcel is less dense that the fluid it displaces, $N^2 < 0$, the buoyancy force will cause the parcel to keep moving upwards away from equilibrium, creating convective instability (Christensen-Dalsgaard, 2003). The higher the frequency of the g-mode, the deeper it is in the interior of the star. In this case, $\omega << S_l$ and Equation 1.14 becomes:

$$K(r) \simeq \frac{1}{\omega^2}(N^2 - \omega^2)\frac{l(l+1)}{r^2} \tag{1.20}$$

As the frequency ω decreases, $K(r)$ increases. The mode order increases with decreasing ω. Thus for a neutron star, even if the fundamental frequency is much

higher than the subpulse frequency, a higher radial order overtone can match the lower observed subpulse frequency.

1.10   Scope of This Project

The goal of this project is to present a non-radial oscillation model that can successfully reproduce many properties of drifting subpulses in pulsars. This model is an alternative to the drifting spark model of Ruderman & Sutherland (1975) (see §1.5). One advantage of our model is that it can be used quantitatively fit to data, which we describe in Chapter 3. Our non-radial oscillation model is able to reproduce both the time-averaged pulse properties and the individual pulse properties of pulsars. We are able to describe the average pulse profile, which is the average of many consecutive pulses of a star and is unique for each pulsar. Pulsars can have anywhere from 1-5 components in their average pulse profile and the components are usually symmetric about the center of the pulse window, which can be naturally explained in our non-radial oscillation model. The single vector model of Radhakrishnan & Cooke (1969) describes the polarization angle swing as the curve traced by the vector that lies in the plane of curvature of the dipole magnetic field and rotates with the magnetic field as it passes by our line-of-sight. The single vector model seamlessly incorporates into our non-radial oscillation model, as it is a natural part of our model. In addition, we are able to explain the orthogonal polarization modes, which is the presence of two polarization angle swings which are 90° apart. In each consecutive spin of the pulsar, smaller subpulses are present in the pulse window. In some pulsars they drift through the pulse window and in other pulsars they display quasi-stationary behavior. The drift rate of the subpulses is incommensurate with the spin period, and in our model, we explain the drift rate of the subpulses as an oscillation mode. An imaginary line tracing the location of the maximum of each subpulse creates a driftband. In many instances, the drift-

band is not linear and instead has distinct curvature, which we can explain as an interaction between the oscillation mode and nodal structure on the surface of the star (see §2). Furthermore, the subpulses can have a 180° phase jump between adjacent components, a phenomena that is seen in other non-radially oscillating stars and was critical in leading us to the development of the model presented in this work. Some pulsars exhibit mode changes where the subpulse period changes. The mode changes can be cyclic between several periods and can be accompanied by nulls, which are periods of no emission. Mode changes and nulls are also seen in other non-radially oscillating stars and are a natural result of pulsations.

In addition, our model can reproduce some of the unique behavior that is not considered the general trend and is seen only in a few pulsars. If the average pulse shape in some pulsars has multiple components, the slope of the driftband can be different in each of the components. Some pulsars show 180° subpulse phase jump between adjacent components, and other pulsars do not show any subpulse phase jump between components. This distinction is easily explained in our model. In addition, our model can explain those particular instances when the subpulse phase jumps are not 180° apart. We consider our non-radial oscillation model to be successful because it cannot only explain the general properties of pulsars, but also those pulsars whose behavior is not the general trend, and furthermore, our model makes specific, testable predictions of phenomena that we should be able to observe.

1.11   Plan of This Work

The idea of non-radial oscillations in stars is not a new idea. White dwarf stars, rapidly oscillating AP stars, delta Scuti stars, and even our sun are all known to have oscillation modes. Despite this, the suggestion of non-radial oscillations in radio pulsars has been largely ignored. However, when Edwards
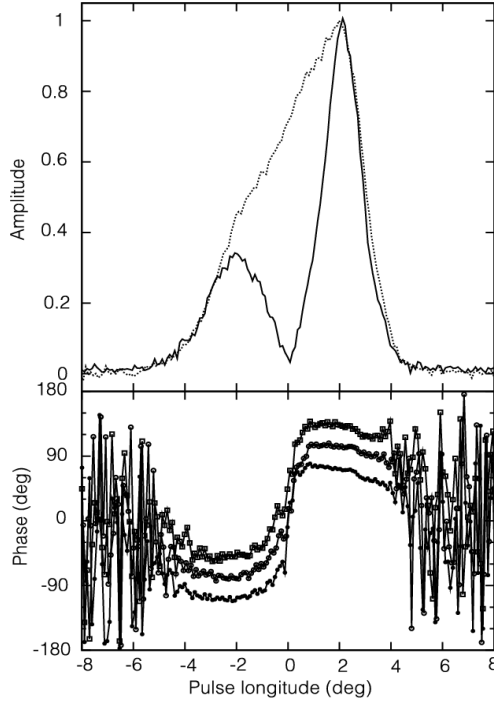
Figure 1.17: Subpulse amplitude (upper panel) and phase (lower panel) envelopes for PSR 0320+39 (Edwards et al., 2003). The upper panel also shows the average pulse shape (dotted line). The subpulse amplitude envelope shows a minimum near zero at the same longitude as a 180° shift in the phase envelope. The phase envelope is plotted three times representing analysis via three different techniques. A 60°/° slope has been removed from the phases.

et al. (2003) published their analysis of PSR 0320+39, a single figure in their paper had striking similarities to another known oscillating star, the rapidly oscillating AP star HR 3831. HR 3831 is an oblique rotator of $l = 1, m = 0$ with the pulsation axis aligned to the magnetic axis. Figure 1.18 shows phase changes of 180° as our line of sight crosses the nodal line. PSR 0320+39, as Edwards et al. (2003) show in Figure 2.4, has a minimum in the subpulse amplitude envelope corresponds to a 180° shift in the phase envelope. The evidence of what appears to be a nodal line in PSR 0320+39 instigated our development of a non-radial oscillation model for pulsars.

We start by modeling the total intensity and show that a pulsational model can reproduce the observed phenomena. In addition to PSR 0320+39, we re-
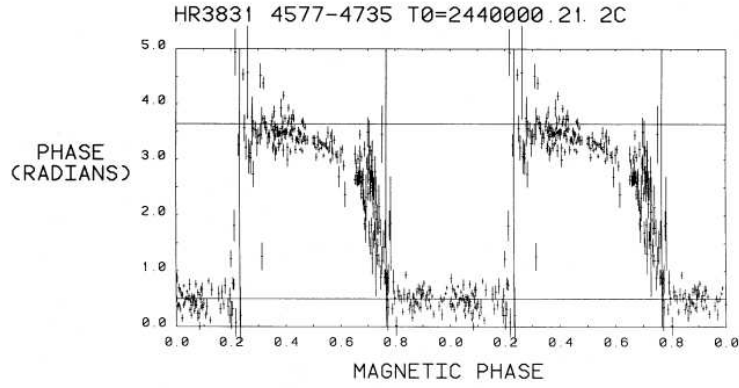
Figure 1.18: The oscillation phase versus magnetic rotation for rapidly oscillating AP star HR 3831 (Kurtz et al., 1990).

examine PSR 1919+21, the first pulsar. When PSR 1919+21 was discovered in 1968, it revolutionized scientific thinking about neutron stars from both a theoretical and observational standpoint. Even after almost 40 years, this star shows unique and interesting behavior that cannot easily be explained by most current drifting spark models, specifically the anticorrelation in subpulse phase between adjacent components. Yet a non-radial oscillation model naturally explains the subpulse phase jumps due to the presence of a nodal line. In this qualitative manner, we compare PSR 1919+21 to published results. We also model PSR 1237+25, another complex, multi-component pulsar to published analyses.

After demonstrating that we can successfully reproduce the total intensity behavior of pulsars, we then elaborate on our non-radial oscillation model to encompass linear polarization phenomena that are associated with pulsations (the Stokes' parameters Q and U). We link the displacement and velocity of the oscillations to two distinct orthogonal polarization modes which are then combined into the Stokes' parameters. We revisit PSR 1919+21 and PSR 1237+25 and find that these pulsars fit into a specific case of the more general model which includes polarization. We conduct quantitative fit of our model to PSR 0943+10 to archival data. We use this pulsar because it has been exhaustively studied in

40

the literature and its behavior is well-documented. Furthermore, it has a simple morphology that lends itself well for quantitative fitting and our model is successful in reproducing its behavior.

We used the 100 meter radio telescope in Green Bank, West Virginia to acquire 28 hours of high time resolution data on 16 different pulsars in all four Stokes' parameters. While the data has not yet been fully calibrated, we show preliminary data analysis on PSR 0809+74 and PSR 1237+25. PSR 0809+74 shows some of the most complex pulsar behavior which is not easily explained by current pulsar models but can be naturally explained with our non-radial oscillation model. We show our model of PSR 0809+74 and compare it to our data taken by the Green Bank Telescope and with published literature. We leave the quantitative fitting of these stars for future work.

Chapter 2

OBSERVATIONS OF NON-RADIAL PULSATIONS

2.1   Introduction

Upon the discovery of radio pulsations from pulsars by Hewish et al. (1968), Ruderman (1968) proposed that the pulses arose from non-radial oscillations of a neutron star. This idea was quickly displaced by a rotational model (Gold, 1969), but Drake & Craft (1968) again raised the possibility of pulsations when they measured individual pulse sequences for two pulsars and found within them narrow subpulses that moved to successively earlier times within the main pulse. Because this drift represented the presence of a "second periodicity" incommensurate with the spin period, it was natural to propose a time-like oscillation of

the star. Subsequent measurements, however, revealed complex subpulse patterns that did not conform to a pulsation model in any obvious way. Moreover, the persistence of unique subpulse shapes from pulse to pulse, along with problems of phase stability we will address in later sections, led Drake to conclude that the drifting subpulses were incompatible with the pulsation hypothesis (see Staelin et al., 1970; Hewish, 1970). Ultimately, pulsations were abandoned in favor of purely geometric models, although they reappeared from time-to-time in the theoretical literature (notably Hansen & Cioffi, 1980; van Horn, 1980; McDermott et al., 1988; Carroll et al., 1986; Finn, 1990; Reisenegger & Goldreich, 1992; Strohmayer, 1993). Most recently Duncan (1998) invoked toroidal modes to account for oscillations of soft gamma repeaters, but other than the work of Strohmayer (1992) and Strohmayer et al. (1992), there has been no determined attempt to account for the properties of classical pulsars with models involving non-radial pulsations.

Instead, most current models, though not all (cf. Lyne & Manchester, 1988; Han & Manchester, 2001), incorporate a circulating pattern of sub-beams, whose motion about the magnetic pole produces the drifting subpulses. In these models, pulsar emission comes from accelerated particles that originate near the pulsar magnetic pole and travel along curved paths in the star's magnetic field (see Radhakrishnan & Cooke, 1969; Komesaroff, 1970). The radiation is confined to a narrow beam by the dipole magnetic field geometry (Goldreich & Julian, 1969) and relativistic beaming along the direction of particle motion, which is roughly parallel to the magnetic axis, not perpendicular as in the models of Gold (1969), Smith (1970) and Zheleznyakov (1971). The observed brightness of pulsar beams effectively demands that the radiation is coherent, but the question of how it is produced is not settled (Jessner et al., 2001; Lesch et al., 1998; Melrose, 1995).

Early studies of pulsar single pulses and average pulse shapes (Taylor et al., 1975; Lyne et al., 1971, and others) led to the addition of more elaborate emission structures within the model pulsar beam. These features sweep past our sightline

and recreate the variety of pulse shapes we observe. Backer (1976) described a target-shaped emission pattern (a central core surrounded by an annulus) that can reproduce a wide variety of pulse morphologies depending on whether our sightline crosses the center of the pattern, yielding a three component pulse, or crosses only the annulus, resulting in a one or two component pulse. Oster & Sieber (1977) added a second annulus and rotating features to reproduce pulses with more than three components and drifting subpulses. In 1975, Ruderman & Sutherland (1975) supplied a physical basis for the model by suggesting that the emission arises from localized discharges or sparks near the polar cap. These are arranged in annular patterns, and rotate naturally due to the crossed components of the magnetic and electric fields.

In addition to the fixed and drifting substructure, models must account for observations of two kinds of discrete events observed in some pulsars; "mode changes", which abruptly alter the character of the substructure, and pulse "nulling", during which the pulse emission drops below detectable levels for one or more spin periods of the pulsar (Backer, 1970c,b; Bartel et al., 1982). In the Ruderman & Sutherland (1975) model, mode changes and nulling result from a collapse or reorganization of the fixed and moving spark structures, after which they must reappear with the same features they had previously.

Several reviewers have summarized observational and theoretical progress in the study of pulsar beams. The most ambitious is Rankin (Rankin, 1983b,a, 1986, 1990; Radhakrishnan & Rankin, 1990; Rankin, 1993a; Mitra & Rankin, 2002), who has both reviewed and synthesized the observations into an empirical model incorporating polarization and spectral behavior. Manchester (1995) gives a somewhat different view of the beam geometry. Most recently, Graham-Smith (2003) has published a succinct review that includes both "normal" and millisecond pulsars.

Against this backdrop, as a student project, we conducted a re-analysis of archival data on PSR 0943+10 to look for evidence of non-radial pulsations,

which, according to theory, might have periods ranging from milliseconds to seconds (McDermott et al., 1988). Our analysis, which will appear in a subsequent paper, convinced us that time-like oscillations with a period of 31.8 msec are a viable alternative to the rotating carousel of emission beams proposed by Deshpande & Rankin (2001), but we could find no compelling reason other than aesthetics to *prefer* a pulsational model. In search of a definitive test, we reviewed the extensive observational literature on pulsars, and found intriguing evidence for non-radial pulsations as a universal mechanism for drifting and stationary subpulses. Moreover, we found that the original reason for abandoning pulsational models does not apply to non-radial pulsations of high azimuthal degree (ℓ) in which our sightline crosses pulsation nodal lines. The presence of nodal lines increases the variety and subtlety of expected subpulse behavior.

The purpose of this paper is to introduce a model in which high ℓ pulsations aligned to the pulsar magnetic pole take the place of the fixed and moving structures of the circulating spark model, but other details of the geometry remain unchanged. In this paper we will explore only the phenomenological consequences of this substitution, and compare them qualitatively to published observations. We will not discuss in any detail problems in the physics of pulsed radio emission or polarization mechanisms. In §2.2, we will present the basic features of our model, and explore its observational properties, some of which are not immediately obvious. Our main purpose is to lay the groundwork for future application of the model to radio measurements of individual and average pulse profiles. In §2.3 we will examine qualitative evidence in favor of our model, reserving quantitative comparisons for subsequent papers. The strongest evidence we will present comes from published measurements that show subpulse phase behavior difficult or impossible to explain using the circulating spark model, but demanded by high ℓ pulsations. We will also discuss analogies between pulsar behavior and that of known pulsating stars, specifically the rapidly oscillating peculiar A stars (roAp) and the pulsating white dwarf stars. This will demonstrate that there are

precedents for the model behavior we propose. In §2.4, we will speculate about theoretical aspects of our model, such as the pulsation driving mechanism, and we will introduce the notion of "horizontal mode trapping", which can account for the high ℓ character of the proposed modes and relate them to the observed period evolution of pulsar beam widths. We will end by highlighting the potential for neutron star seismology, which can yield direct measurements of interesting physical quantities like the buoyancy of neutron star surface oceans.

2.2   Morphology of Non-radial Pulsations

In this section we will describe the basic emission patterns that we expect non-radial pulsations to produce. It is simplest, though not strictly necessary, to confine ourselves to pulsations where the material displacements follow spherical harmonics with azimuthal order $m = 0$. Using the notation Robinson et al. (1982) applied to white dwarfs, we can express displacements as follows:

$$\xi = Y_{\ell,0}(\Theta, \Phi) \cos(w_t t + \phi) \tag{2.1}$$

where the Y is a spatial distribution of pulsation amplitudes, Θ and Φ are spherical coordinates aligned to the *magnetic* axis of the star, and $\cos(\omega_t t + \phi)$ is a time-like variation.

2.2.1   *Fixed and Variable Pulse Structure*

Already we see in Equation 2.1 the expression of an important feature of pulsar emission. In a series of individual pulses from a pulsar there may be no two alike, yet the average of a sufficient number of pulses builds up a profile that is stable in longitude and repeatable. Figure 2.1 illustrates this behavior with two sequences of pulses from pulsar PSR 0943+10 and their respective averages. A series of "driftbands" that represent the positions of subpulses in successive

46
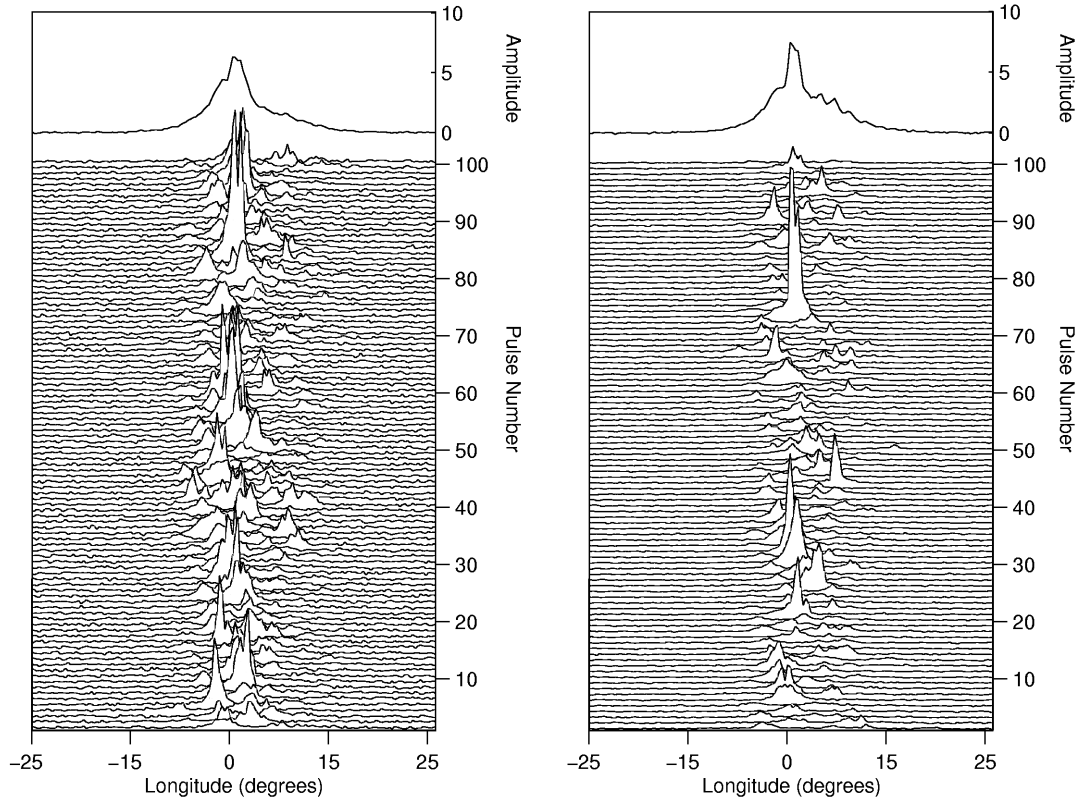
Figure 2.1: Two sequences of 100 pulses each from 430 MHz observations of PSR 0943+10 (lower panels), and their averages (upper panels). The subpulses show organized drift from right to left, along with disorganized amplitude behavior, but their averages converge to similar envelopes. The data are from Suleymanova et al. (1998) and are also published in Deshpande & Rankin (2001).

spins of the pulsar, can be seen going from right to left. Note that within each individual pulse there are two, sometimes three, subpulses, but the average pulse shape is single-peaked. The abscissa is actually time within the pulse, but as conventional we plot longitude calculated according to the formula $\Phi = 360°/P_1$, where P_1 is the pulsar spin period. Following standard convention, we will use P_2 to represent the time interval between consecutive subpulses (the horizontal spacing between subpulses in Figure 2.1) and P_3 to represent the time required for subpulses to return to a fiducial longitude (the vertical spacing between subpulses in Figure 2.1).

Though they exhibit large pulse-to-pulse amplitude variations, the drifting pulses in Figure 2.1 are modulated, on average, by a longitude stationary envelope. In some pulsars this has more complex structure than in PSR 0943+10, as we shall see in a moment. In her review and synthesis of pulsar data, Rankin (1983b) expressed the difference between the information carried by average pulsar profiles and sequences of individual pulses thus: "it seems that profiles and pulse sequences must then each manifest some largely independent physical basis in the emission region." As seen in Equation 2.1, non-radial oscillations offer a natural separation between fixed and variable structure in the form of spatial and time-like portions of a normal oscillation mode.

In addition to oscillations obeying Equation 2.1, we must also propose that these oscillations are coupled to the radio emission mechanism, and that they can generate time-modulated emission according to ξ of Equation 2.1. For consistency with the observations, we do not want the pulsations to subtract emission in the negative part of their cycle, so in our simulations we have kept only positive values of ξ. An alternative approach, analogous to the method of Edwards & Stappers (2002), would be to add a longitude-dependent bias to ξ. This would change the appearance of the simulated individual and average pulse shapes, and if large enough, would mute the nodal structure in the average pulse shapes relative to those shown in this paper.

We also assume that for a fixed radio frequency band, the emission originates at about the same altitude above the magnetic pole. This means that longitudinally distinct regions on the stellar surface will correspond to longitudinally separated pulse components, though the separation grows larger with increasing emission altitude due to the dipole field geometry (Komesaroff et al., 1970; Thorsett, 1991). This assumption is consistent with the measurements of Gil (1991) and Gil & Kijak (1992), who found similar emission heights for the various pulse components, but in conflict with the picture described by Rankin (1993a) or even Gangadhara & Gupta (2001) (see also Gupta & Gangadhara,

2003). Finally, we note the sinusoidal pulses that result from Equation 2.1 will not be sufficient to reproduce the non-sinusoidal profiles seen in Figure 2.1, or the large variations in pulse size, but they will illustrate the essential morphological features pulsations can produce. This level of abstraction will allow later incorporation of simulated emission mechanisms (e.g. shot-noise models, Rickett, 1975; Strohmayer et al., 1992) without affecting the tests of our model presented in this paper.

Figure 2.2 shows oscillations with $\ell = 70$ and $m = 0$ mapped onto the surface of a neutron star aligned with the magnetic axis. Dark regions indicate negative displacements and light regions positive ones. After a half cycle of the pulsations, the dark regions would be light and *vice versa*, but the nodal lines separating them would remain unchanged, except for rotation of the whole pattern about the rotation axis of the star (shown as a line extruding from the top of the sphere in Figure 2.2). This model is similar to the "oblique pulsator" model developed for roAp stars by Kurtz (1982), except that ℓ is much higher here, and the pulsar only emits from a small region near the magnetic pole. We have indicated the boundary of the emission region in Figure 2.2 with a circle around the magnetic pole. In §2.4 we will present a justification for why this boundary should coincide with a nodal line, and we will propose that the oscillations have different amplitude, perhaps even zero amplitude, outside of this boundary, a property we have not tried to reproduce in Figure 2.2. Following convention, we will use α to denote the angle between the pulsar's spin and magnetic axes, and β for the minimum angular separation between the magnetic pole and our line of sight, which is sometimes also called the "impact parameter".

If the pulsar in Figure 2.2 rotates such that the emission region passes under our line of sight, we can observe two different kinds of variations. Because the oscillation amplitude is always zero at nodal lines, but can be non-zero elsewhere, the nodal lines sweeping past our line of sight can create pulses with a repetition rate related to the rate of nodal line passage. To estimate this rate, consider

49
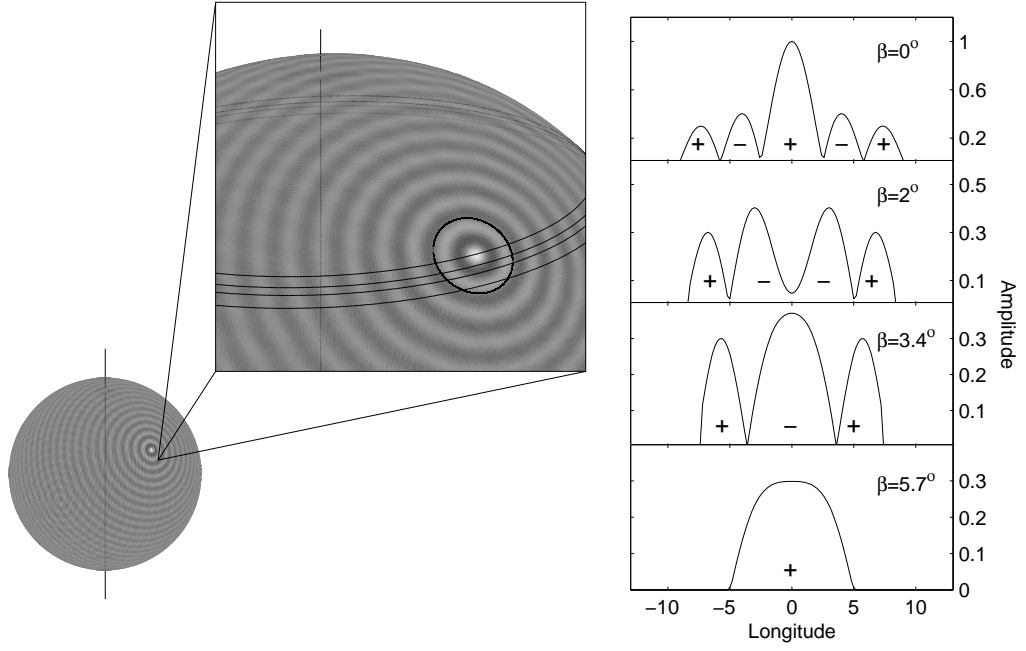
Figure 2.2: An oblique pulsator model for pulsar beams, showing an $\ell = 70, m = 0$ spherical harmonic aligned to the magnetic axis of a neutron star. The angle between the rotation axis and magnetic pole is $\alpha = 50°$ in this illustration. The circle around the magnetic pole in the enlarged view denotes the boundary of the emitting region. This region is crossed by four sightlines with different impact parameters (β, see text). For each sightline, the inset shows the corresponding rectified slice of the spherical harmonic, representing the average beam profile. At the boundaries corresponding to nodal lines, subpulse phase changes by $180°$, denoted by alternating $+$ and $-$ signs in the figure.

the case $\alpha = 90°$, $\beta = 0°$. In one full spin of the star our sightline crosses each nodal line twice, so the crossing rate is $P_1/2\ell$, but the period of a full cycle of the variations is twice this amount, or P_1/ℓ, because ξ changes sign at each nodal line. For arbitrary α, the number of crossings is reduced by $\sin(\alpha)$, so the apparent average period of the spatial variations is:

$$P_{node} = \frac{P_1}{\ell \sin(\alpha)} \tag{2.2}$$

For simplicity, we have suppressed the more complicated dependence on β, which can be seen in the inset of Figure 2.2. The important feature to recognize is that the zeroes caused by the spatial node pattern remain at fixed longitude in

subsequent spins of the pulsar unless either ℓ or the emission geometry changes.

At the same time as these nodal lines sweep past, the time-like oscillations generate pulses with a repetition rate related to the oscillation frequency as follows:

$$P_{time} = \frac{2\pi}{\omega_t} \tag{2.3}$$

The behavior we observe in a pulsar beam depends upon the relationship between these two periods. If $P_{node} > P_{time}$, then we will see subpulses narrower than the nodal line structure, and, as long as P_{time} is incommensurate with P_1, these subpulses will drift in longitude. Furthermore, as long as the measurement does not span a nodal line, the separation between subpulses P_2 will be approximately equal to P_{time}. P_2 is not exactly P_{time} because the nodal structure that modulates the amplitudes of the subpulses also affects their times-of-maxima. For $P_{node} > P_{time}$, this causes longitude dependent subpulse drift such that P_2 is less than P_{time} near nodal lines. In §A we quantify this behavior and show examples of the driftband curvature it generates.

In contrast to the appearance of individual pulses, the average of a sufficiently large number of pulses will reveal the fixed nodal line structure. In the inset of Figure 2.2, we have shown what this nodal line structure would look like by plotting various traverses our sightline might make across the magnetic pole. For each traverse, we have plotted a rectified spherical harmonic to simulate the average of many spin periods where emission occurs only when ξ is positive in Equation 2.1. Our figure is intentionally similar to that of Backer (1976), but whereas the spacing and width of his annular features was arbitrary, ours follows the spacing and shape of spherical harmonics. We will return to this and other features after considering the case where $P_{node} < P_{time}$.

For $P_{node} < P_{time}$, individual pulses show no structure significantly narrower than the nodal line spacing, but the modulation of fixed pulse components at P_{time} can still generate quasi-stationary driftlike variations. We have described
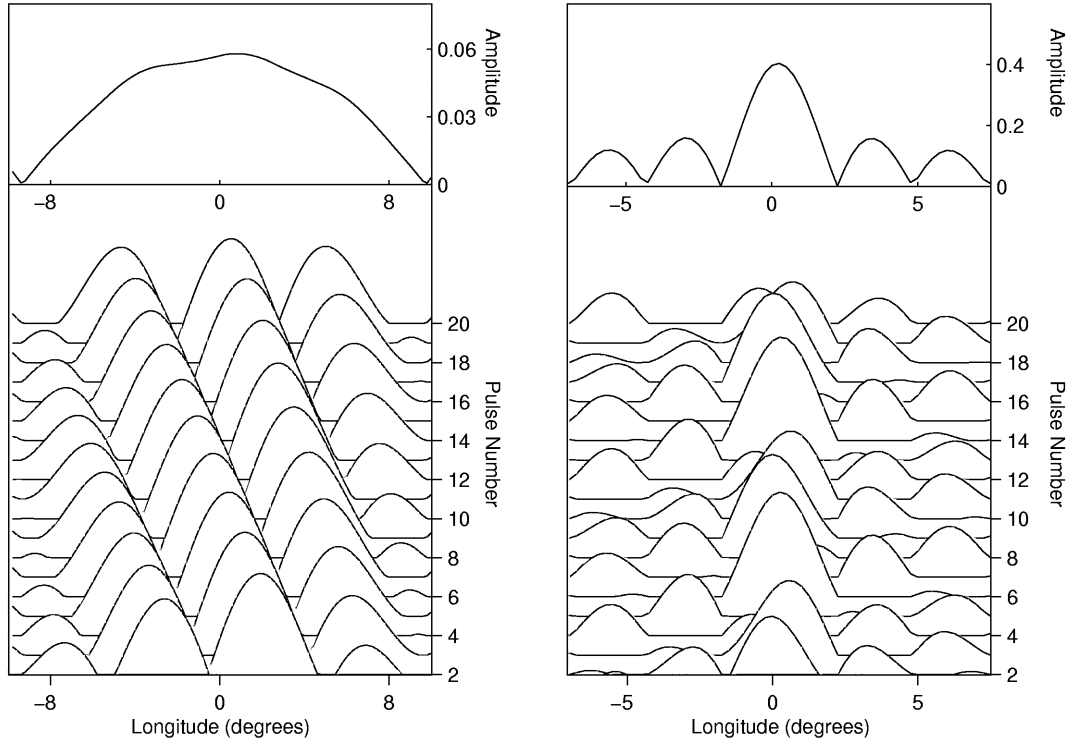
Figure 2.3: Oblique pulsator simulations representing individual and average pulse profiles of PSR 0943+10 (left) and PSR 1237+25 (right). The PSR 0943+10 simulation uses $\ell = 83$, $\alpha = 11.5°$, $\beta = 5.4°$, $P_1 = 1.098$ s, and $P_{time} = 31.78$ msec. There are no nodal lines in the pulse window, and $P_{time} < P_{node}$, so subpulses appear to drift continuously across the profile. The PSR 1237+25 simulation uses $\ell = 85$, $\alpha = 53°$, $\beta = 0°$, $P_1 = 1.382$ s, and $P_{time} = 89.90$ msec. There are four nodal lines in the pulse window, and $P_{time} > P_{node}$ so subpulses appear as quasi-stationary variations with phase reversals at the nodal lines.

the approximate behavior of pulse maxima for $P_{node} < P_{time}$, in §A, and have shown an example of synthetic data for this case in the right hand panel of Figure 2.3. Measurements of P_2 from a single pulse in this case will be strongly affected by P_{node}, making it difficult to estimate P_{time} without modeling. In spite of these differences, the average of a large number of pulses will look the same as in the case previously discussed, and as simulated in the inset of Figure 2.2.

For both cases, there is a 180° shift in subpulse phase between pulse components separated by a nodal line. This has been indicated by alternating + and

$-$ signs in the inset of Figure 2.2. This means that the driftbands caused by drifting subpulses, like those in Figure 2.1, will not be continuous across nodal lines. We have simulated this behavior in Figure 2.3. The left hand panel shows a model representing PSR 0943+10, where the sightline traverse resembles the $\beta = 3.4°$ case (with outer components missing), or the $\beta = 5.7°$ case shown in Figure 2.2. No nodal line is crossed, and the drift is continuous across the whole profile. On the right is a model representing the 5-component profile of PSR 1237+25, whose impact parameter is smaller. For this model, adjacent pulse components have different driftband phase, so there is no continuous pattern extending across the profile. The model we have used to represent PSR 1237+25 also has $P_{node} < P_{time}$, and illustrates the nature of the drifting in that case.

2.2.2   *Requirements of the Model*

The model properties described so far are broadly consistent with the observed behavior of pulsar radio emission, but to focus the discussion onto specific tests, we will state as succinctly as possible three definitive requirements of the pulsation model for comparison with observations.

1. At the nodal line separating adjacent pulse components, subpulse amplitudes should be zero, and their phase should jump by 180°.

This assumes that only one pattern of nodal lines is present at a time, an assumption that could be violated if several pulsation eigenmodes are excited simultaneously, as occurs in the white dwarf stars. Note that 1 does not require the radio emission be zero at nodal lines, but rather that the modulated component of the emission be zero; we have not explicitly required that all of the emission come from the pulsations. As a corollary to requirement 1, subpulse phase should drift almost linearly between the 180° jumps, to within the effects of relativistic aberration and delay (see Gil, 1991). If, however, the subpulse phase is inferred from the times-of-maxima of individual subpulses, these will follow the

53

curvature calculated in §A. The literature on driftband curvature (e.g. Wright, 1981; Krishnamohan, 1980) does not account for the possibility of 180° phase jumps, but we will show in §2.3 that they have been observed in a number of stars, most recently and dramatically by Edwards et al. (2003).

2. The spacing between fixed pulse components should follow the same distribution as a spherical harmonic sampled along a single sightline.

This requirement has to incorporate the effects of β, which is the first of several complications. The second complication lies in the radio frequency dependence of average profiles, which is far from simple (Mitra & Rankin, 2002). It is possible to understand these profile dependencies in the context of a radius to frequency mapping model, as first proposed by Komesaroff et al. (1970) and explored by Thorsett (1991). In this model, lower frequency observations measure emission from a higher altitude, where the dipole field has diverged more. Since the emission is apparently tangent to the magnetic field, this divergence introduces a frequency dependent "magnification". This magnification broadens pulse components at low frequencies compared to their higher frequency counterparts, and changes the β of effective sightline, since the particles emitting at higher altitude originated closer to the magnetic pole. However, if the magnification follows a dipole scaling, the ratios between component spacings will be preserved. Another difficulty arises from the Gaussian shape (Kramer et al., 1994) of measured pulse components, whose half-widths will differ from the cosine-like nodal regions of our model. We can mitigate this by comparing our model to measurements of pulse component maxima instead of widths, when possible. Finally, the emission we see probably represents an integral over some area on the star, due to the finite radio bandwidth and perhaps divergence of the emission itself. Together these problems make definitive tests problematic, but we will show that the average beam geometries explored by Rankin (1990, 1993a), Gould (1994), and Gil et al. (1993), are crudely compatible with the

54

requirements of our model.

3. Within the same pulse component, subpulses follow the relationship

$$\frac{1}{P_3} = \frac{1}{P_{time}} - \frac{n}{P_1},\qquad(2.4)$$

where $nP_{time} \approx P_1$.

This arises because P_3 is simply a beat between P_1 and P_{time} in our model. This relationship is the same as that given by Staelin et al. (1970) for pulsational models, except we have substituted P_{time} for P_2. As we have discussed, when ℓ is sufficiently large that one or more nodal lines appear in the observed pulses, P_2 is not necessarily a good estimator of P_{time}, thus *we cannot rule out the existence of stable clock based solely on the measured irregularity of P_2*. According to Staelin et al. (1970), one of the primary reasons for rejecting pulsational models for drifting subpulses was the relative instability of P_2 compared to P_3. In §2.3, we will answer this objection to pulsation models, thirty-four years late, by reproducing observations of PSR 1919+21, the first pulsar discovered. We will see that a model satisfying requirement 3 can simultaneously exhibit variations in P_2 like those measured by Drake & Craft (1968) and Backer (1970a).

As a corollary to 3, neither P_{time} nor P_3 should be affected by the radius-to-frequency mapping that broadens P_{node} at lower radio frequencies. So while the components of an average profile grow farther apart when observed at low frequency, the time-like pulses will not. Once again, it is crucial to recognize that P_2 may not be a good estimator of P_{time}, especially when P_{time} exceeds P_{node}. In that case measurements of P_2 can be dominated by the nodal line structure instead of P_{time}. As we will discuss in §2.3, measurements of the frequency dependence of P_2 show negligible frequency dependence for those pulsars where $P_{time} < P_{node}$, and an increasing frequency dependence as P_{node} approaches P_{time} (Izvekova et al., 1993; Gil et al., 2002), consistent with the requirements of our model.

2.3 Comparison to Observations

2.3.1 *Subpulse Phase Jumps*

A phase jump of 180° is not subtle behavior, so if our model is correct then this property of drifting subpulses should have been observed repeatedly. Interestingly, the first measurement of phase differences between adjacent pulse components came relatively early, in Taylor et al. (1975), but its significance for pulsation models was not recognized or pursued. Taylor et al. (1975) constructed individual time series for each of the five pulse components in PSR 1237+25, and cross-correlated them. With the exception of the central component, their analysis showed that components adjacent to each other in longitude have opposite subpulse phase (see Figure 11 in Taylor et al. (1975)). This behavior required Oster & Sieber (1977) to place the emission regions on their inner circulating carousel out of phase with those on the outer (see Figure 13 of Oster & Sieber, 1977), and led Hankins & Wright (1980) to propose a spiral emission pattern. In addition to PSR 1237+25, Taylor et al. (1975) found similar anti-correlations for the components of PSR 0329+54. Eleven years later, Proszynski & Wolszczan (1986) applied the same analysis with better resolution to PSR 1919+21, PSR 0809+74, and PSR 1237+25 (again). All three of these objects show behavior consistent with 180° jumps in their subpulse phases in at least one radio band.

In addition to these four objects, Edwards et al. (2003) recently applied their two-dimensional fluctuation spectrum technique to PSR 0320+39, and found dramatic evidence for phase and amplitude modulation like that expected at a nodal line. In Figure 2.4, we have reproduced Figure 3 of their paper, which was largely responsible for guiding us to the model we are proposing. As Edwards & Stappers (2002) point out, the two-dimensional Fourier transform as they apply it makes use of all the phase information in the data to produce phase and amplitude envelopes with high signal-to-noise ratio even for modest quality data. In Figure 2.4, the phase envelope shows the 180° phase shift we expect

56
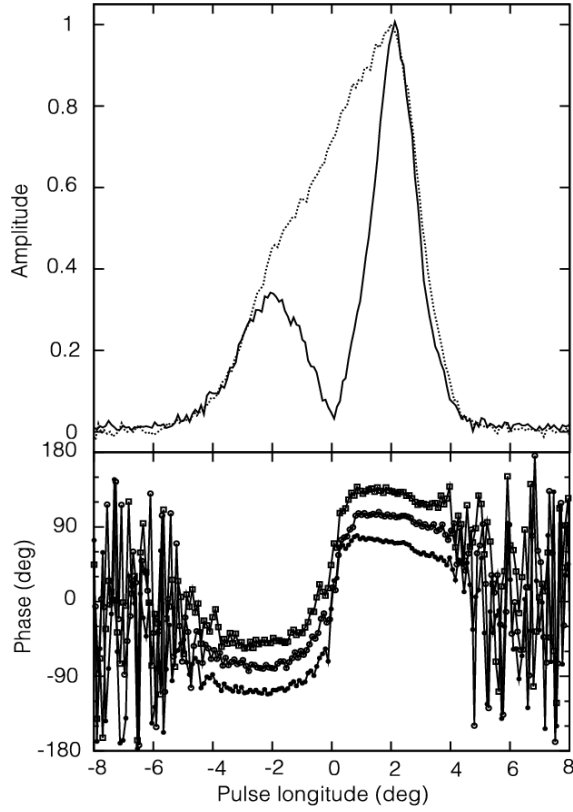
Figure 2.4: Subpulse amplitude (upper panel) and phase (lower panel) envelopes for PSR 0320+39, reproduced with permission from Edwards et al. (2003). The upper panel also shows the average pulse shape (dotted line). The subpulse amplitude envelope shows a minimum near zero at the same longitude as a 180° shift in the phase envelope, consistent with the requirements of the oblique pulsator model. The phase envelope is plotted three times representing analysis via three different techniques. A 60°/° slope has been removed from the phases.

at a nodal line, and almost linear behavior in between (a 60°/° slope has been removed from the data).

At the same longitude as the phase shift, the subpulse amplitude is near zero, as required at a nodal line. This figure evokes comparisons to Figure 14 of Kurtz et al. (1990) (shown in Figure 2.5), which shows a similar phase shift in the rapidly oscillating Ap star HR 3831 as rotation changes the viewing geometry of the pulsation nodal structure. We note that our model requires symmetry in the pulse components which means that a second phase jump should appear
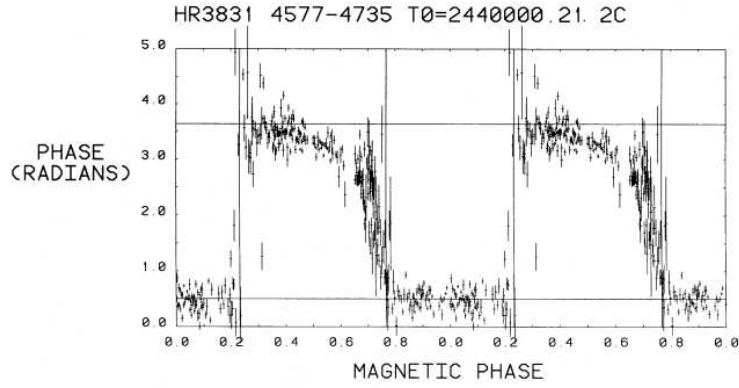
Figure 2.5: The oscillation phase versus magnetic rotation for rapidly oscillating AP star HR 3831 (Kurtz et al., 1990).

in the profile of Figure 2.4. In their subsequent paper Edwards & Stappers (2003) detected such a jump near the right hand edge of the profile.

Edwards & Stappers (2003) applied a similar analysis to PSR 0809+74 at two frequencies, with results that are more challenging for our model. The phase envelopes do not appear to be linear, and there are abrupt phase shifts not equal to 180°. Since the emission we observe is an integral over some frequency range and perhaps over some area on the star, we speculate that abrupt changes can be "washed out" by these inherent limits to the longitude resolution, especially at low frequency where the pulse components change their appearance most rapidly (Thorsett, 1991). Whether PSR 0320+39 is the lucky exception or the norm will require more data to tell. At any rate we do not think the problems with PSR 0809+74 should overwhelm our model, especially when compared to the elaborations these phase changes require in the drifting spark model (Edwards & Stappers, 2003), but caution and careful modeling will be required.

For PSR 1919+21, the prototype of pulsars and of drifting subpulses, we have reproduced a longitude resolved cross-correlation map from Proszynski & Wolszczan (1986) in the left hand panel of Figure 2.6. This is a contour plot of the cross-correlation of the time series at each longitude with that at a ref-
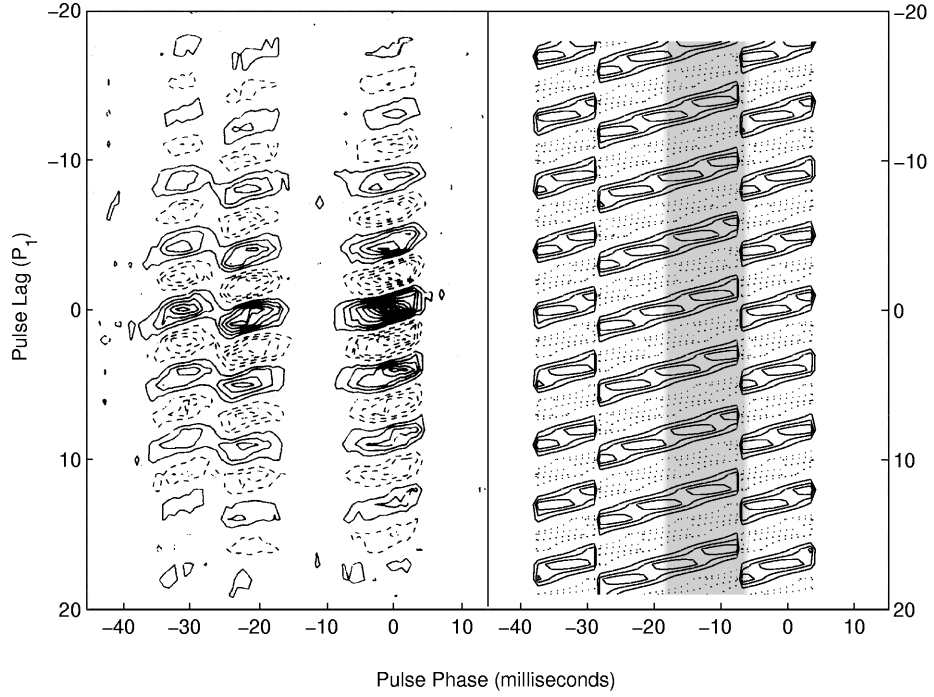
Figure 2.6: A comparison of longitude-resolved cross-correlation maps for PSR 1919+21. The left panel shows the cross-correlation of 1420 MHz time series data from each longitude with that at a reference longitude, reproduced with permission from Proszynski & Wolszczan (1986). The right panel shows the cross-correlation map of simulated data using an oblique pulsator model with $\ell = 100$, $\alpha = 45°$, $\beta = -2.35°$, $P_1 = 1.337$ s, and $P_{time} = 32.01$ msec. The phase reversals at ~ -30 and ~ -8 msec correspond to the locations of nodal lines in the model. Solid contours correspond to positive correlations.

erence longitude. The maxima occur at lags where the subpulse peaks align and minima where peaks align with troughs. For subpulses that drift uniformly from one side of the profile to the other, these diagrams should be crossed by bands of continuous slope proportional to the drift rate. Instead, we see sloping bands punctuated by two phase inversions, indicating that at those longitudes the subpulses abruptly change their phase.

To illustrate that pulsations can reproduce this behavior, we have simulated PSR 1919+21 with a model like that shown in Figure 2.2. The model has only five parameters, α, β, P_1, ℓ, and P_{time}, the values of which are listed in the caption

to Figure 2.6. First we generated a synthetic light curve using the positive values of ξ in Equation 2.1 sampled along a sightline defined by α and β. For each time sample in the light curve, we changed the longitude by $\Delta\Phi = 360°\Delta t/P_1$, and the pulsation phase by $\omega_t\Delta t$, where Δt is the time resolution. We eliminated data outside the observed pulse window, and constructed individual time series at each longitude. Finally, we cross-correlated these time series using the formula provided in Proszynski & Wolszczan (1986), and produced the contour map shown on the right hand side in Figure 2.6. We chose model parameters based on published values (except for ℓ), in some cases adjusting them slightly to improve the fit, which was done by eye. The model parameters should be regarded as illustrative only; no attempt was made to measure the quality or uniqueness of the fit.

In Figure 2.7, we show individual pulse profiles for our model of PSR 1919+21, to emphasize the variations that occur in P_2 even though the pulsation frequency is constant. We have indicated two different measured values of P_2 similar to those given by Backer (1970a), neither of which is close to the input oscillation period of 32.01 msec. We conclude that the published measurements of PSR 1919+21 are qualitatively consistent with a pulsational model incorporating a stable pulsation period and high ℓ.

We performed a second simulation for PSR 1237+25, with the results pictured in Figure 2.8. Once again the qualitative similarity is encouraging. In this star, more of the profile seems to be "missing" than in the previous one. Our model offers no ready explanation for these zones where the pulsed emission disappears, but it seems that the mechanism for generating pulsed emission fails. This failure could also explain the asymmetry in the profile of PSR 0320+39 that we discussed in conjunction with Figure 2.4. To compound the problem, Radhakrishnan & Rankin (1990) report that the pulsed emission seldom appears in the core component, and the polarization there is different, neither of which has any obvious basis in our model. On the contrary, the zone at the pole of
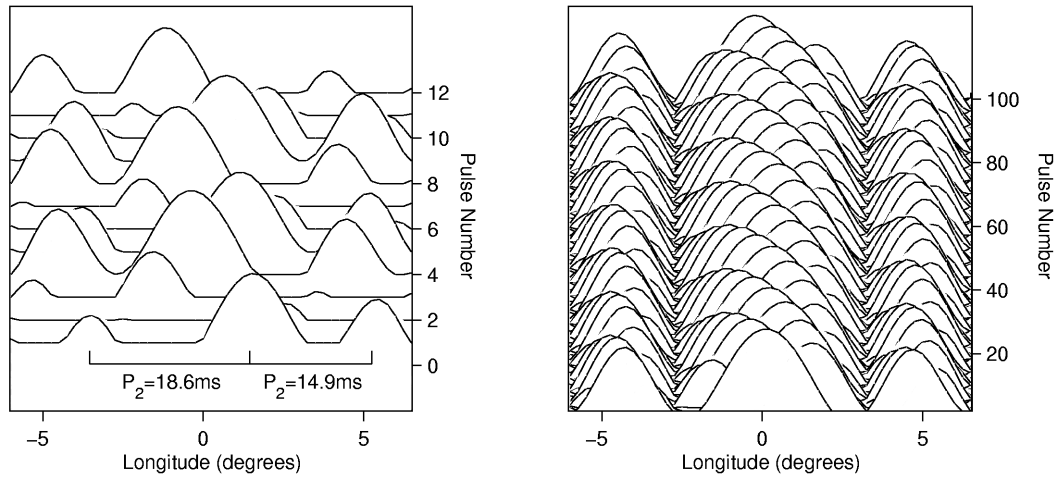
Figure 2.7: Synthetic individual pulse profiles for PSR 1919+21, generated using the same model as in Figure 2.6. The left-hand side shows subpulse separations similar to those measured by Backer (1970a). The right-hand side shows a larger number of pulses, making the amplitude modulation by nodal lines more apparent.

a spherical harmonic has the smallest area and therefore the largest pulsational displacements (to make the surface integral equal to those of other zones), so unless some mechanism saturates we expect larger amplitudes from the core.

We can put these issues aside pending deeper investigation of the emission mechanism, but observations like those described in Hankins & Wolszan (1987) offer a more direct challenge to our model. They analyzed PSR 1918+19 using the same cross correlation technique as shown in Figures 2.6 and 2.8, and found much different behavior. There is evidence in that pulsar for different drift rates in each of the 3 components of the average profile. We see no obvious way to reproduce the diagrams of PSR 1918+19 with a single pulsation frequency, but we note that the time series were very short (just 27 pulses in one case) and the inclination α is unusually small. More measurements and detailed modeling may lead to a solution.
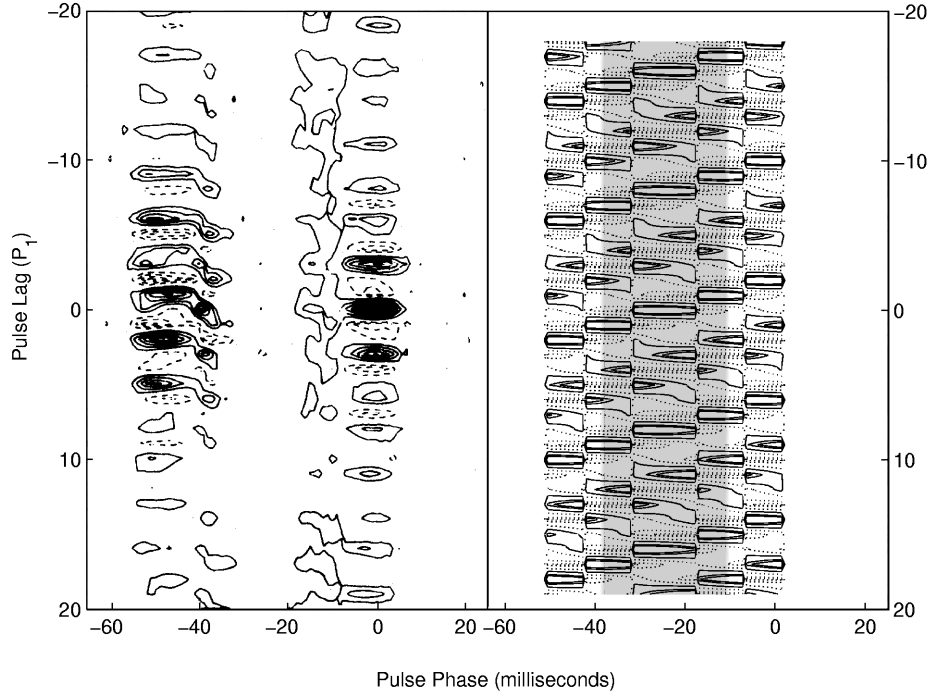
Figure 2.8: A comparison of longitude-resolved cross-correlation maps for PSR 1237+25. As in Figure 2.6 the left panel shows a map reproduced from Proszynski & Wolszczan (1986) for data at 408 MHz. The right panel shows the map for simulated data using an oblique pulsator model with $\ell = 85$, $\alpha = 53°$, $\beta = 0°$, $P_1 = 1.382$ s, and $P_{time} = 89.90$ msec.

2.3.2 Pulse Components and Their Separations

Now we consider the spacing between pulse components in the average profiles of pulsars. If the components are related to the zones of a spherical harmonic, as we propose, then they cannot have arbitrary widths and separations. For example, in our pulsation model, the angular separation between the pulsation pole and the first nodal line is ~ 0.44 times the separation between the pole and second nodal line, independent of ℓ as long as ℓ is high. Similarly, first and second antinodes have angular separations from the pulsation pole in the ratio ~ 0.55. We expect the modulated pulse components in pulsars with $\beta = 0$ to follow similar relationships. PSR 1237+25 is an good example, since it has five components and Lyne & Manchester (1988) and Rankin (1993b) give it $\beta \approx 0$

(as measured from rotation of the linear polarization angle). As an illustration, we have plotted in Figure 2.9 the average profile of PSR 1237+25 along with a $\beta = 0$ sightline through rectified spherical harmonic of $\ell = 85$. Note that the actual ℓ at the surface of the pulsar will be higher, depending on how much magnification the dipole field geometry has imposed.

It would be much better, though quite difficult, to compare the spherical harmonics to a statistical sample of pulsars with known β. Fortunately, Rankin (1990, 1993a), Gould (1994), Gil et al. (1993), Kramer et al. (1994), and Mitra & Deshpande (1999) have studied the ensemble properties of pulse shapes and uncovered consistent ratios between the core and annular emission components after adjusting for or eliminating the effects of α and β. These ratios are statistical averages suitable for comparison to spherical harmonics, but first we will discuss their dependence on P_1.

Rankin (1990) found that the angular size of the central emission component or "core" follows a $P_1^{-1/2}$ dependence, when allowance is made for variations in α. This dependence is the same as that Goldreich & Julian (1969) calculated for the size of the polar cap delineated by open magnetic field lines, i.e. those lines that do not close within the velocity-of-light cylinder at $cP_1/2\pi$. In the Goldreich and Julian model, this cap is the region from which charged particles stream off the spinning pulsar, providing both a mechanism for shedding angular momentum, and the possibility for radio emission from above the magnetic polar cap. The $P_1^{-1/2}$ dependence of emission cores measured by Rankin suggests that they are related to this Goldreich-Julian polar cap, although we should note that Lyne & Manchester (1988) measured a different P_1 dependence from Rankin.

In addition to the functional dependence, Rankin (1990) noticed that at any fixed P_1, the angular half width of pulsar emission cores was the same as the calculated apparent angular size of the Goldreich-Julian cap, e.g. about $2.5°$ for $P_1 = 1$ s. This led her to suggest that the core emission fills the cap near the pulsar surface. While appealing in its simplicity, this explanation requires that
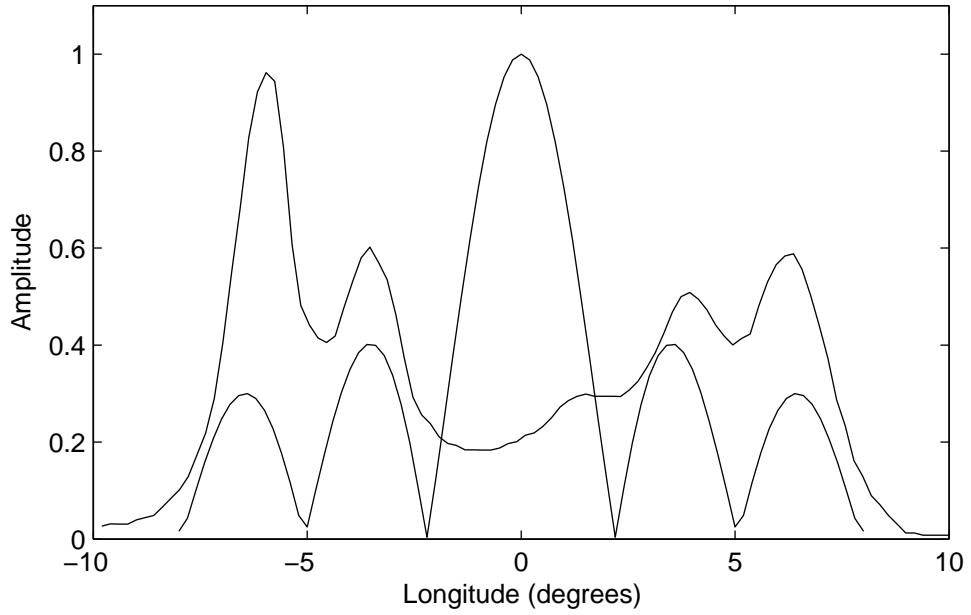
Figure 2.9: A comparison between a $\beta = 0$ slice through a spherical harmonic of $\ell = 85$ and the average pulse profile of 1237+25 measured at 320 MHz (see Rankin, 1986).

the annular emission patterns originate at different heights along the last open field lines. Gil (1991) has criticized this suggestion on observational grounds, but provided no alternative physical reason for the emission core to follow the scaling of the magnetic cap. As we will discuss in §2.4, our model suggests an explanation if the boundary separating open and closed field lines can act as a "mode trapping" boundary, which is always coincident with a pulsation node. The size of the core region would then have quantized values that scale with P_1 according to the to size of the polar emission cap.

Based upon her conclusion that the emission core size depends only on P_1, and upon her measurements of the annular emission regions which show the same P_1 dependence, Rankin (1993a) was able to infer that the ratio of the angular sizes of the inner and outer emission cones is 1.32, as measured at the outer half-power points. In similar fashion, Gould (1994) measured half-widths for the core and annular zones and found that the core components are 1.4 times as wide.

If we compare these measured component ratios to analogous ratios for the components of a spherical harmonic observed along a $\beta = 0$ sightline, we find that the ratio of the half-widths of the core and annular components in the model is ~ 1.49 independent of ℓ, or about 6% higher than the Gould measurement of 1.4. The ratio analogous to Rankin's inner and outer cone widths is not as good a match at ~ 1.72, 23% larger than Rankin's measurement. However, Gil et al. (1993) have found evidence for a different angular size of the inner components in five component pulsars, and the ratio of this innermost component with the outermost one is 1.62, again about 6% below the 1.72 ratio measured in our model. In §2.4 we will discuss how our model might lead to more than one quantized value for the inner and outer annuli if different numbers of nodal lines are trapped within the polar cap. As we will discuss, there is evidence for this kind of quantization in the core component as well, but it has been interpreted as a preferred inclination angle α (Rankin, 1990). For now, even if the results are somewhat ambiguous, it is gratifying to be able to make any testable predictions at all about the shape of average pulsar profiles.

2.3.3   *The Radio Frequency Dependence of Drifting Subpulses*

In the process of addressing model requirements 1 and 2 from §2.2, we have incidentally shown that the formula in requirement 3 is not necessarily contradicted by changes in P_2. Strict confirmation of requirement 3 will be difficult, because all attempts to measure P_{time} are badly aliased by the narrow, periodic pulse window, although PSR 0943+10 looks promising in the studies of Deshpande & Rankin (2001). The best strategy may be to concentrate on the wider profiles measured when α is small, since the aliasing will not be as bad. Fourier methods, especially the two dimensional transform of Edwards & Stappers (2002), will be indispensable to this effort, while direct measurements of P_2 in single or multiple pulses are misleading, as we have seen in our model of PSR1919+21.

The radio frequency dependence of P_2 is another area where the behavior of subpulse maxima can be misleading. Our model requires that P_{time} and P_3 be invariant with radio frequency, but we have already seen that P_2 will vary near nodal lines, even when P_{time} does not (see §A). Consequently, since observing at a different frequency changes the apparent longitude of the nodal lines, P_2 can vary with radio frequency even though P_{time} remains invariant. Qualitatively, we expect the radio frequency dependence of P_2 to approach zero when P_{time} is much smaller than P_{node} and no nodal lines are near. For P_{time} approaching P_{node}, the change in P_{node} with radio frequency will modulate P_{time} as well and introduce a frequency dependence into P_2. In the limit of very large P_{time}, the radio frequency dependence approaches that of the average components.

Izvekova et al. (1993) have studied the frequency dependence of subpulses in four pulsars. They found that P_3 does not change with radio frequency, consistent with the requirement of our model. For P_2, the frequency dependence is in all cases less than that of the average profile, also consistent with our model. For PSR 0031-07 and PSR 1133+16, both of which have continuous driftbands across the profile, the frequency dependence of P_2 is very weak, $\sim \nu^{-0.05}$ and $\sim \nu^{-0.06}$ respectively, while the frequency dependence of the average profile is about $\sim \nu^{-0.3}$. The other two pulsars show larger frequency dependencies for P_2, but one of these is PSR 0320+39, which we now know has multiple components separated by phase jumps, as shown in Figure 2.4. This means that the subpulse separation is similar to the separation between stationary profile components, and we expect a larger frequency dependence in this case. It will be interesting in future quantitative studies to attempt to reproduce the exact radio frequency dependence of the subpulses for individual pulsars by tuning P_{time}. In principle, each independent radio frequency measurement offers a separate constraint on P_{time} that might be useful in verifying its stability with respect to P_3.

2.3.4 *Mode Changes and Nulls*

A number of pulsars exhibit abrupt changes in their drifting subpulse behavior (Rankin, 1986) or their average pulse profiles (Bartel et al., 1982), or both. In some examples, these changes are cyclical or quasi-cyclical, such that the pulsar successively visits each of two or three modes (e.g. PSR 0031-07). A much larger number of pulsars (Rankin, 1986), including many of those with mode changes, undergo "nulls", in which the radio emission falls below detectable levels. The interesting property of these variations in the context of our pulsation model is the "memory" the pulsar must retain in order to return to the same states repeatedly. Inasmuch as pulsations represent eigenmodes of the neutron star, their eigenperiods reflect a durable physical structure that will vary only secularly as the star cools and slows down its spin. This means that a mode excited to observable amplitude and then damped can return again with essentially the same period.

Among the known pulsators, white dwarfs provide some exceptional examples of this behavior. The hydrogen atmosphere variable (DAV) white dwarf G29-38 sometimes oscillates with very large amplitudes in a dominant mode with ~ 610 s period, then changes abruptly to a large dominant mode at ~ 809 s, and then to very low amplitude pulsations with no dominant mode (Kleinman et al., 1998). This mode changing behavior suggests the exchange of energy between eigenmodes with different amplitudes (for the same energy content), though this has not been established with certainty (Dziembowski, 1982; Wu & Goldreich, 2001). We note the similarity of this behavior to pulsar mode changes and nulling. Pulsar mode changing involves changes in subpulse drift rates and in the mean profiles, both of which we might expect for changes between modes of different degree ℓ. Likewise, changes in the subpulse drift rate only might correspond to changes in the radial eigennumber n. Furthermore, the exponential recovery of drift rates after nulls in PSR 0809+74 (Lyne & Ashworth, 1983), suggests relaxation into a normal oscillation mode after a mode interaction. In the same

star van Leeuwen et al. (2002) found that the pulsar is often, and maybe always, in a different drift mode immediately following a null, which shows that they two phenomena are physically related. While it is possible to interpret this in the drifting spark model (van Leeuwen et al., 2003), pulsation mode switching may offer a more natural explanation.

Finally, evidence that nulling and mode changing are global phenomena comes from the pulsars with interpulses PSR 1822-09 and PSR 1055-52. Fowler et al. (1981) have observed that the interpulse emission in PSR 1822-09 changes its intensity when the main pulse changes between burst and quiescent modes. Likewise, (Biggs, 1990) found intensity correlations between the interpulse and main pulse in PSR 1055-52, and suggested non-radial oscillation as a possible mechanism for communication between the poles.

2.4 Discussion

Our main purpose in this chapter has been to set forth the requirements of a model for pulsar beams in which non-radial oscillations of high ℓ replace the *primum mobile* of drifting sparks in the Ruderman & Sutherland (1975) model. This groundwork will clarify future applications of our model to individual pulsars, which we will begin in a forthcoming study of PSR 0943+10. Although quantitative investigations are required for definitive tests, we have presented observational evidence that our pulsation model should be an active contender for the attention of observers and theorists alike. We will continue with some theoretical speculation about the nature of the pulsations.

2.4.1 *The Nature of the Pulsations*

When we invoke non-radial oscillations in our model, we mean any oscillations in which time-like variations are accompanied by spatial nodal lines that rotation can carry past our sightline. Immediately, this suggests various deformations

that might appear in the core, crust, or ocean of a neutron star (McDermott et al., 1988), but we should not rule out other possibilities such as oscillations in the magnetosphere above the magnetic pole (e.g. Rylov, 1978; Staelin et al., 1970; Schopper et al., 2002). The main problem we will encounter in identifying the pulsations is that most of the oscillations we can propose have frequencies too high to account for pulses with the repetition rate of 30 msec typical for subpulse periods. To be fully general we also should not rule out high frequency oscillations that are "switched" at low frequency, but we will find little guidance in pulsar literature for models of this sort.

The two quantities that will assist us in identifying the kind of oscillations our model should include are ℓ and P_{time}. In our illustrations, we have used $\ell \approx 70 - 100$ to match the width of features in observed profiles, but these profiles apparently do not originate at the surface of the neutron star. Rather, they are magnified versions from radiation emitted at tangents to the diverging dipole field. We can estimate the magnification factor, which we will call f_ν, by comparing the observed profile widths to the expected size of the Goldreich-Julian emission cap at fixed period P_1. At 1 second, for a pulsar with radius 10 km, the latter is 1.7°, while Rankin (1993a) measured 11.5° for the width of the outer annular beam. Together, these yield a magnification of $f_\nu \sim 7$ at 1 GHz. Thus an apparent ℓ of 85 represents a true ℓ at the surface of ~ 600. The dispersion relationship for g-modes (and torsional modes) McDermott et al. (1988) requires that P_ℓ scale as $1/\ell$, so if $\ell = 600$ has a period of 30 ms, then we expect the $\ell = 2$ mode with same radial overtone to have period ~ 9 s. This limits considerably the kinds of oscillations we might consider.

McDermott et al. (1988) gives periods near 9 s for low ℓ, low radial overtone ($n \approx 1$), core g-modes. However, these modes require very large energies to excite, and are trapped in the core by the solid crust, yielding small amplitudes at the neutron star surface. An alternative from McDermott et al. (1988) are the g-modes that propagate in the ~ 1m thick electron-degenerate Coulomb liquid

69

ocean overlying the solid crust in equilibrium neutron star models (Richardson et al., 1982). The low n ocean g-modes have periods near 0.3 s, rather than the 9 s we require, but the dispersion relation for g-modes gives longer periods for higher overtone, so the eigenperiod should increase to 9 s for $n \approx 30$. Therefore, ocean g-modes of $\ell \approx 600$, and $n \approx 30$ match the ℓ and P_{time} our model requires. According to McDermott et al. (1988), these modes have lower energies than the core modes, and large surface amplitudes. As in white dwarf stars, the material displacements in these oscillations are primarily horizontal because of the high surface gravity.

The ocean g-modes also have an associated temperature variation that offers a way to modulate the flow of charged particles from the pulsar surface at the pulsation eigenperiod. If we accept the results of Jessner et al. (2001), the electrons accelerated along open field lines from a pulsar magnetic pole can be provided by thermal and field emission from the neutron star surface, without the formation of a vacuum gap where sparks originate in the Ruderman & Sutherland (1975) model. This result practically requires that subpulses be related to a thermal variation at the neutron star surface, as g-modes provide. Thus non-radial oscillations appear to satisfy one of the basic requirements of a pulsar emission mechanism.

The other requirement for emission is that the liberated electrons be "bunched". Their acceleration away from the surface is naturally provided by the potential difference between the neutron star pole and the circum-pulsar medium (Goldreich & Julian, 1969), but conversion of the particle stream to coherent radiation requires bunching of charges, whether the conversion is via an antenna or a maser mechanism (Melrose, 1995). The radial structure of $n = 30$ ocean g-modes consists of ~ 3 cm zones of alternating pulsation phase. At any instant, this will correspond to a periodic variation of the temperature and pressure with depth. In electron degenerate plasma, the temperature is a property of the ions while the pressure is a temperature insensitive property of the electrons. The displace-

ments of an ion fluid element generate a buoyant restoring force only through their electrical coupling to the electrons, so the vertical pressure variation is associated with a vertically varying component of the electric field. If this can modulate the flow of electrons, as in a klystron, then the pulsations might also provide the mechanism for bunching the electrons emitted from the surface. The observational clues necessary to clarify this question may lie in subpulse polarization measurements, which are beyond the scope of this paper.

A problem with this picture comes from the work of Carroll et al. (1986), who added a strong magnetic field to the pulsation calculations. Because of the high electrical conductivity in the neutron star ocean, Carroll et al. (1986) treated the magnetic field as "frozen-in", and recalculated the pulsation frequencies for $B = 10^{12}$ G in the MHD limit. He found that the ocean g-modes become "magneto-gravity" modes with very short periods (< 1ms) and a different dispersion relation. The solution to this conundrum is provided by the conductivity calculations of Potekhin (1999). Potekhin finds electrical conductivities in the direction transverse to a $B = 10^{12}$ G field to be four to five orders of magnitude lower than the 10^{19} s^{-1} Carroll et al. (1986) assumed. Thus the ohmic diffusion timescale for displacements of 10 cm or smaller is $\stackrel{<}{\sim} 1$ msec, shorter than subpulse periods. Not only does this mean the calculations of Carroll et al. (1986) do not apply, it also means the magnetic field can simultaneously provide the driving mechanism, the amplitude limiting mechanism, and the mechanism for enforcing high radial overtones.

2.4.2 *Mode Driving and Trapping*

The high ℓ in our model suggests the concentration of pulsation driving energy into a small surface patch, otherwise it would average away in the sum over multiple surface zones with alternating phase. This concentration suggests consideration of the emission pole itself as the site of driving. The torque exerted by braking from particle emission will be concentrated at the open field lines, and

71

communicated to the rest of the star by magnetic and mechanical dissipation. If the magnetic field is coupled (even weakly) to the surface and it displaces material laterally, the possibility for feedback and mode driving exists. For example, suppose that torque on the open field lines results in a displacement of material on the polar cap. The heating that results can increase particle emission, which increases the torque. Depending on the time delays, this feedback could drive oscillatory motion. Other possibilities involving direct shaking of field lines (Boriakoff, 1976) by displaced material are also possible.

Whatever the driving mechanism, if there are g-mode pulsations in the neutron star ocean, it is reasonable to propose that their propagation behavior changes at the boundary between the emitting cap and the rest of the star, not only because the magnetic field changes from an open to closed configuration, but because the surface boundary condition changes. Thus the edge of the emitting cap constitutes a circular boundary that might "trap" pulsation modes in the horizontal direction, analogous to the trapping by composition transition zones in white dwarf stars (Winget et al., 1981). This "horizontal mode trapping" could provide a connection between the size of the emitting cap and the size of pulsation nodes by forcing surface nodal lines to lie at the circular boundary. If this connection is maintained as P_1 increases, it can explain why the core emission zone, as measured by Rankin (1990) and others, follows a $P_1^{-1/2}$ relationship. In this section, we will explore pulsation period evolution in the context of a horizontal trapping model.

2.4.3 *The Period Evolution of the Pulsations*

The pulsars measured to date seldom, if ever, have more than five components in their average pulse (cf. Gangadhara & Gupta, 2001, although their methodology is compromised by pulsations) In our model, five components could result from horizontal mode trapping at the third nodal line from the pulsation pole, and this is the geometry we depicted in Figure 2.2. We have already seen that

parts of the profile can be "missing", so the presence of five components in the model does not necessarily mean that we see all five. If we now force ℓ to have a value that places the third node at the emission boundary, we can write a relationship for the period evolution of ℓ. From Goldreich & Julian (1969), the width of the emission cap for a 10 km star follows:

$$W_{cap} = 1.7^\circ P_1^{-1/2}, \tag{2.5}$$

and the width of third nodal line scales as $1/\ell$, reaching 1.7° for $\ell \approx 600$. So we may write:

$$W_3 = 1.7^\circ \frac{600}{\ell}. \tag{2.6}$$

Enforcing horizontal mode trapping requires $W_{cap} = W_3$ so,

$$\ell = 600 P_1^{1/2}, \tag{2.7}$$

as long as the trapping stays at the third nodal line. This equation is a mathematical statement of the obvious requirement that as the emission cap shrinks during spin-down, the ℓ of trapped pulsations must go up. Some of the other consequences for the pulsations are not as obvious. For instance, from the dispersion relation for g-modes , P_{time} changes as $\sim 1/\ell$ if the radial overtone doesn't change, so we expect P_{time} to decrease as P_1 increases. However, the important ratio P_{time}/P_{node} becomes:

$$\frac{P_{time}}{P_{node}} \propto \frac{\sin(\alpha)}{P_1} \tag{2.8}$$

So as P_1 increases (or the spin and magnetic axes align), P_{time} shrinks with respect to P_{node} . This favors the appearance of narrow drifting subpulses in the long period pulsars, as observed. The impact parameter β, which we have ignored, may also play a role, since the decreasing emission cap size makes it less

likely that our sightline intersects the central component (see Figure 2.2), and P_{node} increases for such sightlines.

Finally we consider the possibility that the horizontal trapping may apply to the second nodal line instead of the third, requiring a lower value of ℓ for the same P_1. In this case, the central component will have a larger angular size at the same P_1 than for third node trapping. This would be observed as a bimodal distribution of core components, and there is evidence in Rankin (1990) for just such an effect (see Figure 1 of Rankin (1990)). Because Rankin (1990) assumed that the distribution of core sizes is solely an effect of α, the bimodality appears as an excess of pulsars at $\alpha = 35°$. While our explanation would eliminate this puzzling excess, it raises two problems of its own. First, we would expect some pulsars with interpulses in the distribution with larger core sizes, and Rankin (1990) finds none. Second, Figure 1 of Rankin (1990) shows the beam sizes for pulsars with single components, not five, meaning all the pulsars in this sample have pulse components within their emission caps that do not appear in the mean profiles.

2.5   Conclusions

Whether or not the foregoing discussion has revealed anything about pulsars, it has certainly demonstrated Clemens (1883) maxim that we can get "wholesale returns of conjecture out of such a trifling investment of fact." Nevertheless, the fact remains: pulsar beams show subpulse phase reversals at the longitude-stationary boundaries separating individual pulse components. We have shown that these changes are comprehensible in the context of an oblique pulsator model incorporating non-radial pulsations of high degree ℓ. The important features of our model are: non-radial oscillations aligned to and symmetric about the pulsar *magnetic* axis; surface displacements that follow a spherical harmonic distribution; radio emission that follows the displacements but is never negative;

pulsation modes of sufficiently high ℓ that nodal lines often appear in the pulse window; and pulsation frequencies that remain coherent over many pulsar spin periods. Variations on this basic model might include multiple pulsation modes with non-zero azimuthal orders, pulsations that are distorted, in reality or in appearance, by non-dipole fields, and modes that interact either through mode coupling or a non-linear emission mechanism.

Our model qualitatively reproduces the mean shapes of pulsar beams and the radio frequency dependent behavior of subpulses with a minimum of free parameters. In the most basic form of the model these are α, β, P_{time}, ℓ, and P_1. Our model also dictates specific requirements that can be tested quantitatively using new or archival data. We have embarked on a program to conduct such tests and we encourage others to do likewise. If the model survives these tests, then we will have the opportunity to measure fundamental properties of matter in a domain not accessible to laboratory experiments. The first challenge will be to determine the site of the pulsations, and then to connect measured eigenfrequencies with the eigenmodes of a structural model. Given the number of modes in the pulsation spectrum at large ℓ, this may be a daunting task, but even rough identification will provide limits on the thermal, electrical, and mechanical properties of constituents of a neutron star, the densest objects accessible to direct observational scrutiny.

Chapter 3

A PULSATIONAL MODEL FOR THE ORTHOGONAL POLARIZATION MODES

It is the time you have wasted for your rose
that makes your rose so important.
Antoine de Saint-Exupéry
The Little Prince

3.1 Introduction

In §2, we introduced an oblique pulsator model (Kurtz, 1982) for radio pulsars in which drifting subpulses are reproduced by non-radial oscillations whose periods are incommensurate with the pulsar spin period. The non-radial modes of our model are aligned to the pulsar magnetic axis, so in addition to the drifting time-like pulses, our model produces longitude stationary variations caused by nodal lines rotating past our line of sight. Although our model only includes seven parameters, it is able to reproduce a wide variety of observed behavior, including drifting and quasi-stationary subpulses, driftband curvature, and sub-

pulse phase jumps. It is also able to account for the correlation of subpulse phase between the pulse and interpulse of PSR 1702-19, as recently discovered by Weltevrede et al. (2007).

As we presented it, our model did not attempt to incorporate any polarization effects. This is a major shortcoming: pulsars emit highly polarized radiation with subtle and interesting properties. In this chapter we remedy this shortcoming, using only phenomena associated with non-radial oscillations. The model of our previous chapter then represents a special case of the more general model presented here, and the former maintains its success in reproducing data from a specific subset of pulsars. However, the more general model presented here allows us to reproduce a wider variety of pulsar behavior, including "orthogonal polarization modes" and their interplay with pulse longitude.

We begin in §3.2 with a summary of the (linear) polarization behavior of pulsars. Following this, in §3.3, we introduce the extensions to our non-radial oscillation model. These are phenomenological rather than physical, in that they represent the hypothetical effects of non-radial oscillations (in either the star or magnetosphere) without any established model for how the radio emission is actually produced. In section §3.4, we fulfill a promise made in Chapter (§2), which is a quantitative analysis of PSR 0943+10 using our model. This includes an examination of observational phenomena not emphasized in previous analyses of this star (Deshpande & Rankin, 2001). In our conclusions, we propose that our model presents an alternative to existing theories that is at once more compact in its assumptions and richer in the phenomena it reproduces.

3.2 Polarization in Pulsars

The publication by Radhakrishnan & Cooke (1969) of their single vector model for pulsar emission was a watershed in the study of radio pulsars, because it convincingly united diverse polarization angle behavior around an intelligible

principle. The linear polarization angle in an average pulsar profile rotates following a vector that points from the site of emission toward the magnetic pole. That pole is also the epicenter of our non-radial oscillations, and thus we shall see that it is possible to connect our non-radial oscillation model and the rotating vector model into a single elegant and effective description.

Once Radhakrishnan & Cooke (1969) had accounted for the rotation of linear polarization with pulse longitude, a new complication arose in the form of "orthogonal polarization modes" (Backer et al., 1976). At some pulse longitudes, the polarization angle occasionally jumps by 90 degrees, but continues to follow the rotating vector model on the orthogonal track. In some pulsars there is more than one switch between the tracks. Figure 3.1, reproduced from Stinebring, shows this behavior in the form of a histogram at each pulse longitude. At each longitude, the histogram counts the number of individual pulses that exhibit a particular polarization angle. The clear preference for one or the other orthogonally polarized modes is evident, as is the swing in angle associated with the changing vector to the magnetic pole. Note also that in those regions where the two modes occur with nearly equal frequency the linear polarization is reduced. From this behavior, Stinebring deduced that the orthogonal polarization modes are not disjoint (occurring one at a time but never simultaneously), but rather "superposed" (Stinebring et al., 1984a). That means the radiation we detect is the superposition of two simultaneously present emissions. The polarization angle will be that of the higher intensity mode, but if they are exactly equal, there will be complete depolarization. We will model this situation mathematically, using Stokes parameters for the two modes, in section §3.3.

Another common but not universal property of orthogonally polarized modes, evident in Figure 3.1, is the tendency for the switch between modes to happen repeatedly at fixed pulse longitude. For instance the switch in PSR 2020+28 is shown in the second panel in Figure 3.1, and is centered around the regions marked by the lines "A" and "B". Because it is longitude-stationary, this fea-

ture cannot be associated with rotating structure on the stellar surface (Rankin, 1986) and in many pulsars reproducing it requires the ad hoc superimposition of unrelated phenomena, e.g. birefringent double imaging of the circulating sparks (Rankin & Wright, 2003). From the scatter at each longitude in the polarization angle histogram, it is evident that the polarization in *individual* pulses can vary from the dominant mode. This arises because the polarization angle also rotates substantially with the phase of the drifting subpulse. That is, the rotating vector model describes the behavior of the polarization angle averaged over many pulses. Within an individual pulse, the polarization may change in correlation with subpulse phase rather than longitude (Manchester et al., 1975). This polarization angle behavior is analogous to the intensity behavior of individual and average pulse shapes: individual pulses are dominated by the phase of the drifting subpulses, while average pulse shapes show the envelope of their average intensities at each longitude, as we explored in §2. It is important to recognize that this polarization angle change within individual subpulses can contribute to the depolarization of the average profiles (Cordes & Hankins, 1977), even when all the individual pulses are fully polarized.

3.2.1 *The First Polarization Mode*

The implications of orthogonal polarization modes, considered in light of the rotating vector model, is that there are two highly linearly polarized sources of radiation. Michel (1991) has criticized models in which there is only one highly linearly polarized source that is separated into two states. Almost all of the radio emission mechanisms reviewed by Melrose (1995) can produce one linearly polarized component of radiation, but not the other. Accordingly, in our previous work, we considered only one source of radiation, and proposed that it was modulated by non-radial oscillations of high azimuthal degree (ℓ). In this chapter, we retain the modulation by pulsational displacements, and explicitly connect it to the radio emission whose transverse electric field vector

79
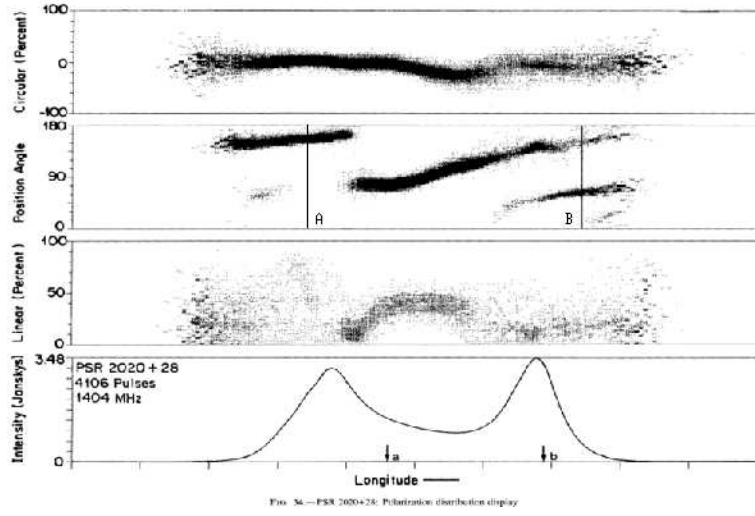
Figure 3.1: The properties of PSR 2020+28 (Stinebring et al., 1984a). The top three panels show in histogram form, starting from the top, the circular polarization percent, polarization angle, and linear polarization percent. The average pulse shape is in the bottom panel.

points toward the magnetic pole in concordance with the single vector model of Radhakrishnan & Cooke (1969) (i.e. in the $\hat{\Theta}_{mag}$ direction as defined in Figure 3.2). We refer to this radiation as the "displacement polarization mode", to remind us of its connection to pulsational displacements. We express the time dependent amplitude of this radiation mathematically as the positive portion of the function:

$$A_{DPM}(t) = a_{0_{DPM}} + a_{1_{DPM}} \Psi(\phi, \theta) \cos(\omega t - \psi_0 - \psi_{delay})) \qquad (3.1)$$

where Θ refers to the magnetic latitude, because the pulsations in our model are aligned to the magnetic pole. This expression is slightly more general than in Clemens & Rosen (2004) because it explicitly includes an unmodulated emission baseline ($a_{0,DPM}$) which we discussed in Chapter §2 but, for simplicity, did not incorporate into our mathematical function. The negative portions of this function would represent the emission of less than zero light, and for this reason we

80

discard them. The new expression also breaks the phase into two terms, one of which allows for the arbitrary phase of the drifting subpulses, and the other of which allows for a time lag between the maximum amplitude of the pulsations and emission maximum (ψ_{delay}), which we explain below.

In Clemens & Rosen (2004), we speculated about how pulsational displacements could affect the intensity of the radio emission, but without knowing the radio emission mechanism, or even the site of the pulsations, convincing physical arguments were impossible. We preferred models in which the pulsations are in the neutron star (Strohmayer, 1992; McDermott et al., 1988), rather than in its magnetosphere (Gogoberidze et al., 2005). Strohmayer (1992) proposed that neutron star oscillations could modulate the radio intensity if greater quantities of plasma are injected into the magnetosphere during pulsation maxima, when local heating of the stellar surface is greatest. This remains a sensible suggestion in light of the conclusion by Jessner et al. (2001) that thermal emission of electrons dominates the rate at which charged particles flow from the star to magnetosphere. Following this reasoning, we continue to assume in this paper that the amplitude of the displacement polarization mode, as defined above, follows surface thermal variations caused by non-radial oscillations of the neutron star. This means that for non-adiabatic oscillations, the thermal maximum can lag the displacements in phase. We have included ψ_{delay} explicitly to allow for this effect.

This model is directly analogous to the white dwarf stars, except in white dwarfs the thermal variations directly modulate the radiative flux from the stellar surface while in neutron stars the changing radio flux is a secondary effect of the modulations in plasma emission. The ψ_{delay} term is absolutely required in models of white dwarf pulsations (van Kerkwijk et al., 2000), and its size has been measured for several pulsation modes in G29-38. For alternative modulation mechanisms unrelated to surface temperature (Gogoberidze et al., 2005), ψ_{delay} may not be necessary and could then be set to zero. We shall see that the

value measured from the data has sign and magnitude consistent with thermal variations.

We explored the properties of a model based on Equation 3.1 in Clemens & Rosen (2004) (for the choice $a_{0,DPM} = 0$, $\psi_{delay} = 0$), and showed it to be a good model for some pulsars but not others. In particular it was successful in PSR 1919+21,PSR 1237+25 and PSR 0320+39. Interestingly these pulsars do not show orthogonal polarization mode switching in the sections of the profiles we modeled, implying that they are dominated by a single polarization mode. They are therefore exactly the kind of pulsars that should be amenable to modeling with only Equation 3.1, a congruence we noticed only after the development of the model in this paper.

3.2.2 The Second Polarization Mode

In order to model pulsars that emit radiation in two orthogonal polarization modes, we must include a component of radio emission with transverse electric vector orthogonal to the Radhakrishman and Cooke vector used in our displacement polarization mode. The Radhakrishman and Cooke vector points in the $\hat{\Theta}_{mag}$ direction in Figure 3.2; to explain orthogonal polarization mode changes, we require emission in the $\hat{\Phi}_{mag}$ direction as well. Existing models with this property are few. The maser mechanism of Fung & Kuijpers (2004) produces such radiation by the ad hoc imposition of a "wiggler" oscillation with transverse $\vec{E}$ vector pointing in the $\hat{\Phi}_{mag}$ direction (see Figure 3.2). The Cherenkov Drift mechanism of Lyutikov et al. (1999a) produces the same polarization in a more natural way, by orienting the vector Cherenkov drift velocity (u_D) along the $\hat{\Phi}_{mag}$ direction. Figure 3.2 shows this orientation along an imaginary line that represents the magnetic field. The drift velocity u_d of Lyutikov et al. (1999a) arises from the cyclotron-Cherenkov mechanism operating in a weakly inhomogeneous magnetic field.

Interestingly, our pulsational model suggests a natural mechanism for polar-
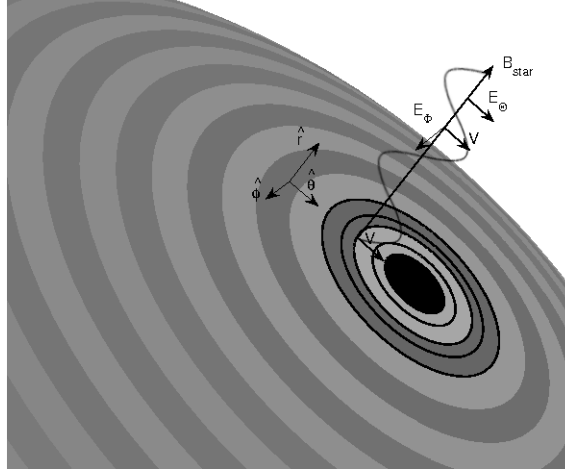
Figure 3.2: The polarization geometry near the surface of a neutron star. The magnetic field B_{star} extends outward, normal to the stellar surface. The electric field has two components: $E_{\hat{\theta}}$ points in a longitudinal direction and $E_{\hat{\phi}}$ is oriented in a latitudinal direction with respect to the magnetic pole. The dominant velocity vector $\vec{v}$ points in the $\hat{\Theta}_{mag}$ direction, toward and away from the magnetic pole.

ization in the $\hat{\Phi}_{mag}$ direction using $\vec{E} = \vec{v} \times \vec{B}$. The pulsations we introduced in Clemens & Rosen (2004) are all $m = 0$ non-radial modes centered on the magnetic pole. For non-radial g-modes, the dominant pulsational motions are horizontal, which for m=0 modes means the displaced material has a velocity $v_{\theta} \propto \frac{\partial \Psi}{\partial \theta} \frac{\partial cos(\omega t)}{\partial t}$ (Dziembowski, 1977). Thus, in our oblique pulsator model, the dominant velocity v_{θ} is directed toward and away from the magnetic pole of the pulsar (Figure 3.2). If the surface material interacts with the $\vec{B}$ field, introducing transverse wiggles as shown in Figure 3.2, this would generate a transverse electric field modulation, $\vec{E} = \vec{v} \times \vec{B}$, that is also in the $\hat{\Phi}_{mag}$ direction. This suggests that the polarization mode under consideration could be modulated in synchronism with the pulsational velocities, whose magnitudes determine the size of the modulating $\vec{E}$ field. It also raises the question of whether the pulsations could themselves operate as the wiggler mechanism of Fung and Kuijpers. The subpulses we consider in this paper have frequencies too low ($\propto$ 30 Hz) relative to the radio emission frequencies for this to work, unless there are also

unresolved high frequency oscillation modes present. For the Cherenkov drift emission mechanism, the transverse motions of the $\vec{B}$ field can modulate the drift velocity if there is an inhomogeneity in the charged particle distribution in the $\hat{\Theta}_{mag}$ direction. [1] These modulations would lead directly to a modulation in the Cherenkov Drift radiation.

Following this reasoning, we propose as a hypothesis that non-radial pulsations exactly like those we described in Clemens & Rosen (2004) can generate or interact with a second mode of radiation that is linearly polarized in the $\hat{\Phi}_{mag}$ direction and that the pulsations modulate this radiation by the surface velocities rather than the displacements. We will refer to this emission as the "velocity polarization mode". Mathematically, we model the velocity polarization mode as a time-varying amplitude of the following form:

$$A_{VPM}(t) = a_{0_{VPM}} \frac{\partial \Psi}{\partial \theta} \sin(\omega t - \psi_0), \qquad (3.2)$$

which incorporates the time derivative and the θ derivative of Equation 3.1, as appropriate for horizontal pulsation velocities. This equation is analogous to the V_θ in Equation (3) of Dziembowski (1977). The ϕ_0 term is identical to the one in Equation 3.1, because it is the phase offset for the same pulsation. We have dropped the delay term because disturbances in the $\vec{B}$ field propagate to the emission zone at the Alfvén speed, which is near c. Gil (1983) have shown the emission altitude to be 10-100 times the neutron star radius, which means that the modulations will be a near instantaneous representation of the surface velocities.

Technically, the units of Equation 3.2 are different from Equation 3.1, but we treat both of them as unitless, time-varying amplitudes of the polarized electromagnetic radiation. The meaning we attach to negative values of Equation 3.2 is

---

[1]The transverse motions of the $\vec{B}$ field we propose are equivalent to introducing a time dependent v_r into equation 72 of Lyutikov et al. (1999b).

different from that for Equation 3.1, and model dependent. Negative velocities represent a 180° change in the polarization angle of this mode rather than a reduction of the intensity to values below zero. This strategy for interpreting the amplitudes is model dependent; if our reasoning about the emission mechanism is wrong, then a different approach may be required to match the observational data. We shall see that for PSR 0943+10 at least, our model generates a satisfactory fit to the observations.

Once more, the situation is analogous to the white dwarf pulsators. The displacements responsible for surface heating and flux changes in oscillating white dwarfs are primarily horizontal, as discussed by Robinson et al. (1982), and can be represented by a formula like our Equation 3.1. More recently, van Kerkwijk et al. (2000) have detected the horizontal velocities associated with these pulsations via radial velocity variations. These variations arise from the horizontal surface motions viewed at the limb of the star (Clemens et al., 2000). As expected, they cause spectral line shifts that follow Equation 3.2, although we can only see an integral over the observed hemisphere of the star.

3.2.3 Cross Terms

It is reasonable to ask if our model should allow so clean a separation of two different effects of pulsation on two separately-generated types of radiation. Arguably, modulation of the surface plasma emission as described by Equation 3.1 should cause variations in both orthogonal polarization modes; resolution of this question depends upon specific details of the unknown emission mechanisms. Cross terms between Equation 3.1 and Equation 3.2, and other complications, are certainly plausible. We have chosen to present the simplest model that is consistent with the data presented in this paper. If subsequent pulsar measurements demand cross terms, then they will be telling us something about the emission mechanism itself or the validity of our pulsational model.

3.3 Observed Quantities

To convert the amplitudes in Equations 3.1 and 3.2 into observable quantities, we use the following transformations to calculate Stokes parameters in the frame of the star:

$$I = <A_{DPM}>^2 + <A_{VPM}>^2 \tag{3.3}$$

$$Q' = <A_{DPM}>^2 - <A_{VPM}>^2 \tag{3.4}$$

$$U' = 0 \tag{3.5}$$

This is equivalent to assuming that the orthogonal polarization modes are completely linearly polarized, and that their superposition generates the emission we observe. When one or the other mode dominates, the fractional linear polarization is high, and the polarization angle follows the dominant mode; when the two modes have equal amplitudes, complete depolarization occurs. We have not included circular polarization in the model presented in this paper.

The choice of prime notation for Q' and U' follows the usage of Deshpande & Rankin (2001), who use primed coordinates to refer to observed orthogonal polarization modes with the rotating vector model removed (i.e. converted to the non-rotating frame). Translating from the primed quantities into the observers frame requires incorporating the changing longitude we observe as the star spins and imposing rotation of the polarization angle so that the polarization of DPM follows the changing direction of the magnetic pole, given as

$$\chi_{model} = \chi_o + tan^{-1} \frac{\sin(\alpha)\sin(\phi - \phi_o)}{\sin(\alpha + \beta)\cos(\alpha) - \cos(\alpha + \beta)\sin(\alpha)\cos(\phi - \phi_o)} \tag{3.6}$$

Since the total linear polarization does not change with the frame of reference:

$$L = \sqrt{Q'^2 + U'^2} = \sqrt{Q^2 + U^2} \tag{3.7}$$

then Q' and U' can be rotated into Q and U using the following transformation:

$$Q = L\cos(2\chi_{model}) \tag{3.8}$$

$$U = L\sin(2\chi_{model}) \tag{3.9}$$

And we have to make ϕ and θ functions of time as follows:

$$\phi = \frac{t}{P_1}360 \tag{3.10}$$

$$\theta = \cos^{-1}(\sin(\alpha)\cos(\phi - \phi_o)\sin(\alpha + \beta) + \cos(\alpha)\cos(\alpha + \beta)) \tag{3.11}$$

3.3.1 The Observed Pulse Window

Our model treats the pulsations as global oscillation modes of the neutron star, which means that they can modulate emission coming from any location on the neutron star. However, neutron stars are observed to emit radiation only from the region surrounding the magnetic poles. The theoretical explanation for this is generally framed around the Goldreich & Julian (1969) aligned rotator model, in which charged particles can escape only from the polar regions.

In order to make quantitative comparisons between our model and observations, we have to impose an emission "window", analogous to the observed "pulse window", that is separate from the pulsation model, and limits the effects of pulsations to the regions that are observed to emit. For this purpose we have imposed upon I, Q and U a "window function" that is zero in those portions

of the pulsar spin when the star is off, and is a Gaussian function with a maximum of unity in the emitting region. Observations show that this window is not necessarily centered on the longitude of the magnetic pole (Johnston et al., 2005). Therefore, center longitude ϕ_{mean} and the width σ of this function are free parameters, and increase the fitted parameters in the model by two. However, ϕ_{mean} and σ are fit to the average pulse shape instead of individual pulses, as described in §3.4.2.

3.3.2 *Qualitative Behavior of the Model*

Figure 3.3 is an extension of Figure 2.2 from the previous chapter, and shows how the variety of observed average pulse shapes can be generated by changing the viewing geometry (impact parameter β). The panels in Figure 3.3 show the averages of the square of the displacement and velocity polarization modes (generated using Equations 3.1 and 3.2), along with the total intensity. The panels on the left show models dominated by the displacement polarization mode. The pulse shapes are similar to those in the previous chapter (§2), and the subpulse phase still changes by 180° at the nodal lines. There are several differences between the panels on the left and those in Figure 2.2 for the same values of β. In the previous chapter, the amplitude of the displacements was modeled using a simplified version of Equation 3.1; now we convert the displacement into Stokes' parameters to model the intensity, which is related to the square of the amplitudes. So in the case of a displacement polarization mode dominated model in Figure 3.3, the average pulse shape is described by the square of Equation 3.1 rather than just Equation 3.1 as in Figure2.2. Furthermore, we have added the window function described in §3.3.1, which suppresses intensity at the edges of the profile. So, for example, a sightline that crosses directly through the magnetic pole ($\beta = 0°$) normally gives an average profile with 5 components, like the top panel in Figure 2.2 or as in the fit to the average profile of PSR 1237+25 in Figure 2.9. However, the addition of the window function suppresses the
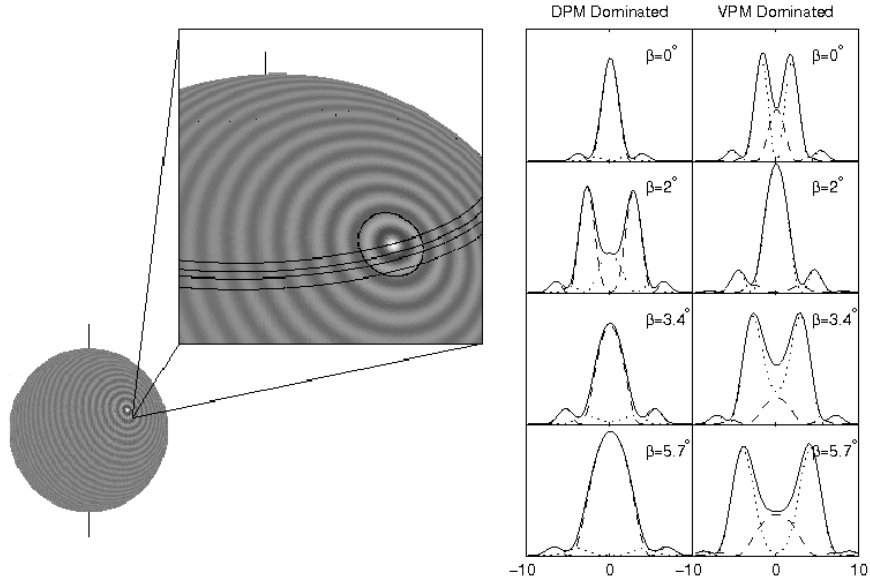
Figure 3.3: The variety of observed average pulses as a function of changing β created from the two orthogonal polarization modes. In the panels, the solid line represents the total intensity and the dashed and dotted lines represent the square of the displacement (Equation 3.1) and velocity (Equation 3.2) polarization modes, respectively. The panels on the left show a model dominated by the displacement polarization mode and the panels on the right show a model dominated by the velocity polarization mode. Both models have $\alpha = 50°$ and $l = 70$.

outer components in Figure 3.3 so that the top left panel appears to have few components. The panels on the right show models dominated by the velocity polarization mode. The panels on the right and left have the same model parameters (α, l); the difference between the two models is the ratio of $a_{1_{DPM}}/a_{0_{VPM}}$. The velocity polarization mode has its maxima at antinodes of the pulsation, and does not include time-like phase changes in the subpulses.

The drifting subpulse behavior is much richer in this model. Whereas a displacement polarization mode dominated model can show phase shifts of only $180°$, and these only at nodal lines, a model with both polarization modes has subpulse phases that also depend upon the longitude dependent amplitude ratio of the two polarization modes $(a_{1_{DPM}}, a_{0_{VPM}})$, and their fixed phase difference

(ψ_{delay}). This means that the subpulse phase can have a larger variety of longitude dependent changes. Our model predicts that these will be most pronounced in pulsars that show orthogonal mode switching. These effects can also combine with the phase shifts at nodal lines to result in phase jumps that are not equal to 180 degrees.

This model can account for many observed phenomena not explained by Clemens & Rosen (2004). For example, subpulse phase jumps that occur in only one of the polarization modes (Edwards, 2006), subpulse phase jumps that differ from 180° (Edwards & Stappers, 2003), and apparent changes in driftband slope (Esamdin et al., 2005). This model meshes in general with the observational description of subpulses in PSR 0809+74 as "the out-of-phase superposition of two orthogonally polarized drift patterns" (Edwards, 2004; Rankin & Ramachandran, 2003). Whether it can reproduce even more confused subpulse polarization behavior (e.g. PSR B0818-13, (Edwards, 2004)) is an exercise that will require careful numerical modeling like that we have done for PSR 0943+10 in this paper.

Figure 3.4 shows subpulse behavior for the two polarization modes and their combination. Panel a shows a model dominated by the displacement polarization mode. The individual pulses are at the top and the average pulse shape is at the bottom. The model in Clemens & Rosen (2004) is the special case of the model presented in this paper in which there is only the displacement polarization mode present. Therefore panel a shows exactly the same behavior of models in Clemens & Rosen (2004). Panel b is the behavior the velocity polarization mode, which is orthogonal and the derivative of, the displacement polarization mode. Panel c is a combination of the two polarization modes, with a ψ_{delay} of $\pi/8$. In this situation, there appears to be two different subpulse frequencies, P_2, and two corresponding different drift rates, P_3. However, this model still has only one single, stable subpulse frequency. Panel d is the same as panel c except that ψ_{delay} is now $\pi/2$. Note that the way the individual modes combine to form the average pulse shape in I now depends upon the relative amplitudes and phases
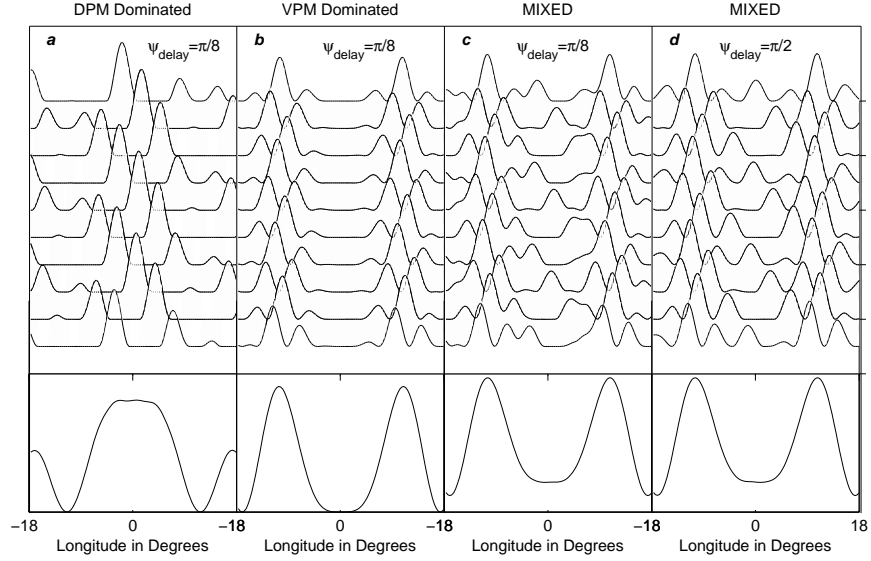
Figure 3.4: Individual subpulses for (left to right): a displacement polarization mode dominated model, a velocity polarization mode dominated model, a model with both polarization modes present. The average of the pulses is at the bottom of each panel

of the drifting subpulses in each polarization mode.

3.4 Quantitative Fitting of PSR 0943+10

In this section we discuss our analysis of archival data PSR 0943+10 and show that our non-radial oscillation model can quantitatively reproduce the observed phenomena. We organize our work as follows: In §3.4.1 we highlight significant subtleties in the data that were not mentioned in Deshpande & Rankin (2001), namely a small change in the subpulse frequency, a splitting in the driftband when it is folded at P_3, and effects of the stochastic pulse height distribution. Deshpande & Rankin (2001) detect a modulation of the subpulses in a small portion of the data which bolstered support for their drifting spark model. We find that the amplitude modulation, while present in that specific subsection of

the data, is not seen in any other part of the data and is likely the result of the drastic pulse amplitude variation intrinsic to the pulsar. In §3.4.2 we discuss the amplitude modulation properties in the data that make it difficult to model and our attempt to circumvent these problems. We then use Gaussfit, least-squares approximation software, to fit the free parameters to the data. In §3.4.3 we compare our model to the data and discuss the behavior of the model and sources of error in the fitting.

3.4.1 *Data Analysis*

The 430 MHz data of PSR 0943+10 that we examine in this chapter is the same data analyzed by Deshpande & Rankin (2001). We refer to the reader to their paper for most of the data analysis, which we do not repeat here except for those instances where we find significantly different behavior of the star. Deshpande & Rankin (2001) use four basic tools in their analysis: synchronous folding of the data, the Fourier transform, the longitude resolved fluctuation spectrum, and the harmonic resolved fluctuation spectrum. When synchronously folding the data at a given period, usually P_3, the subpulses drift through the pulse window at each successive spin until they repeat in longitude, thus creating a driftband plot. The longitude resolved fluctuation spectrum, first introduced by Backer (1973), is a Fourier transform calculated at each longitude. The harmonic resolved fluctuation spectrum is a Fourier transform of the time series stacked at the spin frequency. Edwards & Stappers (2002) have shown that the combination of the longitude and harmonic resolved fluctuation spectra present the same information as a two-dimensional Fourier spectrum. While we have also calculated the two-dimensional Fourier spectrum, we do not present it here because it is less familiar and not directly comparable to the Deshpande & Rankin (2001) analysis. Deshpande & Rankin (2001) also use an algorithm for separating the polarization modes, and conduct analysis on each polarization mode individually, but we do not repeat the analysis, as discussed later in this section.
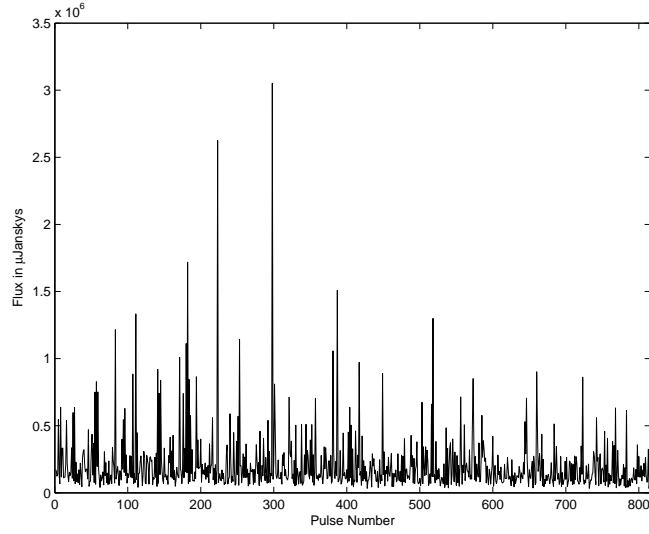
Figure 3.5: Distribution of pulse amplitudes in PSR 0943+10. The 430 MHz data, courtesy of Joanna Rankin, was taken using Arecibo in 1992.

The most difficult aspect of modeling PSR 0943+10 is the large stochastic variation in the pulse amplitudes. The signal-to-noise for each pulse, where the noise is measured from the off-pulse regions of the synchronous measurements, averages to be about 6 for the entire data set, but ranges from 0.94 to 101.83. The standard deviation in the noise is 410.87 μJanskys while the standard deviation in the data is 3.22×10^4 μJanskys. From this, we can conclude the large variations in pulse height, as shown by the pulse height distribution given in Figure 3.5 are due to stochastic variations of the pulsar, not instrumental noise. Indeed, Cordes (1978) has argued that pulsar subpulses are amplitude modulation of shot noise-like emission.

Driftbands

We now explore the subtleties in the driftband because changes in the shape of individual subpulses as a function of longitude will appear using this method of analysis. In the perspective of our non-radial oscillation model, the delay between the two orthogonal polarization modes can creates interesting behavior. In this

section, we describe significant structure in the driftband which was overlooked in previous published analyses.

The subpulses in PSR 0943+10 drift through the pulse window at a regular period, P_2. If an imaginary line is drawn through the maximum of each subpulse in consecutive spins of the star, it would trace out a shallow curve through the consecutive pulse windows and spanning the pulse window, creating a driftband. The driftband starts at a given longitude and continues on until the subpulses arrive back at the starting longitude many spins of the star later; the time it takes for a subpulse to return to its original longitude is P_3. The driftband then repeats at intervals of P_3 through the length of the data set. An easy way to display this behavior is to fold the data at P_3, essentially stacking all the driftbands on top of each other. In terms of the rotating spark model, as the sparks rotate uniformly around the magnetic cap, they should produce a smooth driftband. As evidence of this, Deshpande & Rankin (2001) shows a smooth driftband of all 816 pulses. However, we find there is significant, interesting behavior in the driftbands that may be difficult to explain with the rotating spark model.

In the driftbands shown by Deshpande & Rankin (2001) for the entire 816 pulses, they have removed an "aperiodically fluctuating base" from the data before folding it at P_3. We do not remove this base as in doing so may remove other frequencies not related to the subpulse or spin frequency; furthermore, they did not describe of their method which prevents us from being able to exactly reproduce their work.

The driftband of the 816 pulses in the Stokes' parameter I shows a broadening in the driftband at positive longitudes as shown in the right panel of Figure 3.6. To explore this, we folded shorter 100 pulse segments of the data at P_3, and noticed an obvious splitting on the right side of driftband as shown in the left panel of Figure 3.6. The left panel of Figure 3.6 is a driftband of the first 100 pulses in the time series. A splitting occurs at positive longitudes. While we only show the first 100 pulses here, driftbands of other 100 pulse segments of the

94
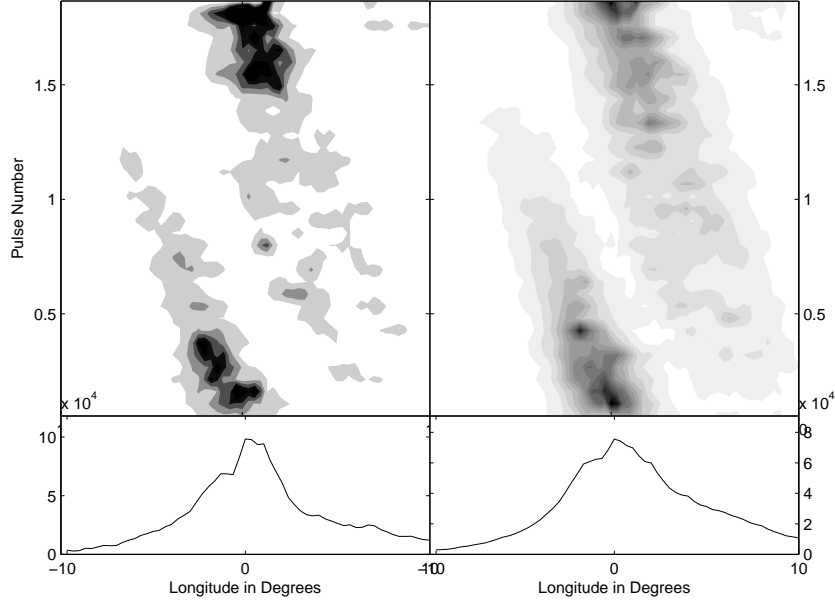
Figure 3.6: Left panel: The first 100 pulses of PSR 0943+10 folded at P_3 = 1.86584 seconds. The value of P_3 was calculated based on the value of P_2 = 31.78224, taken from the Fourier transform of the entire 816 pulses. Right panel: All 816 pulses folded at the same value of P_3.

data also display this behavior.

The splitting in the driftband is difficult to explain with the rotating spark model because it is a longitude-dependent phenomenon. In the rotating spark model, of Deshpande & Rankin (2001) in particular, in each successive spin of the star, an individual spark moves a few degrees in longitude. In PSR 0943+10, the same spark as seen on the right side of the pulse window will, in the next spin of the star, have moved to the left of the pulse window. The splitting in the driftband indicates that the spark must be split when it is present on the right side of the pulse window and that it recombines when it moves to the left side. Since the splitting persists for many spins, it indicates that all sparks must have this behavior of splitting at one longitude and recombining at another. This is difficult to explain with the rotating spark model without the introduction a new phenomenon, but we will show it is a natural result of the phase difference between the displacement and velocity polarization modes, ψ_{delay}, in our model.

Fourier Transform

Just as we find structure in the driftbands not seen by Deshpande & Rankin (2001), we also find structure in the Fourier transform because we use all 816 pulses in the Fourier transform to get the maximum resolution possible for this data set. A highly-resolved Fourier transform of the entire 816 pulses shows a splitting in the subpulse frequency. When computing the Fourier transform for smaller, consecutive subsets of the data, we find that the frequency wanders throughout the whole data set.

The Fourier transform is an ideal tool for picking out periodic frequencies in data that are either highly aliased and/or appear to be random. The resolution of the Fourier transform is $1/2T$ where $T = 895.64$ is the timescale in seconds. A Fourier transform of the entire 816 pulses shows the subpulse frequency to be split (overlooked by Deshpande & Rankin (2001)). We will see that it is impossible with the limited data in this data set to determine whether the double peaks are due to an amplitude modulation of a single subpulse frequency or whether the subpulse frequency is two closely spaced independent frequencies. The presence of two independent frequencies would require additional complexity in the rotating spark model. However, our non-radial oscillation model would naturally allow for two or more simultaneous frequencies. Indeed, the existence of multiple frequencies is a prerequisite to astroseismology of neutron stars. Thus it is important to acquire additional data on this star to see if the pattern is repeatable.

When computing the Fourier transform of the data Deshpande & Rankin (2001), in addition to removing a "base", use the average of "three successive, overlapping 256-pulse Fourier transforms" (where they have padded the off-pulse regions with zeros). The average of the transforms is then used to plot the harmonic resolved fluctuation spectrum (see below). For 256 pulse transform, the resolution is 0.001785 Hz, which is not fine enough resolution to identify the splitting in the subpulse frequency.
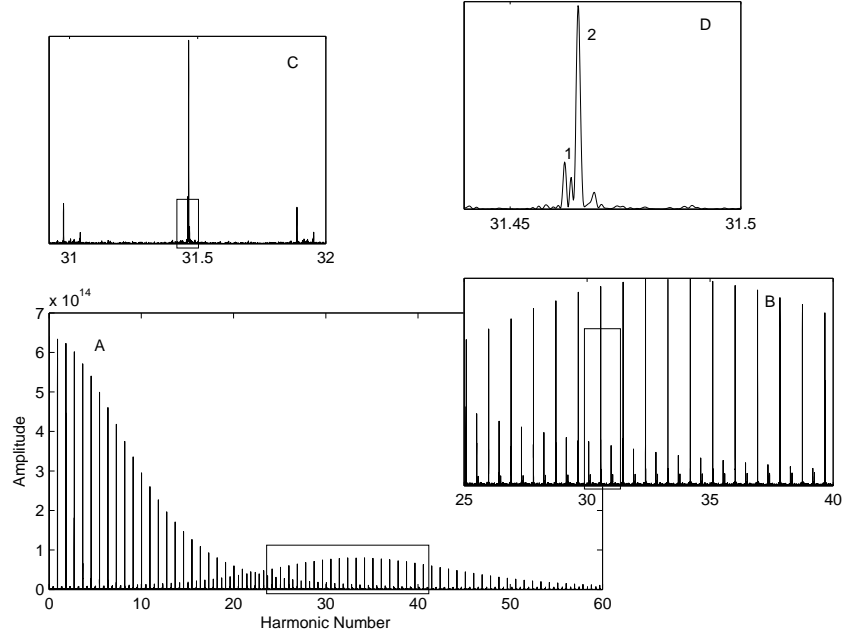
Figure 3.7: The Fourier transform of all 816 pulses using QSFT. Panel (A) shows the transform up through the first 60 harmonics. Each successive panel enlarges the area of the transform, eventually focusing on the subpulse period in panel (D). The subpulse frequency is split into 2 peaks, labeled according. The spacing between the two peaks is an order of magnitude greater than the resolution of the Fourier transform.

The software package QSFT, written by Carl Hansen for the Whole Earth Telescope (Nather et al., 1990), computes the slow Fourier transform for time series data. QSFT is ideal for computing the Fourier transforms for this pulsar data because it expects segments of data at regularly spaced intervals and does not require there to be an integer number of time intervals δt between each data segment. The bottom panel (A) of Figure 3.7 shows the Fourier transform up through the 60th harmonic of all 816 pulses of PSR 0943+10 using QSFT. Using all 816 pulses give the Fourier transform a resolution of $1/2T = 0.000183$ Hz, ten times greater than the resolution of a 256 pulse Fourier transform. A closer inspection of the subpulse frequency in the top panel (D) of Figure 3.7 show that the peak is split into two peaks. The peaks in this panel are representative of all the aliased subpulse peaks. The larger of the two peaks (peak 2) is at

31.464703784 Hz, which is not the largest subpulse alias in panel (A). We have chosen this peak as the subpulse frequency due because this peak shows an integer relation to the second and third harmonics which are not shown in Figure 3.7. The location of the smaller peak is at 31.46179786 Hz (peak 1); the difference in the two peaks is 0.0029 Hz. This difference in frequency would be barely visible in a 256 pulse Fourier transform, especially if several transforms were averaged together which could broaden the subpulse frequency.

To explore the frequency splitting in the time domain, we divided the data into smaller, sequential sets of 50 pulses each. Fourier transforms of these smaller subsets of data can still clearly find the subpulse frequency, but they do not have the frequency resolution to separate the subpulse frequency into the two distinct peaks. Instead, we used Gaussfit (described in §3.4.2) to fit the unitized intensity (Stokes I) of each subset to a function $I = A\cos(\omega t - \psi)$. We used the dispersion in the data as the variance. The frequency change (ω) with subset is shown in the bottom panel of Figure 3.8 and the corresponding amplitudes (A) are shown in the top panel.

The frequency in Figure 3.8 wanders in a significant fashion. The splitting in the Fourier transform and the cyclic wandering in the smaller subsets of the data could be due to either a closely spaced second frequency or a combined frequency and amplitude or phase modulation. If the subpulse frequency is solely amplitude modulated and we then repeat the fits using Gaussfit, but with a fixed subpulse frequency (ω), the phase (ψ) would remain stable. If the subpulse frequency is actually two closely spaced frequencies, a repeat of the fits with Gaussfit would result in a periodic wander of the subpulse phase. We averaged the subpulse frequencies in Figure 3.8 and then fit each of the 50 pulse subsets with Gaussfit with the same function $I = A\cos(\omega t - \psi)$, but with $\omega = 31.464485029$ Hz. The resulting phase as a function of time is shown in the bottom panel of Figure 3.9 and the corresponding amplitudes are in the top panel. Since it appears that the subpulse frequency and phase wander through only one or two cycles, we cannot
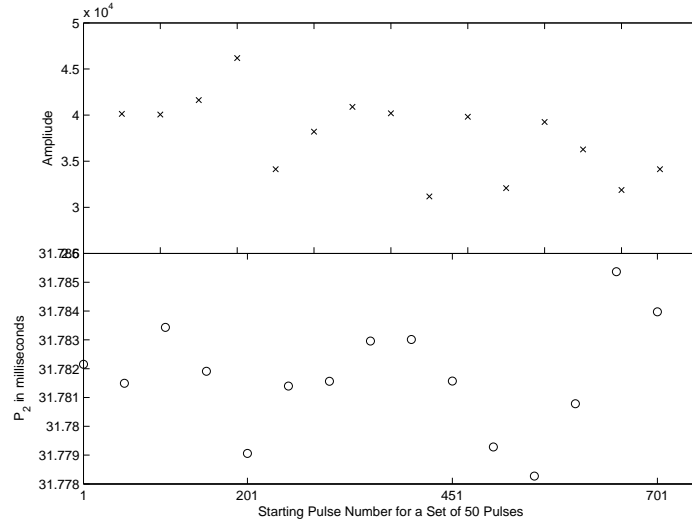
Figure 3.8: The results of fitting consecutive 50 pulse segments of the data with Gaussfit to the function $I = A\cos(\omega t - \psi)$. Bottom panel: The fitted value of the frequency for each 50 pulse segment. Top panel: The corresponding fitted amplitude for each 50 pulse segment. The error bars are not included because the error is significantly small that they are not visible within the resolution of this plot.

conclusively determine whether the split peak is two closely spaced peaks or an amplitude modulation with an associated frequency or phase modulation.

It is worth noting that a Fourier transform of the unitized data had no effect on the splitting of the peaks. (The unitization method is described in §3.4.2.) If the two peaks were due to an amplitude modulation, the unitization of the individual pulses would not show a split peak as the unitization would remove any amplitude modulation. The fact that the splitting of the peak remained indicates, but does not conclusively lead us to believe that the peaks are two closely spaced independent frequencies. We would need to repeat these analyses for a longer continuous portion of the data and for an independent data set to determine conclusively the presence of two independent frequencies.

99
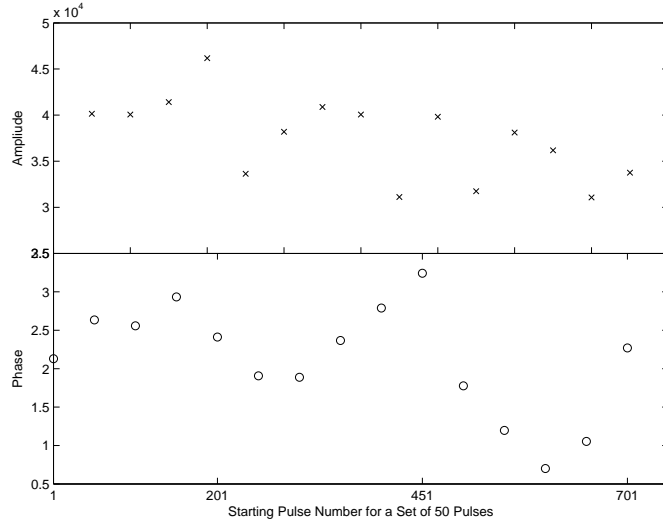
Figure 3.9: The results of fitting consecutive 50 pulse segments of the data with Gaussfit to the function $I = A\cos(\omega t - \psi)$ where the subpulse frequency is kept fixed. Bottom panel: The fitted value of the phase for each 50 pulse segments using Gaussfit. Top panel: The corresponding fitted amplitude for each 50 pulse segments. The error bars are not included because the error is significantly small that they are not visible within the resolution of this plot.

Longitude and Harmonic Resolved Fluctuation Spectra

Stochastic variation in the pulse amplitudes complicate attempts to extract any underlying signal for comparison to our model. While stochastic variation averages away in the driftbands and affects primarily the amplitudes in the Fourier transform, it can have large effects over short segments of the data in the longitude and harmonic resolved fluctuation spectra. Within this data set, Deshpande & Rankin (2001) have detected a periodic amplitude modulation in the region of pulses 129-384 of the data. The amplitude modulation was a key component for increasing confidence in circulating spark model, and Deshpande & Rankin (2001) interpret it as a persistent pattern of brightness in the circulating sparks and use it to confirm the existence of twenty distinct sparks. A single frequency pulsation model cannot reproduce either the stochastic variations in the pulse height or the amplitude modulation that produces the sidelobes. However, it is

legitimate to ask whether the appearance of symmetric sidelobes in a subset of the data is not consistent with stochastic amplitude variations alone, rather than indicative of a periodicity in the star that should be fitted by models.

The amplitude modulation can be seen in the longitude and harmonic resolved fluctuation spectrum of that region in the left panels of Figures 3.10 and 3.11. In Figure 3.10, the aliased subpulse frequency is at about 0.43 Hz. The panel on the left shows two sidelobes about this peak. In Figure 3.11, the subpulse frequency is at 0.49 Hz. The amplitude modulation is arguably present in the left panel; a peak on the right appears near the 30th harmonic and a peak on the left appears at low harmonic number. The sidelobes which result from the amplitude modulation seen in this section of the data are not present in the other sections of the data. For comparison purposes, we show the next 256 pulses (pulses 256-512) in the right panels of Figures 3.10 and 3.11.

In addition, the sidelobes about the subpulse frequency appear symmetric in the average of the harmonic resolved fluctuation spectrum over all harmonics are actually asymmetric in harmonic number. As can be seen in the right panel of Figure 3.11, the low and high frequency sidelobes appear at harmonic numbers 10 and 35, respectively. According to Deshpande & Rankin (2001), the amplitude modulation which creates the sidelobes occurs at $20P_3$. We created simulations with a strictly periodic subpulse, but allowed the amplitude of the subpulse to vary with a period of $20P_3$. As expected a single subpulse frequency with a modulated amplitude creates sidelobes about the subpulse frequency, and about all other significant peaks, including the harmonic of the subpulse and spin frequencies, and the DC offset at zero frequency. Furthermore, in our simulations, the sidelobes are symmetric in harmonic number at the same frequency of the peak they are modulating. While we do not dispute that the sidelobes seen in pulses 129-384 are due to an amplitude modulation, a stable time varying modulation with the period of twenty circulating sparks would produce behavior in the harmonic resolved fluctuation spectrum that is different from what is
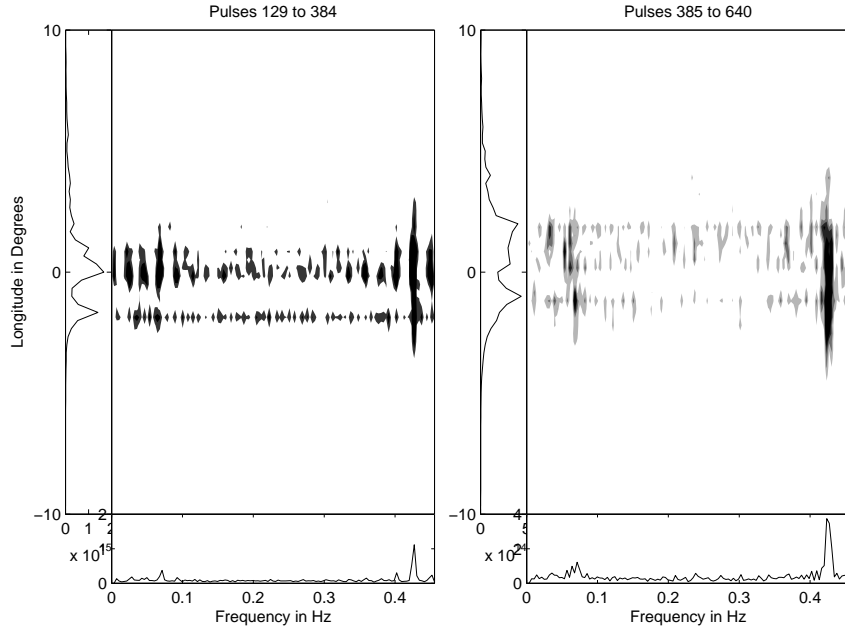
Figure 3.10: The longitude resolved fluctuation spectrum for two consecutive 256 pulse segments of the data from PSR 0943+10. Left panel: The subsection of the data (pulses 129-384) where Deshpande & Rankin (2001) discovered the tertiary modulation which supports the rotating spark model. Right panel: The longitude resolved fluctuation spectrum for the next portion of the data (pulses 257-512); the tertiary modulation is not present.

observed.

3.4.2 *Simulations*

Departing now from new phenomena uncovered by our analysis, we address the central purpose of this work in this section, which is whether or not our pulsational model can reproduce the observations. We will show that it is possible to reproduce not only the subpulse frequency and linear polarization behavior shown by Deshpande & Rankin (2001) but also the phenomena uncovered in the previous section.

We modeled the displacement polarization mode according to 3.1 and the velocity polarization mode using 3.2. From these two polarization modes, we
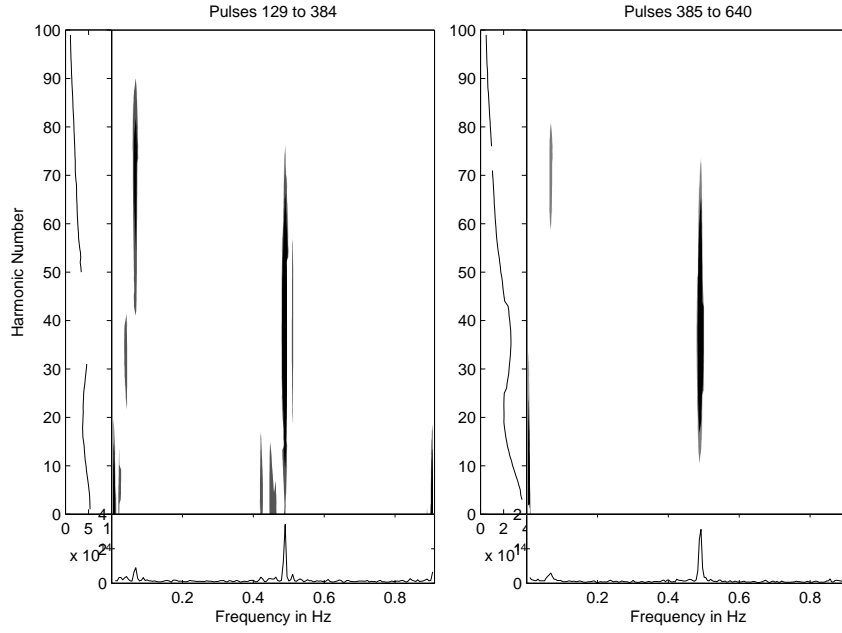
Figure 3.11: The harmonic resolved fluctuation spectrum for the same two consecutive 256 pulse segments of the data from PSR 0943+10 as in Figure 3.10. Left panel: The subsection of the data (pulses 129-384) where Deshpande & Rankin (2001) discovered the tertiary modulation. Right panel: The harmonic resolved fluctuation spectrum for the next portion of the data (pulses 257-512); the tertiary modulation is not present.

created the Stokes parameters outlined in §3.3 so that we could directly compare our model to the Stokes' parameters taken at a telescope. In order to conduct a quantitative comparison of our model to the data of PSR 0943+10 described in §3.4.1, we used Gaussfit, a robust least-squares approximation package [2] to obtain values of the free parameters. Our model is able to reproduce the behavior of PSR 0943+10: the average pulse shape and drifting subpulses, orthogonal polarization modes, the splitting in the driftband, and the features in the Fourier transform. We could add stochastic variation to our simulated data, but by its nature, stochastic variations would take an infinite amount of time to fit quantitatively. Therefore, we attempt to reduce the effect of the large pulse height distribution

---

[2]http://clyde.as.utexas.edu/Gaussfit.html

in our quantitative comparison of our model to the data. We fit the average pulse shape to determine the window function and the individual pulses to determine the model parameters.

To reduce the effect of the stochastic pulse height variation on our fit of the individual pulses, we "unitize" the data. To do this, we create an average pulse shape with a maximum of one. We then scale each individual pulse so that its maximum has an amplitude of the corresponding longitude in the unitized average pulse. Furthermore, since our model does not include circular polarization, we remove it from the data by constructing a new I where $I_{new} = \sqrt{I^2 - V^2}$.

Once we have built a unitized data set, we can fit it with the model based on the two orthogonal polarization modes. However, the unitized data is sparsely sampled due to the nature of pulsars; we receive a pulse of data once every spin period of the star (see §1). Furthermore, each pulse appears to be the strongest in the center of the pulse window, presumably due to the closest approach of the magnetic pole. Our simulated data, though, is a continuous stream of pulses constructed from Equations 3.1 and 3.2. To mimic the pulse window created by the spin of the pulsar and its magnetic axis sweeping by our line of sight, we impose a window function (described in §3.3.1) on our simulated data every interval of P_1 and of the same length in time as the pulse window. Any simulated data that falls outside the pulse window is set to zero.

The unitized average pulse shape that we construct provides the parameters for the window function that we impose on our model. We have chosen to use a Gaussian curve as our window function as it has the same general shape as the unitized average pulse shape. Other choices for the shape of the window function are possible, but have little effect in the fit of the data to the pulsation model. We define the Gaussian curve with unity amplitude as given by:

$$g = e^{-(\phi - \phi_{mean})^2/(2\sigma)^2} \tag{3.12}$$

We start with a window spanning $20°$ and use Gaussfit to fit a unitized average

pulse shape with a maximum of one and its variance, taken from the instrumental noise. For this data, Gaussit determines ϕ_{mean} and σ in Equation 3.12 to be 0.55° from the center of the profile and 0.05665, respectively. The χ^2 is 359, which we expect to be large since the average pulse profile is asymmetrical.

After imposing this window function on our time series, we fit the time series data to our pulsational model. The χ^2 of the fit is based on a variance calculated from the on-pulse variations, namely the dispersion in the data which always results in a χ^2 of approximately one. The resulting χ^2, in comparison with fits with various fixed parameters and different portions of the data, indicates the robustness and consistency of the fit.

We divided the data into 100 pulse segments, initially fitting the first 100 pulses. Fixing β, α/β and ϕ_o, our analytic model in Gaussfit fit seven parameters: $a_{0_{DPM}}$, $a_{1_{DPM}}$, $a_{0_{VPM}}$, ω, ψ_0, ψ_{delay}, and χ_o using the following algorithm:

- Calculate $A_{DPM}(t)$ and $A_{VPM}(t)$ using Equations 3.1 and 3.2, respectively, where we supplied initial guesses for the free parameters. We used the Fourier transform to determine guesses for the subpulse frequency, the drift-band plots to guess ψ_{delay}, and for the other parameters we made initial guesses by eye.

- Modulate $A_{DPM}(t)$ and $A_{VPM}(t)$ by the window function described in Equation 3.12.

- Calculate I_{model}, Q'_{model}, and U'_{model} using Equations 3.3, 3.4, and 3.5, respectively.

- Compute the polarization angle χ from Q'_{model} and U'_{model} and add the polarization angle swing from Equation 3.6.

- Since the linear polarization (L) is the same regardless of reference frame, rotate into Q_{model} and U_{model} space by:

$$Q_{model} = L\cos(2\chi); \qquad (3.13)$$

105

$$U_{model} = L \sin(2\chi); \tag{3.14}$$

- Minimize the following equations:

$$I_{model} - I_{new} = 0 \tag{3.15}$$

$$Q_{model} - Q_{data} = 0 \tag{3.16}$$

$$U_{model} - U_{data} = 0 \tag{3.17}$$

Using this procedure, Gaussfit successfully converged on a solution for the first 100 pulses. We found that the parameters could be easily divided into geometrical and pulsational parameters and that the solution was independent of the geometry of the star. The geometrical parameters, namely α, β, χ_o, and ϕ_o, are closely related, as discussed in §3.4.3. To match the polarization angle swing, the actual values of α and β are irrelevant; it is the ratio of α/β that is significant. Furthermore, ℓ and β are also correlated and either parameter can be adjusted to match the average pulse shape. Given the ratio of α/β and an assumed value of ℓ, we tested the dependence of the pulsational parameters on the geometrical parameters by repeating the procedure in listed above for various values of β. We surmise that β is limited to the first two nodal regions; the polarization angle swing is not sharp enough to indicate that our sightline passes through core region of the magnetic pole, and a lack of any pulsars that show more than five components indicates that in general magnetic polar caps have no more than two nodal regions. The imposed window function discussed above and in §3.3.1 ensures that the average profile only has a single peak and the lack of any subpulse phase jumps in the data indicates that our sightline does not cross any nodal lines.

To test the robustness of the solution, we then repeated the fit for the same 100 pulses for several values of β in the first two nodal regions, ranging from 2.29° to 5.42° in 0.57° intervals for different values of ϕ_o. Figure 3.12 shows the nodal structure of the star as function of the impact parameter, β. The magnetic
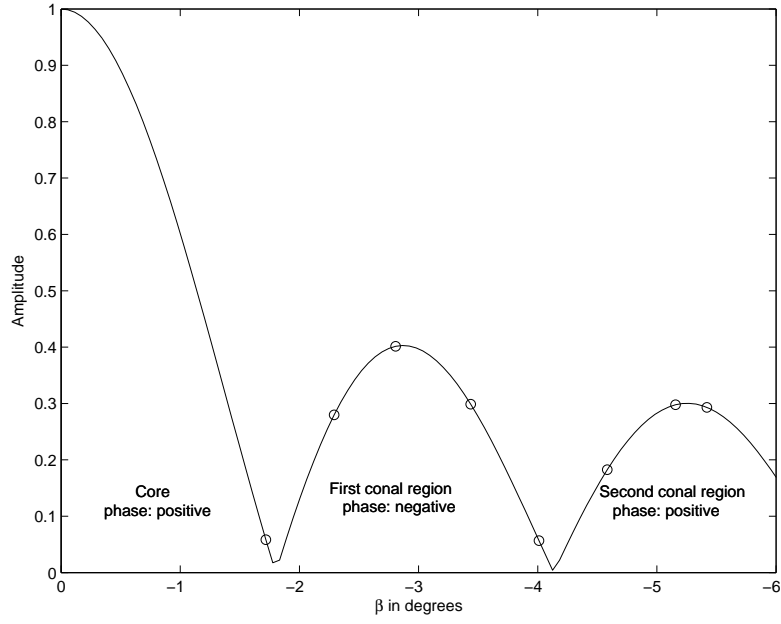
Figure 3.12: The nodal structure of the model of PSR 0943+10 with $l = 75$. The magnetic pole is at $\beta = 0°$, the nodes are at about $-1.8°$ and $-4.1°$, and the antinodes are at $-2.9°$ and $-5.2°$. The circles indicate values of β used in the Gaussfit.

pole is at $\beta = 0°$, the nodes are at about $-1.8°$ and $-4.1°$, and the antinodes are at $-2.9°$ and $-5.2°$. The circles indicate values of β used in Gaussfit. As an example, Table 3.4.2 lists the parameters, both free and fixed, used in our model for β and ϕ_o fixed at $-2.8°$ and $0°$, respectively.

We speculate that ϕ_o, the longitude of closest approach to the magnetic pole, is near the center of the profile due to observations of PSR 0943+10 at other frequencies. At lower frequencies, the average pulse profile becomes broader and bifurcates, turning into a double profile (Asgekar & Deshpande, 2001). In terms of our model, this behavior indicates that these observations at 430 MHz place β near, but not at, an antinode and as the radio frequency decreases, β decreases (Smits et al., 2006). The decrease in β, assuming all other parameters remain unchanged, will cause our sightline to graze the antinode causing a decrease in intensity at the center of the profile. In light of this, we ran our model through

Parameter	Value	σ	Fitted/Fixed
P_1	1.097608 seconds	–	fixed
P_2	0.031782 seconds	6.101097e-08	fitted
P_3	1.87074 seconds	–	both
β	$-2.8075°$	–	fixed
α	$8.0338°$	–	both
ϕ_o	$0°$	–	fixed
χ_o	$-3.3596°$	4.427539e-03	fitted
l	75	–	fixed
$a_{0,DPM}$	0.16426	1.27606e-02	fitted
$a_{0,VPM}$	0.12544	2.58751e-03	fitted
$a_{1,DPM}$	1.21291	3.24189e-02	fitted
ψ_0	-2.26865	4.25580e-02	fitted
ψ_{delay}	1.139587	3.76759e-02	fitted
χ^2	0.93508	–	fitted

Table 3.1: The free and fixed parameters used in our model. The results are from a fit of the first 100 pulses where β and ϕ_o are fixed at $-2.8°$ and $0°$, respectively. We get the values of P_1 from the Fourier transform of the entire run. We calculate P_3 from Equation 2.4.

all the values of β shown in Figure 3.12 for values of ϕ_o of $0°$, $1°$, $2°$, and $3°$ to the right of center (to match the asymmetry in the average pulse profile), respectively.

Figure 3.13 displays the results of Gaussfit for fixed values of β and ϕ_o. The consistency of the fitted parameters and its independence from specific geometries, indicates the robustness of the fit. The absolute value of χ^2 is only a check on the fit since the variances provided for Gaussfit was from the data themselves. However, the relative values of χ^2 indicate that some fits are slightly better than others. The phase offset in Figure 3.13 shows a change of about $180°$ between the first and second nodal region. According to our model as described in §2,
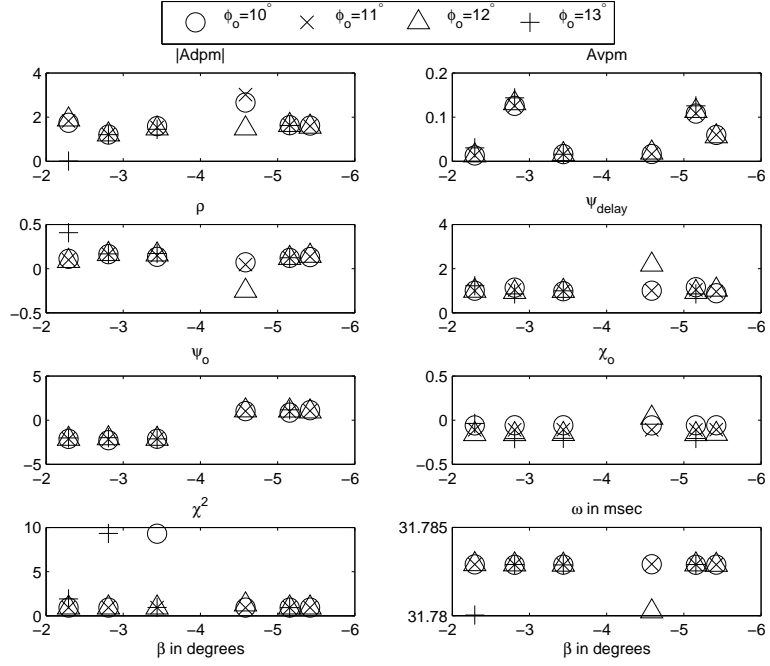
Figure 3.13: The results of Gaussfit for various values of β and ϕ_o. Each panel shows a different parameter fitted using Gaussfit. The x-axes show the values of β that were used in the fit, corresponding to the same values of β in Figure 3.12. The different symbols represent the different values of $\phi_o = 10°$, 11°, 12°, and 13°.

both the core and second nodal region have the same phase while the first nodal region is 180° out of phase. As expected, the phase ϕ_o for values of β in the first nodal region was 180° different than the phase in the second nodal region.

We then chose a well-behaved solution of $\beta = -2.8°$ and $\phi_o = 0°$ and fit other sections of the data. Specifically, we took consecutive 100 pulses sections, 8 sections in all, starting from the first pulse and fit the same parameters as discussed above. Gaussfit found solutions for all sections as shown in Figure 3.14. Each data point is the starting pulse number for the data section; for example, the data point at 400 is the fit for pulses 400-500.

Most of the fitted values show no general trend. The pulsar transitions into a disorganized state at the end of pulse 816 (Deshpande & Rankin, 2001) and it was our hope that these fits would yield predictive value for the transition from
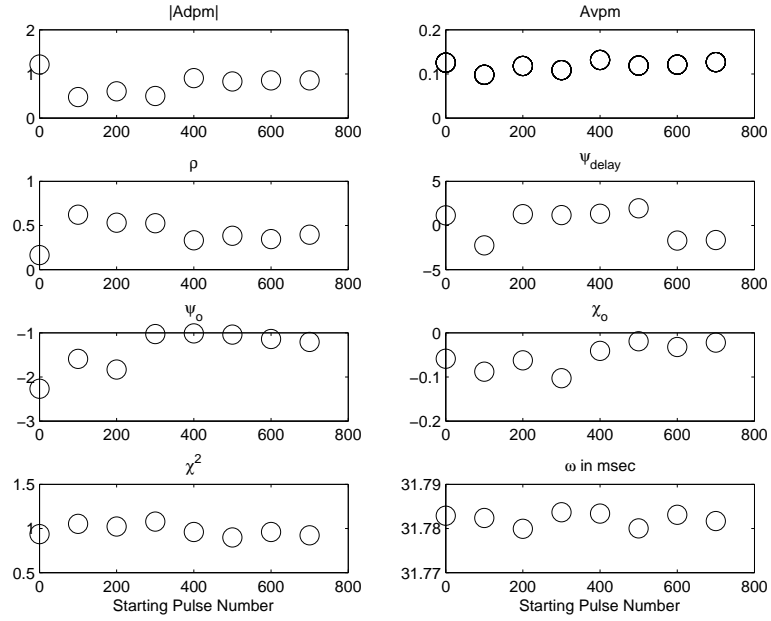
Figure 3.14: The results of Gaussfit for fixed values of $\beta = -2.8°$ and $\phi_o = 0°$. We fit eight consecutive 100 pulse segments of the data. Each panel shows a different parameter fitted by Gaussfit as a function of the pulse segments.

highly organized behavior into disorganized behavior. No such trend is seen in Figure 3.14, but these fits are for limited values of β and ϕ_o; a more extensive fitting of the parameter space is worth investigating.

3.4.3 Comparison

Fits to the Polarization Angle

Initial fits of the observed polarization angle to Equation 3.6 to determine the geometry of the star (α, β, χ_o, and ϕ_o) proved to be underconstrained. The correlation between all the parameters was very high. Attempts to circumvent this problem including fixing α (for a given $l = 75$) to ensure our viewing window was in the first nodal region, and making various guesses for ϕ_o were unsuccessful. For any given values of α and ϕ_o, a suitable β and χ_o could be found, no fit any better than another. It was apparent, however, that the

Fit 1	Fit 2	DR2001
$\beta = -2.81°$	$\beta = -5.42°$	$\beta = -4.29°$
$\alpha = 8.03°$	$\alpha = 15.51°$	$\alpha = 11.58°$
$\phi_o = 0°$	$\phi_o = 1°$	$\phi_o = 0°$
$\chi_o = -3.36°$	$\chi_o = -6.15°$	$\chi_o = 0°$

Table 3.2: The first two columns are the values of the geometrical parameters for two fits using Gaussfit (Fit 1 and Fit 2). The last column contains the values used by Deshpande & Rankin (2001) for α and β. They did not publish their values for ϕ_o and χ_o and we have therefore assumed the value for these parameters is $0°$.

ratio of α/β was consistently the same regardless of the given value of α and we preserved this ratio in subsequent fits of individual pulses. In addition to the correlation between these geometrical parameters, the values of β and ℓ are also strongly dependent on each other. For most given values of ℓ, a corresponding value of β can be found to match the average pulse window. We chose $l = 75$ because the corresponding β approximately matched other published values of β, and our qualitative models of other pulsars suggested that ℓ be near this value.

Figure 3.15 shows the Radhakrishnan & Cooke (1969) polarization angle calculated from Equation 3.6 superimposed on the polarization angle histogram of the data. The calculated polarization angle is dependent on four parameters: α, β, ϕ_o, and χ_o. We took two of the Gaussfit results mentioned in §3.4.2 and plotted their corresponding polarization angle, keeping in mind that β and ϕ_o were fixed as well as the ratio of α/β, where the ratio was determined from previous underconstrained fits that explored the geometry. The lower lines on Figure 3.15 show the two fits in Table 3.4.3 while the upper line shows the geometry used in Deshpande & Rankin (2001), where we have assumed a ϕ_o and χ_o at zero degrees.
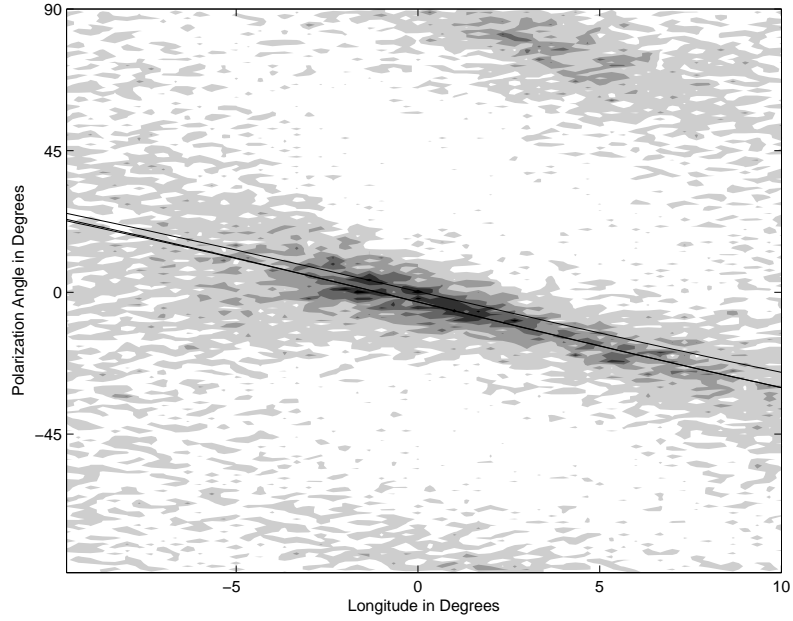
Figure 3.15: The polarization angle histogram of all 816 pulses of PSR 0943+10. The lines represent different values of α, β, ϕ_o, and χ_o. The top line is the polarization angle calculated from the values determined by Deshpande & Rankin (2001); the values are in the right column in Table 3.4.3. The bottom line is the result of the two polarization angles calculated from Fits 1 and 2 in Table 3.4.3.

Visual Comparison to Individual Pulses

Finally we make a visual comparison of our non-radial oscillation model to data. The stochastic pulse amplitudes and the unpolarized component in the data are, to some degree, unquantifiable and can only be partially fit using Gaussfit. The effect of the stochastic pulse amplitudes can be minimized via the unitization process described above. We examine the results of our fitted model parameters by looking at the driftband, the Fourier transform, and the longitude and harmonic resolved fluctuation spectra. In addition, we compare our model to the data in histogram form by creating plots similar to those used by Stinebring et al. (1984a,b).

When comparing the driftband plots from the results of Gaussfit to the data, we use the unitized data since the results of Gaussfit are based on the unitized
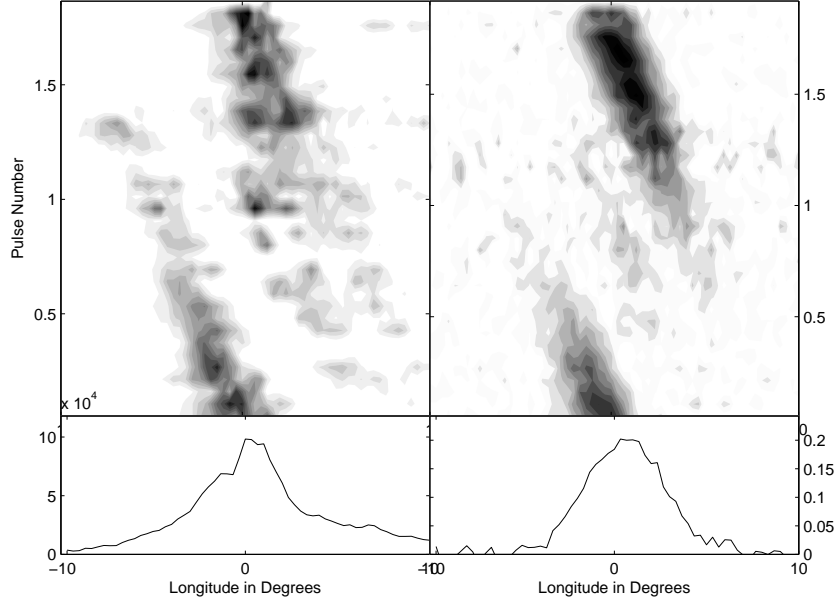
Figure 3.16: Left panel: The first 100 pulses of PSR 0943+10 folded at $P_3=$ 1.86584 seconds, as also shown in the left panel of Figure 3.6. The value of P_3 was calculated based on the value of $P_2= 31.78224$, taken from the Fourier transform of the entire 816 pulses. Right panel: Our model of the data, using the results of Gaussfit and the same values of P_2 and P_3 as in the left panel. Noise was added using off-pulse noise from the archival data of PSR 0943+10.

data. In addition to the random distribution in pulse heights, there is an unpolarized component in the data. A simple plot shows that for the average pulse profile $I > \sqrt{Q^2 + U^2 + V^2}$. Isolating and removing the unpolarized component is more complex than simply stating $I_{new} = \sqrt{Q^2 + U^2 + V^2}$ because when Q and U are equal, depolarization occurs. Therefore, it is impossible to tell how much of the unpolarized portion of I is due to unpolarized stellar emission and how much is due to a depolarization of the two linear polarization modes. Keeping these limitations in mind, we now compare our model to the data.

The left panel of Figure 3.16 is the same as the left panel of Figure 3.6: the first 100 unitized pulses in the time series folded at P_3. The longitude dependent splitting occurs at positive longitudes in the right side of the driftband. We used the parameters listed in Table 3.4.2 to create 100 pulses simulated data,

113

adding noise to the simulation from the instrumental noise in the data. The driftband created from the model is in the right panel of Figure 3.16, and like the data, it also shows a marked splitting at positive longitudes. In terms of our model, the amount of the bifurcation in the driftband is due to the phase difference, ψ_{delay}, between the displacement and velocity polarization modes. A different value of ψ_{delay} would change the amount by which the driftband is divided. The prominence of the smaller, bifurcated track of the driftband is due to the ratio of the amplitudes two polarization modes. The displacement and velocity polarization modes create the main and bifurcated track of the driftband, respectively. The relative amplitudes of the polarization modes are manifested in the relative amplitudes of the main driftband and its secondary companion. In addition, the driftband on the left side of the pulse window is not bifurcated as a result of the steep drop in intensity of the window function.

We can also make a visual comparison of our pulsational model to the data in Fourier space. We apply the Fourier transform to our noise-free simulation using QSFT. We used the model parameters in Table 3.4.2, creating the full 816 pulses to match the resolution in the Fourier transform of the data. The Fourier transform of our simulation does not show the splitting in the subpulse frequency, as discussed in §3.4.1, since we have created our model only using a single subpulse frequency. To reproduce the two closely spaced peaks, our model would require the introduction of a second, incommensurate subpulse frequency or the subpulse frequency would have to wander as a function in time be accompanied by an associated amplitude or phase modulation. Figure 3.17 shows the Fourier transform of our model. The series of peaks centered around 30 Hz is the subpulse frequency and its associated aliases; the peaks near 65 Hz are the second harmonic of the subpulse frequency. The second harmonic in Figure 3.17 is more pronounced than in the data (panel (A) of Figure 3.7). In addition to not including noise in the simulation, the discarding of negative values in the displacement polarization mode and the doubling of frequency in the velocity

114
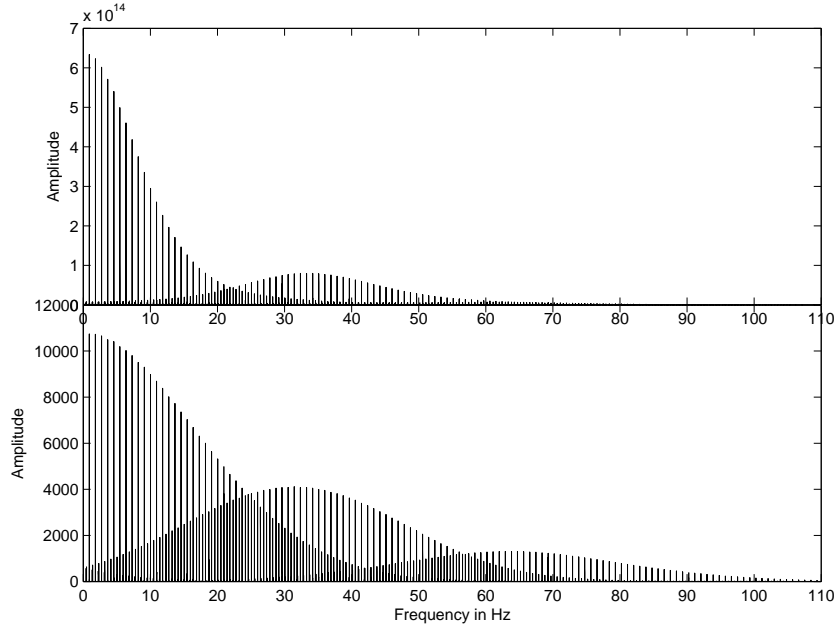
Figure 3.17: Top panel: The Fourier transform of 816 pulses of our simulated data. The peaks centered around 30 Hz are the subpulse frequency and its aliases. The harmonic of the subpulse frequency and its aliases are centered around 65 Hz. The values of the parameters used in our model are listed in Table 3.4.2. Bottom panel: The Fourier transform of 816 pulses from the archival data of PSR 0943+10. This panel is the same as panel A in 3.7.

polarization mode (due to the retention of negative values and the squaring of the function to create the total intensity) results in a second harmonic that is larger in the simulation than in the data.

We reproduce the longitude and harmonic resolved fluctuation spectra used by Deshpande & Rankin (2001) using our model. We use the values of the parameters in Table 3.4.2 to create 256 pulses. We do not add instrument noise to the simulation, as it has little effect in this analysis. The longitude resolved fluctuation spectrum of our model is in the left panel of Figure 3.18 where the subpulse frequency is at about 0.43 Hz and its harmonic is near 0.067 Hz. Likewise, the harmonic resolved fluctuation spectrum of our model is in the right panel of Figure 3.18. The subpulse frequency is located at about 0.48 Hz with a maximum near the 30th harmonic; the harmonic of the subpulse frequency is
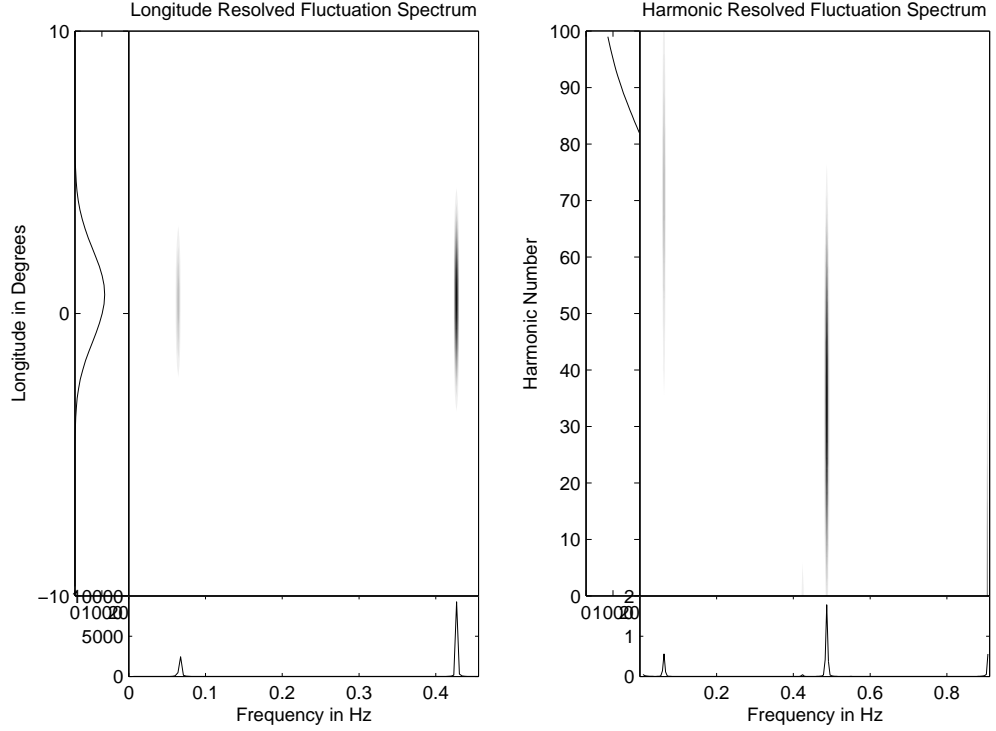
Figure 3.18: Left panel: The longitude resolved fluctuation spectrum of 256 pulses of data produced by our model. Right panel: The harmonic resolved fluctuation spectrum of the same 256 pulses of simulated data. The values of the parameters used in our model are listed in Table 3.4.2.

at 0.63 Hz with a maximum near the 70th harmonic. Just as with the Fourier transform, the more pronounced harmonics of the subpulse frequency in our simulation is due to the discarding of the negative values in the displacement polarization mode and the doubled frequency in the velocity polarization mode. The longitude and harmonic resolved fluctuation spectra created from the model can be compared to the right panels in Figures 3.10 and 3.11, reproduced again here as Figure 3.19.

To compare the average pulse shape, linear polarization, and polarization angle, we created plots similar to those used by Stinebring et al. (1984a,b). Stinebring et al. (1984a,b) created histograms of the linear fractional percent and the polarization angle, along with the average pulse shape, to display pulsar
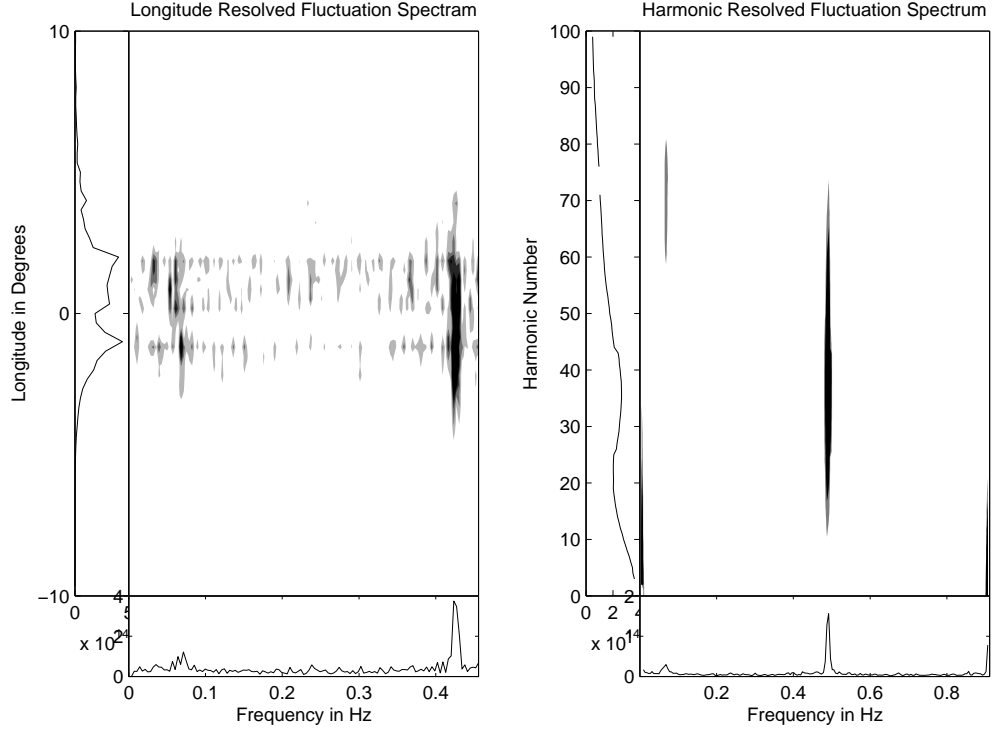
Figure 3.19: Left panel: The longitude resolved fluctuation spectrum of pulses 385-640 from the archival data of PSR 0943+10. This panel is the same as the right panel in Figure 3.10. Right panel: The harmonic resolved fluctuation spectrum of the same 256 pulses of data. This panel is the same as the right panel in Figure 3.11.

data. We create Stinebring-like plots of both the data and our simulation, where we have included off-pulse noise in our simulation. We have no fractional linear percent other than 0% or 100% due to the large displacement polarization mode compared to the weaker velocity polarization mode. The instances when the velocity polarization mode is larger than the displacement polarization mode occurs when the displacement polarization mode is zero (due to the truncation of negative values), thus still resulting in a fractional linear percent of 100%.
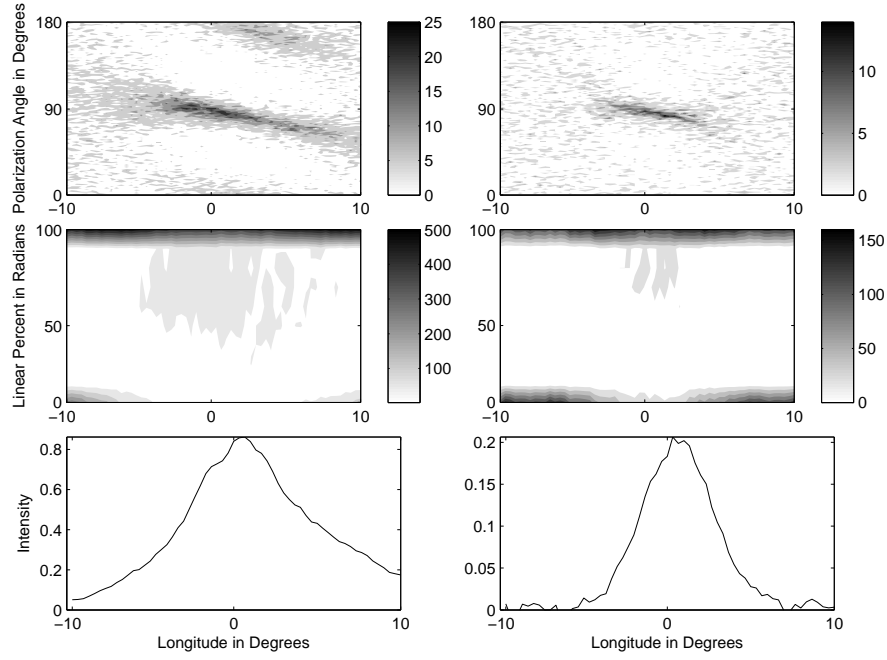
Figure 3.20: Left panel: The properties of PSR 0943+10 using all 816 pulses in the archival data. The top three panels show in histogram form, starting from the top, the circular polarization percent, polarization angle, and linear polarization percent. The average pulse shape is in the bottom panel. Right panel: Our model of the data, using the results of Gaussfit. Noise was adding using the off-pulse noise from the archival data.

3.5   Conclusions

It was our goal to develop a non-radial pulsation model that can reproduce the wide range of observed pulsar behavior. While our original model in §2 was able to model the total intensity of a specific subset of pulsar phenomena, we expanded on the model in this chapter to encompass the polarization properties, omitted in §2, so that we can model a wider range of pulsar morphology. Specifically, two orthogonal polarization modes are present in most pulsars and this was a key feature in the development of our current model. By building a model with two orthogonal polarization modes, we were able to not only mimic the 90° degree polarization angle switches, but we were subsequently able to model other phenomena such as the splitting in the driftband and depolarization.

118

We describe the displacement of the material on the star due to thermal variations as a Legendre polynomial modulated by a sinusoid, and the velocity of the particle motion as the derivative of the displacement. We then assign one polarization mode to the displacement and one polarization mode to the velocity of the material, and by definition, these two modes are orthogonal to each other. From this, we create the Stokes' parameters so that our model directly mimics the observations taken from the telescope.

Using archival data of PSR 0943+10, we conducted an extensive analysis of the data in order to fit our model to the data quantitatively. Driftbands of 100 pulse segments of the data show a longitude-dependent splitting; the subpulses appear to be bifurcated on the right side of the pulse profile but rejoin on the left side of the profile. The subpulse frequency changes throughout the entire data set, indicating that any quantitative fitting may be more effective using smaller portions of the data where the subpulse frequency is stable. The pulse amplitudes vary wildly and the stochastic pulse height variation is intrinsic to the star and not due to instrumental noise.

We use a least-squares approximation to fit the free parameters in our model to the data. We fit 100 pulse sections of the data to minimize the effect of the wandering of the subpulse frequency. Using the average pulse shape, we fit the mean (ϕ_{mean}) and standard deviation (σ) of the Gaussian curve, which acts as our window function. We try to reduce the effect of the stochastic pulse height variation by unitizing the pulse amplitudes to the average pulse shape. We compare the fitted parameters of Gaussfit to the polarization angle histogram, driftband, and Stinebring-like plot of the data. The model successfully reproduces the observed phenomena of PSR 0943+10.

The parameters in our model can be separated into geometrical and pulsational parameters and we find that there is very little connection between these two categories. The geometrical parameters are highly correlated and it is their relationship to each other that is significant rather than their actual values.

While this means that there are many combinations of the geometrical parameters that can match the observations and we may never know their true value, the independence of these parameters from the pulsational ones allows us the possibility to learn new physics from the pulsational parameters, regardless of the geometry of the star.

The value of ψ_{delay}, the phase difference between the two orthogonal polarization modes, is an interesting parameters from which we can learn about the physics of pulsating neutron stars. Positive values of ψ_{delay}, which we have in PSR 0943+10, means that the maximum light arrives before the maximum velocity, consistent with a delay in the flux maximum compared with the adiabatic case (Clemens et al., 2000). This is what we find in white dwarf stars, and expect from thermal oscillations. It is consistent with the identification of the displacement polarization mode as a surface flux phenomena related to pulsations.

The results of the quantitative fitting of PSR 0943+10 demonstrate that a pulsational model can be used to describe the observations and that the resulting pulsational parameters can directly lead to understanding the physics of the star. However, PSR 0943+10 is a fairly simple star with no nodal lines and a single subpulse frequency. Modeling more complex pulsars, pulsars with multiple subpulse frequencies and/or multiple components, will deepen our understanding of the physics of pulsations and the properties of neutron stars.

Chapter 4

A QUALITATIVE COMPARISON OF OUR PULSATIONAL MODEL TO PSR 0809+74

"All men have the stars," he answered,

"but they are not the same things for different people.

For some, who are travelers, the stars are guides.

For others they are no more than little lights in the sky.

For others, who are scholars, they are problems.

For my businessman they were wealth.

But all these stars are silent. You – you alone –

will have the stars as no one else has them –"

Antoine de Saint-Exupéry

The Little Prince

4.1 Introduction

Thus far, our non-radial oscillation model has qualitatively reproduced drifting and quasi-stationary subpulses, subpulse phase jumps of 180°, mode-changes, nulls, and driftband curvature in §2. Using the literature, we found pulsars that had examples of each type of phenomena we were trying to explain and created models to compare to the published results. In §3 we expanded our model to explain the orthogonal polarization modes and quantitatively compared our model to PSR 0943+10. PSR 0943+10 is an ideal star for initially testing of our model because of its simple average pulse shape and single subpulse frequency.

After demonstrating that our non-radial oscillation model can reproduce the behavior of PSR 0943+10, we decided that further tests of our model were in order, and to do so, we needed to observe other pulsars. In this chapter, we describe our observations using the Green Bank Telescope and, for PSR 0809+74, show our data and a qualitative fit of our model to both our observations and published analyses.

4.2 Observations

We applied for time on the Green Bank telescope and compiled a target list of 16 pulsars, which are listed in Table 4.2 along with their specific interesting observational property. In collaboration with Bryan Jacoby, we acquired 28 hours of single pulse L-Band measurements at 1.4 GHz. We used the Caltech-Green Bank-Swinburne Recorder II (CGSR2) to acquire single pulse data in all four Stokes parameters with a time resolution of approximately 0.5 msec. As a backup, we used the Berkeley-Caltech Pulsar Machine (BCPM) which records single pulse data, intensity only (Stokes I), with a time resolution of 0.576 msec.

Pulsar	Observational Property
0031-07	dual and cyclic periods
0037+56	multiple periods
0320+39	subpulse phase jump of 180 degrees
0329+54	non-orthogonal polarization modes
0525+21	typical double profile, unique circular polarization
0809+74	subpulse phase is not 180 degrees, multiple periods
0826-34	always on, unique phase behavior
0823+26	interpulse, multiple periods
0943+10	further quantitative analysis, multiple periods
1133+16	asymmetric orthogonal polarization modes
1237+25	quasi-stationary drift, multiple components
1737+25	quasi-stationary drift, multiple components
1919+21	fiducial
1929+10	pre- and post- cursor
2016+28	multiple periods
2020+28	fiducial

All of the data shown in the following section were taken using the BCPM; the data from the CGSR2 has not yet been calibrated. The usefulness of the data varies for the different pulsars. Scintillation occurs on a relatively long scale (Hewish et al., 1985; Malofeev et al., 1996) compared to the observational window. For faint pulsars the scintillation can decrease the signal so that the individual pulses cannot be distinguished above the noise, as in the case of our observations of PSR 0943+10. Other pulsars, like PSR 0826-34, have null periods as long as (or greater than) periods of emission. Our observations of PSR 0826-34 occured while the pulsars was in a null and thus we have no useful data on this object. While we have not examined all the data for each of the stars, the following section is an example of our data of PSR 0809+74 and our attempt to

model both the data we acquired using the BCPM and published data.

4.3   PSR 0809+74

PSR 0809+74 has highly unusual behavior, and because of this, it has been observed and analyzed extensively in the literature. Many current models are unable to explain the observations, and therefore it has become a litmus test for our model. At high frequencies, around 4.6 GHz, PSR 0809+74 has a single peak in the average pulse profile. At around 1.4 GHz, a subpulse phase jump develops near the center of the profile but still maintains its single peaked average pulse profile. As the frequency decreases to 380 MHz, the phase jump disappears and the driftband shows uniform drift. At even lower frequencies, 62 MHz and below, the average pulse profile bifurcates into a double pulse profile. We attempt to model these attributes at different frequencies and show how our model evolves with observational frequency. Then we show our intensity data taken with the BCPM and compare its cross correlation with those published by Proszynski & Wolszczan (1986) and discuss how this affects our modeling of this star.

In determining the parameters for our model, we first attempt to match the average pulse shape. The left panel in Figure 4.1 shows how the average pulse shape evolves with frequency. Using geometry determined from the polarization angle swing (Rankin et al., 2006) as a starting point, we attempted to match the average pulse shape at different frequencies. As discussed in §1.6, as the observational frequency decreases, the emitted radiation, while emitted at higher altitudes from the stellar surface, is also emitted closer to the magnetic pole. Therefore, β decreases with a decrease in frequency. Starting with $\alpha = 9°$ and $\beta = -4.8°$ at 1.4 GHz, which is a rough approximation of the values determined by Rankin et al. (2006) for that frequency, we then adjusted β to match the profile at each frequency, with the results shown in the right panel of Figure 4.1.

The parameters we used to match the observations at 1.4 GHz in Figure

124
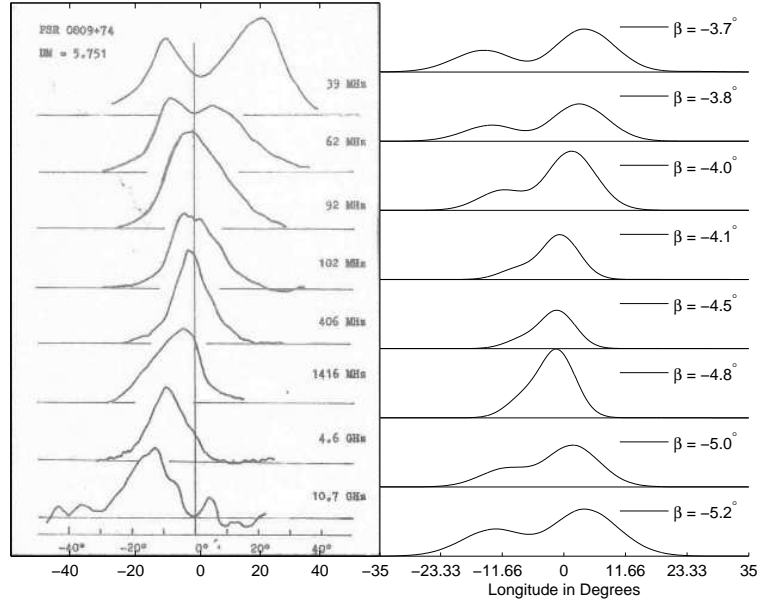
Figure 4.1: Left panel: Average pulse profile of PSR 0809+74 as a function of frequency Rankin et al. (2006). Right panel: Average pulse profiles of our model in which β varies while all other parameters are kept fixed at the values in Table 4.3.

4.1 are listed in Table 4.3. We determined P_1, P_2, and P_3 from the Fourier transform of our BCPM data. We compared our values with published values and found that they were similar. We chose the other values in Table 4.3 based on observations mentioned later in this section. Once we settled on the parameters for the model, we only varied β to get the results in Figure 4.1. We did not modify any of the other parameters in the model; a more accurate match to the observations at different frequencies may be found if we let $a_{0,DPM}$, $a_{0,VPM}$, and $a_{1,DPM}$ vary with frequency.

Parameter	Value
P_1	1.292162269582755 s
P_2	0.03483956830213154 s
P_3	11.24494592753969 s
α	9°
β	−4.5°
ϕ_o	85°
χ_o	−45.84°
l	75
ϕ_{mean}	30°
σ	0.09
$a_{0,DPM}$	0.51
$a_{0,VPM}$	0.12
$a_{1,DPM}$	2.5
ψ_0	-2
ψ_{delay}	-1.9

We have available published average pulse profiles and polarization angle histograms at two frequencies, 112 MHz and 328 MHz, and driftbands are available at a third frequency, 1380 MHz. At 112 MHz, we compared the average pulse profile in Rankin et al. (2005) to that of our model. The left panel in Figure 4.2 shows the published average and linear pulse profile along with the polarization angle histogram (Rankin et al., 2005). The right panel in Figure 4.2 is the same plot using the parameters in Table 4.3 with the exception of $\beta= -4.1°$ to compensate for the lower frequency observations. Most notable is the asymmetry in the polarization angle histogram, which our model reproduces due to the difference in the longitude dependent nodal structure of the two orthogonal polarization modes.

The average pulse profile of PSR 0809+74 is shown in the left panel of Figure
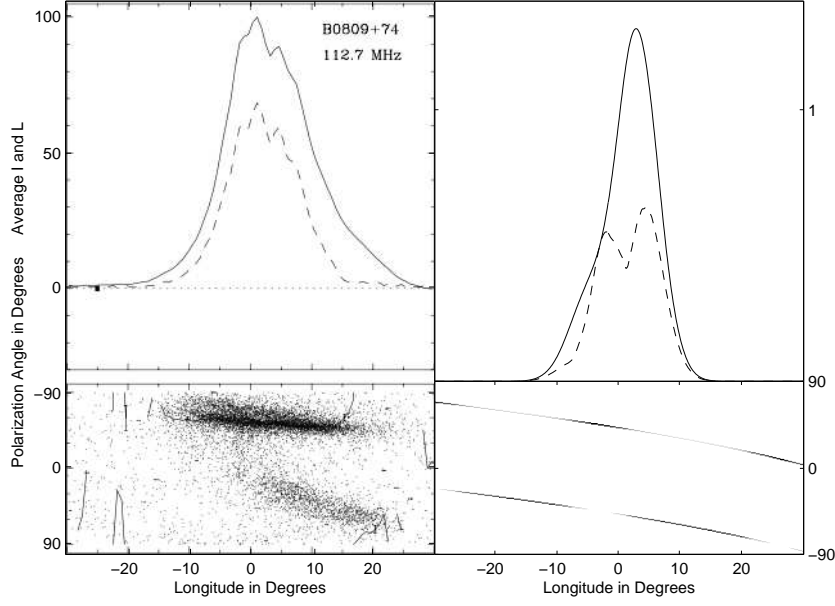
Figure 4.2: Left panel: Average total intensity (solid line), average linear intensity (dashed line), and polarization angle histogram (bottom) of PSR 0809+74 at 112.7 MHz (Rankin et al., 2005). Right panel: Model of PSR 0809+74 of the average total intensity (solid line), average linear intensity (dashed line), and polarization angle histogram (bottom). All parameters are those in Table 4.3, except $\beta = -4.1°$, as is consistent with Figure 4.1.

4.3 at 328 MHz (Rankin et al., 2006). Our model uses the parameters in Table 4.3 and the results are in the right panel of Figure 4.3. Based on the double profile shape in the linear average profile in the data and the dominance of the displacement polarization mode in our simulation, it appears that our velocity polarization mode in the model at this frequency is too small. Allowing the amplitudes in the two polarization modes in our model to vary would improve the qualitative fit.

At 1380 MHz, the published driftband is in Q' space (Rankin et al., 2005), shown in the left panel of Figure 4.4. Near the center of the profile, there is a clear change from Q to $-Q$ in the polarization angle, indicating in our pulsational model, the presence of a nodal line. The nodal line indicates a zero (or nearly zero) intensity of the displacement polarization mode. The average pulse profile
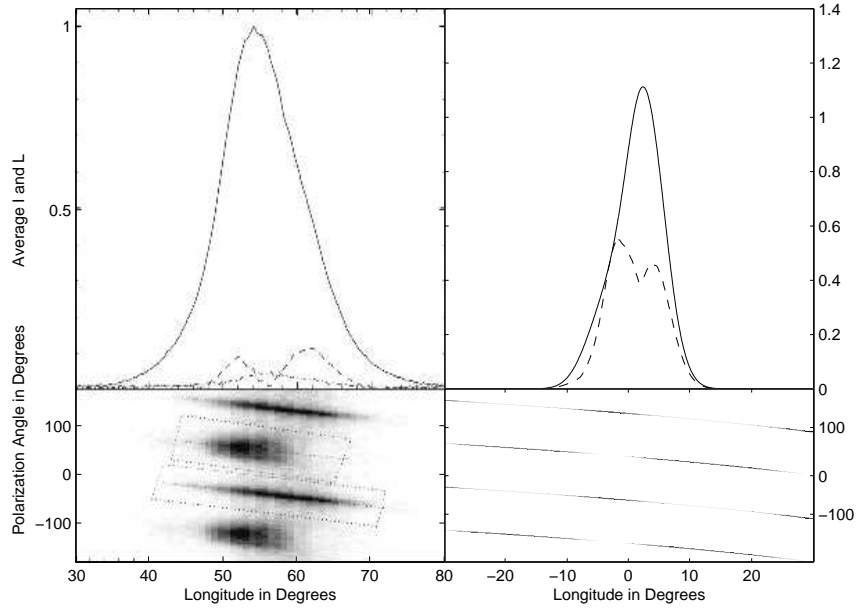
Figure 4.3: Left panel: Average total intensity (solid line), average linear intensity (dashed), and average circular intensity (dashed-dotted) of PSR 0809+74 at 328 MHz. The polarization angle histogram is plotted twice in the bottom portion of the panel (Rankin et al., 2006). Right panel: Model of PSR 0809+74 of the average total intensity (solid line) and average linear intensity (dashed line). The polarization angle histogram is plotted twice in the bottom of the panel. All parameters are those in Table 4.3, to match the frequencies in Figure 4.1.

at this frequency is a single peak with a maximum at the same longitude as the switch from Q to $-Q$. Therefore, the model must be dominated by the velocity polarization mode since the velocity polarization mode has maximum at nodal lines. Keeping all the parameters the same as in Table 4.3 except for $\beta = -4.8°$, we model the driftband, also in Q' space, in the right panel of Figure 4.4. We are able to model the change from Q to Q'. However, our driftbands are narrow compared to the data. This feature can be changed by adjusting $a_{0,DPM}$ and the shape of the window function.

In addition, we acquired over 5000 pulses of PSR 0809+74 using the BCPM. The pulse amplitude distribution is shown in Figure 4.5. At this time, we are unable to produce the driftband in Q' space from our BCPM data as it requires us to have data in all four Stokes parameters. We postpone this analysis until
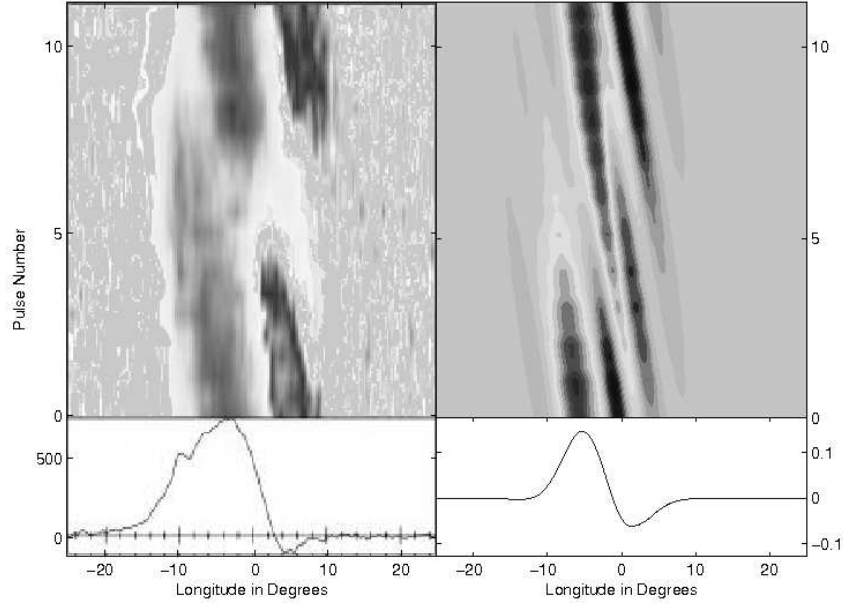
Figure 4.4: Left panel: Driftband of Q' of PSR 0809+74 at 1.38 GHz (Rankin et al., 2005). The data is folded at $P_3 = 11P_1$. The bottom portion of the left panel shows the intensity at each longitude integrated over the driftband. Right panel: Driftband of Q' created by our model using the parameters in Table 4.3, except $\beta = -4.8°$ to match the average profile in Figure 4.1. The simulated data is folded at $P_3 = 11.245$ seconds, where P_3 is calculated from P_2. We used the Fourier transform of our data collected using the BCPM to determine the subpulse period as $P_2 = 34.8395$ msec.

the CGSR2 data is calibrated. However, we show in Figure 4.6 the first 200 pulses of the BCPM data, with the background intensity removed so that the mean intensity for each pulse is zero.

We can compute, however, the cross correlation of PSR 0809+74, as this requires only the intensity data. The cross correlation at 1.42 GHz was published by Proszynski & Wolszczan (1986) and is shown in the left panel of Figure 4.7. We remove the background intensity from the BCPM data and then calculate the cross correlation. The results are in the right panel of Figure 4.7.

We conclude that in the context of our model, that the behavior of PSR 0809+74 is dominated by the velocity polarization mode. We reached this conclusion mainly based on the data around 1.4 GHz, namely the change from Q to
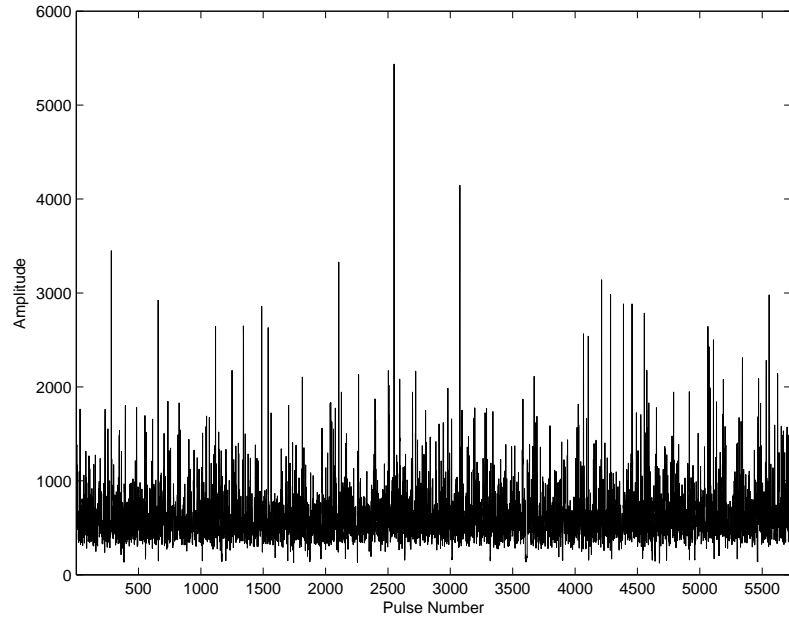
Figure 4.5: Distribution of pulse amplitudes in PSR 0809+74. The data were acquired using the Berkeley-Caltech Pulsar Machine at 1.4 GHz.
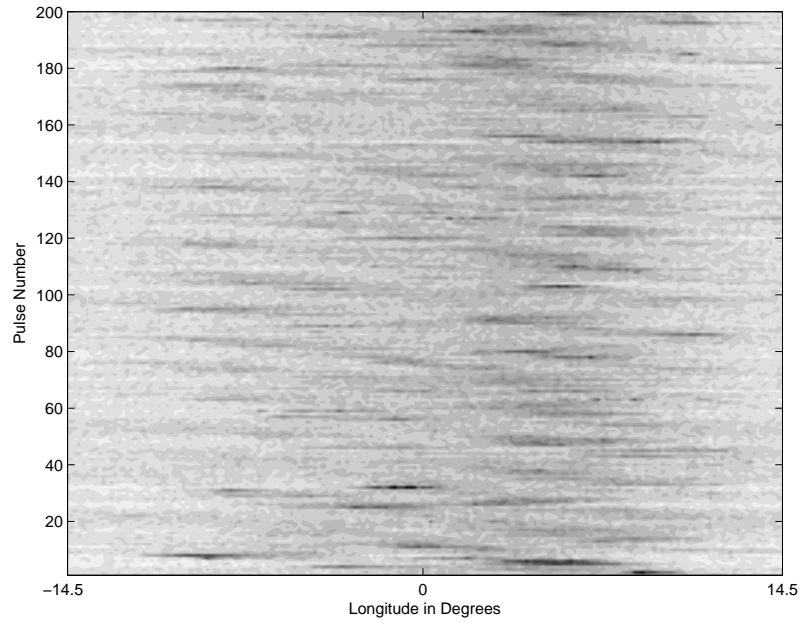
Figure 4.6: The first 200 pulses of PSR 0809+74 acquired using the Berkeley-Caltech Pulsar Machine at 1.4 GHz.
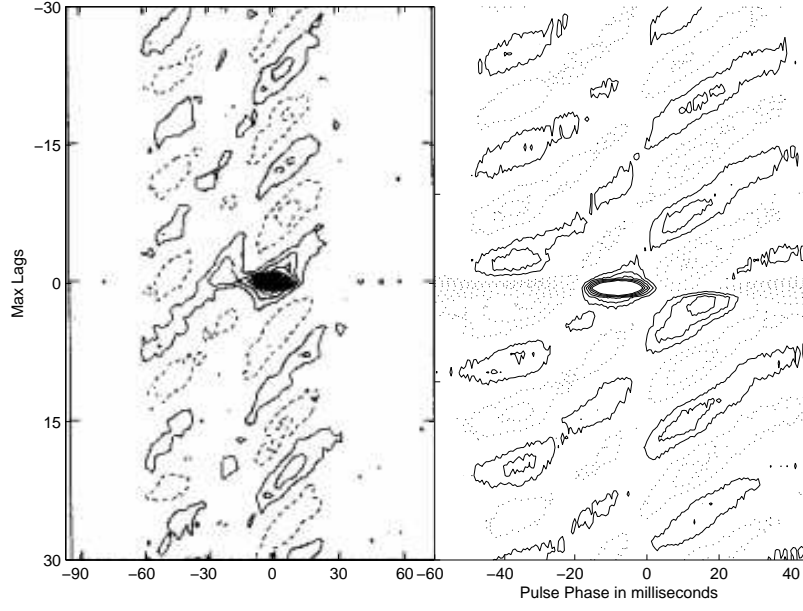
Figure 4.7: Left panel: Cross correlation of PSR 0809+74 at 1.420 GHz Proszynski & Wolszczan (1986). Right panel: Cross correlation of all 5733 pulses taken by the BCPM at 1.4 GHz. Solid contours indicate positive correlations; dashed contours indicate negative correlations.

$-Q$ which corresponds to a maximum in the average pulse profile. The change in polarization angle must be the result of a nodal line, and only the velocity polarization mode has a maximum at a node. We are able to show that, leaving all the parameters in our model fixed except the impact parameter β, we can qualitatively reproduce the change in the average pulse profile with frequency. While our model reproduces the average pulse shape and phase change near 1.4 GHz fairly well, our model is less successful at other frequencies. To improve the results of our model, we could allow the amplitudes of the two polarization modes to vary freely with frequency. Furthermore, since the crux of our assumptions of the free parameters in our model rests on the published change in Q' space, it is crucial to conduct our own analysis of the polarization at this frequency. We would like to determine if the phase change in our data agrees with the published results and that the phase change persists over time. Analysis of our CGSR2 data will clarify these assumptions and guide our intuition in modeling this pulsar.

4.4 Conclusions

For our non-radial oscillation model to be successful, it must be able to reproduce not only the behavior of PSR 0943+10, but the behavior of other pulsars as well. The best way for us to test our model is to acquire data and to conduct our own analysis. To meet this end, we observed 16 pulsars with high time resolution (0.5 msec) for a total of 28 hours using the Green Bank Telescope. We used the Caltech-Green Bank-Swinburne Recorder II to record the data in all four Stokes' parameters and used the Berkeley-Caltech Pulsar Machine as a backup, only recording the total intensity data. While the CGSR2 data is not completely calibrated, we have been able to do some preliminary analysis using methods that only require the total intensity of the BCPM data.

Using the data from the BCPM and published results, we have been able to qualitatively model PSR 0809+74. We attempted to model this star at multiple frequencies. In the spirit of simplicity, we kept all parameters in our model constant except β, which is known to vary with observational frequency. The bulk of our modeling effort centered around observations at 1.4 GHz, where PSR 0809+74 exhibits a phase change and thus is the most difficult of the frequencies to model. We are able to successfully reproduce the behavior of the pulsar at this frequency. Fortunately, our data collected using the CGSR2 and BCPM is also at 1.4 GHz, which allows us to conduct our own analysis of the phase change. However, our model is not as successful at reproducing the behavior of PSR 0809+74 at other frequencies. Models at other frequencies could be drastically improved by allowing several of the other parameters to vary with frequency.

We hoped to find simultaneous multiple subpulse frequencies in some pulsars, as this is the first step in astroseismology. We found several pulsars (0031-07, 0525+21, 0809+74, 0823+26, and 1237+25) with multiple frequencies in their Fourier transform. However, it is unclear at this point whether the frequencies are simultaneous or rather a single subpulse frequency that changes over time.

Our current methodologies need to be developed to make this distinction. The presence of phase changes in a pulsar is an indication, in our model, of a nodal line. The phase changes are one of the fiducial marks in our model; it is around these that all the other parameters are fit. Until we finish calibrating the CGSR2 data, we cannot detect the presence of phase changes. Our next immediate goal is to finish the calibration in conjunction with Bryan Jacoby so that we may analyze the data in polarization space and begin quantitative fits of our model.

Chapter 5

CONCLUSION

"In one of the stars I shall be living.
In one of them I shall be laughing.
And so it will be as if all the stars were laughing,
when you look at the sky at night...
You – only you – will have stars that can laugh!"
Antoine de Saint-Exupéry
The Little Prince

5.1 Conclusion

The purpose of this project was to determine if a non-radial pulsation model could explain drifting subpulses in radio pulsars. Our initial non-radial oscillation model successfully described pulsar phenomena in a qualitative fashion. However, this model only described a certain subset of pulsars with drifting subpulses and did not attempt to explain any of the distinct polarization properties in pulsars. We then expanded on the model to include polarization and, in doing so, were able to model a wider variety of pulsars. As quantitative fit of our model to archival data PSR 0943+10 showed that the new model can reproduce all of the observed behavior in this star.

Initially, we introduced a model for pulsars in which non-radial oscillations of

high spherical degree (ℓ) are aligned to the magnetic axis of a spinning neutron star. The rotation of the pulsar carries a pattern of pulsation nodes underneath our sightline, reproducing the longitude stationary structure seen in average pulse profiles. The associated time-like oscillations reproduce the drifting subpulses. The presence of nodal lines can account for observed 180° phase jumps in drifting subpulses and their otherwise poor phase stability, even if the time-like oscillations are strictly periodic. Our model also accounted for the mode changes and nulls observed in some pulsars as quasiperiodic changes between pulsation modes of different (ℓ) or radial overtone (n), analogous to pulsation mode changes observed in oscillating white dwarf stars. We discussed other definitive and testable requirements of our model and showed that they are qualitatively supported by existing data. We speculated about the excitation mechanisms of the non-radial pulsations, the physics we can learn from them, and their relationship to the period evolution of pulsars.

We elaborated our model to account for the diverse polarization behavior observed in pulsars. The measured polarization angle for most pulsars reveals the existence orthogonal polarization modes. We concluded that our initial model represented one polarization mode: the displacement of stellar material due to thermal variations, which can be described by non-radial oscillations of degree ℓ modulated by a time-like sinusoidal oscillations. The second polarization mode represents the pulsational velocities. The time lag between the displacement and the velocity of particle motion was accounted for by the addition of a ψ_{delay} phase term in the temporal variations of the displacement polarization mode. In retrospect, our original model was only able to reproduce pulsars that were dominated by what we now recognize as the displacement polarization mode; the new model can reproduce a broader spectrum of pulsar morphology. The combination of these two polarization modes can be transformed into the Stokes' parameters, which can then be quantitatively compared to observational data.

135

PSR 0943+10 is an ideal candidate for comparing our model to the data because of its simple average pulse shape and its single subpulse frequency. Before comparing our model to archival data of PSR 0943+10, we conducted an extensive analysis of the data. The data are plagued with a large stochastic pulse amplitude distribution which is intrinsic to the star and not due to instrumental noise. The driftbands of 100 pulse segments of the data show a longitude-dependent splitting of the subpulses. The subpulses appear to bifurcate on the right side but remain single peaked on the left side of the profile. The subpulse frequency wanders throughout all 816 pulses in this data set. While we concur with Deshpande & Rankin (2001) that there is an amplitude modulation in pulses 129-384, the modulation is not significant in the face of stochastic variations nor seen in other sections of the data and therefore we do not include the amplitude modulation in our model at this time.

We use Gaussfit, as robust least-squares approximation package, to quantitatively fit our model to the archival data of PSR 0943+10 and conclude that our non-radial oscillation model can reproduce the observed pulsar behavior. We find that the parameters can be divided into two categories: geometrical and pulsational parameters. The geometrical parameters are highly correlated and it is their relationship to each other that is significant in matching the observations, not the true value of the parameters. Therefore, we are prevented us from determining the true geometry of the star. Fortunately, for the most part, the geometrical parameters are independent from the pulsational parameters and thus the degeneracy of the geometry does not prevent us from learning about the physics of pulsations of neutron stars. We find that the phase difference between the two orthogonal polarization modes, ψ_{delay}, is in the correct quadrant for self-exciting pulsations. The simple average pulse profile and single frequency of PSR 0943+10 limits the amount of physics we can learn, and quantitative analyses of more complex pulsars will deepen our understanding about the pulsations of neutron stars.

To this end, we acquired 28 hours of high time resolution data in all four Stokes' parameters of 16 pulsars using the 100 meter telescope in Green Bank, West Virginia. While the data is not fully calibrated at this time, we did preliminary data analysis and modeling of PSR 0809+74. We chose this star because its unusual properties have been well documented in the literature. We found that we could model the change in average pulse profile with frequency by keeping all the parameters in our non-radial oscillation model constant, except for the impact parameter, β. We then successfully modeled the average total and linear intensity and polarization angle a several frequencies. At 1380 MHz, PSR 0809+74 shows a unique change from Q to $-Q$ in Q' space and the current rotating spark model has a difficult time explaining this phenomena. This change is a natural part of our pulsation model and we are able to qualitatively model it. We save a more quantitative fit of PSR 0809+74 for future work.

5.2   Scientific Impact

The competing theory to explain the drifting subpulses in pulsars is the drifting spark gap model. The spark gap model assumes a vacuum gap above the stellar surface. To prevent the gap from growing indefinitely, a discharge or "spark" occurs which then translates through a variety of mechanisms, to stellar emission. The sparks form an evenly spaced rotating ring around the magnetic pole which then produces the subpulses that drift through the pulse window. This model is ever growing; new parameters and explanations are added for each new complexity observed in a pulsar. There is little scientific value to be gained in regards to stellar properties from this model as it is unrelated to any global phenomena; the sparks are limited to the magnetic pole. And as a theory, many of its predictions are not satisfied.

Non-radial oscillations were originally dismissed as an explanation for drifting subpulses because the observed subpulse frequency appeared to be unstable. We

have shown that this is an unwarranted conclusion; the subpulse frequency can appear to vary even though there is an underlying stable clock. Our model can reproduce a wide range of observed behavior without increasing the number of free parameters and makes specific predictions. Most importantly, non-radial oscillations are a global phenomena and further exploration of this model in comparison to more complex pulsars can lay the foundation for astroseismology and other work on stellar composition and interiors.

5.3   Future Work

Our non-radial oscillation model and its comparison to PSR 0943+10 are by no means the end of this work. Indeed, there are many avenues to explore and unique pulsars to model. Our model is incomplete as it does not include circular polarization. While we have proposed explanations for mode changes and nulls, we have not quantified or tried to model pulsars that show this type of behavior. It would be interesting to know if mode changes and nulls are predictable and how they relate in terms of our model. We have only quantitatively compared our model to a fairly simple pulsar; further comparisons of our model to more complicated stars are necessary. No pulsars have yet been shown to have simultaneous multiple frequencies, needed for astroseismology, and the method for detecting multiple simultaneous periodicites has yet to be developed. It is our hope that the non-radial oscillation model that we have proposed will, instead of closing an unsolved case, will open the door to new understandings of pulsars, stellar interiors, and physics yet to be discovered.

Appendix A

APPENDIX

A.1 Modulation Induced Driftband Curvature

The purpose of this appendix is to calculate, in approximate fashion, the apparent change in subpulse drift between nodal lines caused by the amplitude modulation of strictly periodic time-like pulses. We will approximate the longitude-dependent modulation between two nodes as a cosine function, which is very similar to the envelope between two nodes of a spherical harmonic for sightlines with $\beta = 0$. Thus we can write a more manageable version of Equation 2.1:

$$\xi = \cos(\omega_\Phi t) \cos(\omega_t t + \phi), \tag{A.1}$$

where $\omega_\Phi = \frac{2\pi}{P_{node}}$.

To find the times of maxima (and minima), we take the derivative and set it to zero, yielding:

$$-\frac{\omega_\Phi}{\omega_t + \phi} = \frac{\tan(\omega_t t + \phi)}{\tan(\omega_\Phi t)}. \tag{A.2}$$

In Figure A.1 we have plotted the locus of the times-of-maxima for $\omega_\Phi t$ between -90 and 90 degrees, simulating the range between nodal lines, for a variety of cases. The lines in these plots are analogous to subpulse driftbands, because they show how the maxima (and minima) of time-like pulses vary with longitude.

For the case where $P_{time} \approx P_{node}$, we expect no driftband curvature. When $P_{time} < P_{node}$, we expect slower drift near nodal lines (right hand panels), and vice versa.

We note that for $\beta \neq 0$ sightlines that graze along a nodal line in the center of the pulse window, the driftband curvature can be the reverse of the cases plotted here, i.e. narrow subpulses will drift more slowly near the center of the profile. This can explain the driftband curvature measured for PSR0031-07 by Krishnamohan (1980), and discussed by Wright (1981). The more important conclusion is that when nodal lines are present, P_2 can vary with longitude, even though the underlying clock is absolutely stable.
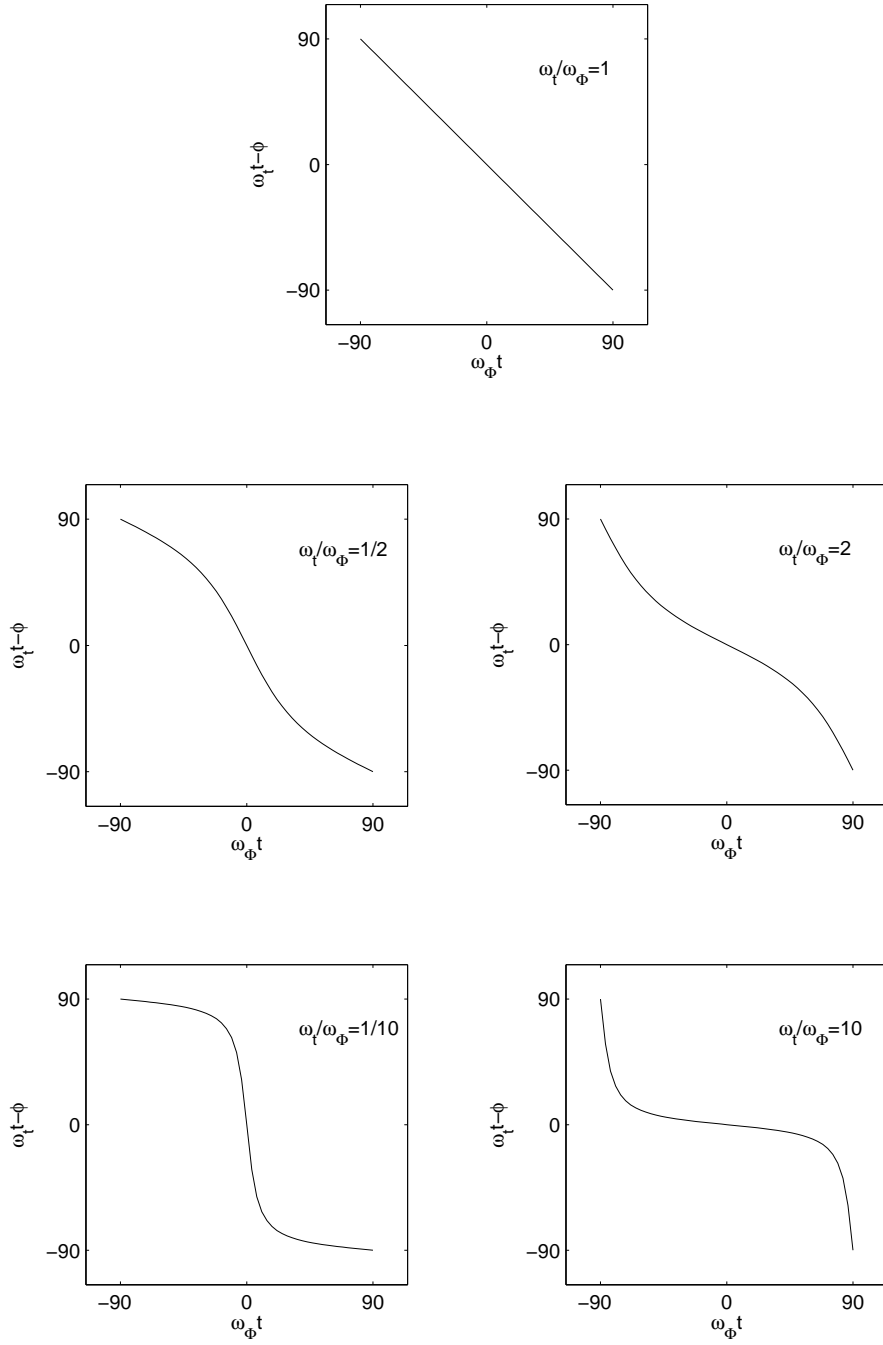
Figure A.1: Simulated driftband curvature calculated from Equation A.2 for cases where $P_{time} = P_{node}$ (top), $P_{time} > P_{node}$ (left) and $P_{time} < P_{node}$ (right).

REFERENCES

Agrinier, B., Masnou, J. L., Parlier, B., Niel, M., Mandrou, P., Vedrenne, G., Gerardi, G., Mineo, T., Sacco, B., Scarsi, L., Costa, E., Massaro, E., Matt, G., Salvati, M., & Lyne, A. G. 1990, Astrophysical Journal, 355, 645

Ambartsumyan, V. A., & Saakyan, G. S. 1960, Soviet Astronomy, 4, 187

Asgekar, A., & Deshpande, A. A. 2001, Monthly Notices of the RAS, 326, 1249

Baade, W., & Zwicky, F. 1934, Proceedings of the National Academy of Science, 20, 259

Backer, D. C. 1970a, Nature, 227, 692

—. 1970b, Nature, 228, 1297

—. 1970c, Nature, 228, 42

—. 1973, Astrophysical Journal, 182, 245

—. 1976, Astrophysical Journal, 209, 895

Backer, D. C., Rankin, J. M., & Campbell, D. B. 1976, Nature, 263, 202

Bartel, N., Morris, D., Sieber, W., & Hankins, T. H. 1982, Astrophysical Journal, 258, 776

Biggs, J. D. 1990, Monthly Notices of the RAS, 246, 341

Biggs, J. D., McCulloch, P. M., Hamilton, P. A., Manchester, R. N., & Lyne, A. G. 1985, Monthly Notices of the RAS, 215, 281

Boriakoff, V. 1976, Astrophysical Journal, Letters, 208, L43

Cameron, A. G. 1959, Astrophysical Journal, 130, 884

Carroll, B. W., Zweibel, E. G., Hansen, C. J., McDermott, P. N., Savedoff, M. P., Thomas, J. H., & van Horn, H. M. 1986, Astrophysical Journal, 305, 767

Cheng, A., Ruderman, M., & Sutherland, P. 1976, Astrophysical Journal, 203, 209

Christensen-Dalsgaard, J. 2003, Lecture Notes on Stellar Oscillations

Clemens, J. C., & Rosen, R. 2004, Astrophysical Journal, 609, 340

Clemens, J. C., van Kerkwijk, M. H., & Wu, Y. 2000, Monthly Notices of the RAS, 314, 220

Clemens, S. L. 1883, Life on the Mississippi

Cocke, W. J., Disney, M. J., & Taylor, D. J. 1969, Nature, 221, 525

Cordes, J. M. 1978, Astrophysical Journal, 222, 1006

Cordes, J. M., & Hankins, T. H. 1977, Astrophysical Journal, 218, 484

Daugherty, J. K., & Harding, A. K. 1996, Astrophysical Journal, 458, 278

Deshpande, A. A., & Rankin, J. M. 2001, Monthly Notices of the RAS, 322, 438

Drake, F. D., & Craft, H. D. 1968, Nature, 220, 231

Duncan, R. C. 1998, Astrophysical Journal, Letters, 498, L45+

Dziembowski, W. 1977, Acta Astronomica, 27, 203

—. 1982, Acta Astronomica, 32, 147

Edwards, R. T. 2004, Astronomy and Astrophysics, 426, 677

—. 2006, Chinese Journal of Astronomy and Astrophysics Supplement, 6, 18

Edwards, R. T., & Stappers, B. W. 2002, Astronomy and Astrophysics, 393, 733

—. 2003, Astronomy and Astrophysics, 410, 961

Edwards, R. T., Stappers, B. W., & van Leeuwen, A. G. J. 2003, Astronomy and Astrophysics, 402, 321

Esamdin, A., Lyne, A. G., Graham-Smith, F., Kramer, M., Manchester, R. N., & Wu, X. 2005, Monthly Notices of the RAS, 356, 59

Finn, L. S. 1990, Monthly Notices of the RAS, 245, 82

Fowler, L. A., Morris, D., & Wright, G. A. E. 1981, Astronomy and Astrophysics, 93, 54

Fowler, R. H. 1926, Monthly Notices of the RAS, 87, 114

Fung, P. K., & Kuijpers, J. 2004, Astronomy and Astrophysics, 422, 817

Gangadhara, R. T., & Gupta, Y. 2001, Astrophysical Journal, 555, 31

Gil, J. 1983, Astronomy and Astrophysics, 123, 7

Gil, J., Gupta, Y., Gothoskar, P. B., & Kijak, J. 2002, Astrophysical Journal, 565, 500

Gil, J., & Kijak, J. 1992, Astronomy and Astrophysics, 256, 477

Gil, J. A. 1991, Astronomy and Astrophysics, 243, 219

Gil, J. A., Kijak, J., & Seiradakis, J. H. 1993, Astronomy and Astrophysics, 272, 268

Gil, J. A., Lyne, A. G., Rankin, J. M., Snakowski, J. K., & Stinebring, D. R. 1992, Astronomy and Astrophysics, 255, 181

Ginzburg, V. L., & Zhelezniakov, V. V. 1975, Annual Review of Astron and Astrophys, 13, 511

Gogoberidze, G., Machabeli, G. Z., Melrose, D. B., & Luo, Q. 2005, Monthly Notices of the RAS, 360, 669

Gold, T. 1968, Nature, 218, 731

—. 1969, Nature, 221, 25

Goldreich, P., & Julian, W. H. 1969, Astrophysical Journal, 157, 869

Gould, D. M. 1994, PhD thesis, , Univ. of Manchester, (1994)

Graham-Smith, F. 2003, Reports of Progress in Physics, 66, 173

Gunn, J. E., & Ostriker, J. P. 1969, Nature, 221, 454

—. 1971, Astrophysical Journal, 165, 523

Gupta, Y., & Gangadhara, R. T. 2003, Astrophysical Journal, 584, 418

Hamada, T., & Salpeter, E. E. 1961, Astrophysical Journal, 134, 683

Han, J. L., & Manchester, R. N. 2001, Monthly Notices of the RAS, 320, L35

Hankins, T. H., & Wolszan, A. 1987, Astrophysical Journal, 318, 410

Hankins, T. H., & Wright, G. A. E. 1980, Nature, 288, 681

Hansen, C. J., & Cioffi, D. F. 1980, Astrophysical Journal, 238, 740

Hansen, C. J., & Kawaler, S. D. 1994, Stellar interiors : physical principles, structure, and evolution (New York : Springer-Verlag, 1994. 1st ed.)

Harrison, B. K., Thorne, K. S., Wakano, M., & Wheeler, J. A. 1965, Gravitation Theory and Gravitational Collapse (Gravitation Theory and Gravitational Collapse, Chicago: University of Chicago Press, 1965)

Harrison, B. K., Wakano, M., & Wheeler, J. A. 1958, in La Structure et l'évolution de l'univers, ed. R. Stoops, (Onziéme Conseil de Physique Solay, Brussels, Belgium), 124

Hewish, A. 1970, Annual Review of Astron and Astrophys, 8, 265

Hewish, A., Bell, S. J., Pilkington, J. D., Scott, P. F., & Collins, R. A. 1968, Nature, 217, 709

Hewish, A., Wolszczan, A., & Graham, D. A. 1985, Monthly Notices of the RAS, 213, 167

Hibschman, J. A., & Arons, J. 2001, Astrophysical Journal, 546, 382

Hoyle, F., Narlikar, J. V., & Wheeler, J. A. 1964, Nature, 203, 914

Izvekova, V. A., Kuzmin, A. D., Lyne, A. G., Shitov, Y. P., & Smith, F. G. 1993, Monthly Notices of the RAS, 261, 865

Jessner, A., Lesch, H., & Kunzl, T. 2001, Astrophysical Journal, 547, 959

Johnston, S., Hobbs, G., Vigeland, S., Kramer, M., Weisberg, J. M., & Lyne, A. G. 2005, Monthly Notices of the RAS, 364, 1397

Joss, P. C., & Rappaport, S. A. 1976, Nature, 264, 219

Kleinman, S. J., Nather, R. E., Winget, D. E., Clemens, J. C., Bradley, P. A., Kanaan, A., Provencal, J. L., Claver, C. F., Watson, T. K., Yanagida, K., Nitta, A., Dixson, J. S., Wood, M. A., Grauer, A. D., Hine, B. P., Fontaine, G., Liebert, J., Sullivan, D. J., Wickramasinghe, D. T., Achilleos, N., Marar, T. M. K., Seetha, S., Ashoka, B. N., Meistas, E., Leibowitz, E. M., Moskalik,

P., Krzesinski, J., Solheim, J.-E., Bruvold, A., O'Donoghue, D., Kurtz, D. W., Warner, B., Martinez, P., Vauclair, G., Dolez, N., Chevreton, M., Barstow, M. A., Kepler, S. O., Giovannini, O., Augusteijn, T., Hansen, C. J., & Kawaler, S. D. 1998, Astrophysical Journal, 495, 424

Komesaroff, M. M. 1970, Nature, 225, 612

Komesaroff, M. M., Morris, D., & Cooke, D. J. 1970, Astrophysics Letters and Communications, 5, 37

Kramer, M., Wielebinski, R., Jessner, A., Gil, J. A., & Seiradakis, J. H. 1994, Astronomy and Astrophysics, Supplement, 107, 515

Krishnamohan, S. 1980, Monthly Notices of the RAS, 191, 237

Kurtz, D. W. 1982, Monthly Notices of the RAS, 200, 807

Kurtz, D. W., Shibahashi, H., & Goode, P. R. 1990, Monthly Notices of the RAS, 247, 558

Large, M. I., Vaughan, A. E., & Mills, B. Y. 1968, Nature, 220, 340

Lesch, H., Jessner, A., Kramer, M., & Kunzl, T. 1998, Astronomy and Astrophysics, 332, L21

Lyne, A. G., & Ashworth, M. 1983, Monthly Notices of the RAS, 204, 519

Lyne, A. G., & Manchester, R. N. 1988, Monthly Notices of the RAS, 234, 477

Lyne, A. G., Smith, F. G., & Graham, D. A. 1971, Monthly Notices of the RAS, 153, 337

Lyutikov, M., Blandford, R. D., & Machabeli, G. 1999a, Monthly Notices of the RAS, 305, 338

Lyutikov, M., Machabeli, G., & Blandford, R. 1999b, Astrophysical Journal, 512, 804

Malofeev, V. M., Shishov, V. I., Sieber, W., Jessner, A., Kramer, M., & Wielebinski, R. 1996, Astronomy and Astrophysics, 308, 180

Manchester, R. N. 1995, Journal of Astrophysics and Astronomy, 16, 107

Manchester, R. N., Lyne, A. G., Taylor, J. H., Durdin, J. M., Large, M. I., & Little, A. G. 1978, Monthly Notices of the RAS, 185, 409

Manchester, R. N., & Taylor, J. H. 1977, Pulsars (San Francisco : W. H. Freeman, c1977.), 36–+

Manchester, R. N., Taylor, J. H., & Huguenin, G. R. 1975, Astrophysical Journal, 196, 83

McCulloch, P. M., Hamilton, P. A., Ables, J. G., & Hunt, A. J. 1983, Nature, 303, 307

McDermott, P. N., van Horn, H. M., & Hansen, C. J. 1988, Astrophysical Journal, 325, 725

Melikidze, G. I., Gil, J. A., & Pataraya, A. D. 2000, Astrophysical Journal, 544, 1081

Melrose, D. B. 1978, Astrophysical Journal, 225, 557

—. 1991, Annual Review of Astron and Astrophys, 29, 31

—. 1995, Journal of Astrophysics and Astronomy, 16, 137

Mestel, L. 1971, Nature, 233, 149

Michel, F. C. 1991, Theory of neutron star magnetospheres (Chicago, IL, University of Chicago Press, 1991, 533 p.)

Mitra, D., & Deshpande, A. A. 1999, Astronomy and Astrophysics, 346, 906

Mitra, D., & Rankin, J. M. 2002, Astrophysical Journal, 577, 322

148

Nather, R. E., Winget, D. E., Clemens, J. C., Hansen, C. J., & Hine, B. P. 1990, Astrophysical Journal, 361, 309

Oppenheimer, J. R., & Volkoff, G. M. 1939, Phys. Rev., 55, 374

Oster, L., & Sieber, W. 1977, Astronomy and Astrophysics, 58, 303

Ostriker, J. P., & Gunn, J. E. 1969, Astrophysical Journal, 157, 1395

Pacini, F. 1967, Nature, 216, 567

—. 1968, Nature, 219, 145

Pandharipande, V. R., Pines, D., & Smith, R. A. 1976, Astrophysical Journal, 208, 550

Potekhin, A. Y. 1999, Astronomy and Astrophysics, 351, 787

Proszynski, M., & Wolszczan, A. 1986, Astrophysical Journal, 307, 540

Radhakrishnan, V., & Cooke, D. J. 1969, Astrophysics Letters and Communications, 3, 225

Radhakrishnan, V., Cooke, D. J., Komesaroff, M. M., & Morris, D. 1969, Nature, 221, 443

Radhakrishnan, V., & Rankin, J. M. 1990, Astrophysical Journal, 352, 258

Rankin, J. M. 1983a, Astrophysical Journal, 274, 359

—. 1983b, Astrophysical Journal, 274, 333

—. 1986, Astrophysical Journal, 301, 901

—. 1990, Astrophysical Journal, 352, 247

—. 1993a, Astrophysical Journal, 405, 285

—. 1993b, Astrophysical Journal, Supplement, 85, 145

Rankin, J. M., & Ramachandran, R. 2003, Astrophysical Journal, 590, 411

Rankin, J. M., Ramachandran, R., & Suleymanova, S. A. 2005, Astronomy and Astrophysics, 429, 999

—. 2006, Astronomy and Astrophysics, 447, 235

Rankin, J. M., & Wright, G. A. E. 2003, The Astronomy and Astrophysics Review, 12, 43

Reisenegger, A., & Goldreich, P. 1992, Astrophysical Journal, 395, 240

Richards, D. W., & Comella, J. M. 1969, Nature, 222, 551

Richardson, M. B., van Horn, H. M., Ratcliff, K. F., & Malone, R. C. 1982, Astrophysical Journal, 255, 624

Rickett, B. J. 1975, Astrophysical Journal, 197, 185

Robinson, E. L., Kepler, S. O., & Nather, R. E. 1982, Astrophysical Journal, 259, 219

Romani, R. W. 1996, Astrophysical Journal, 470, 469

Ruderman, M. A. 1968, Nature, 218, 1128

Ruderman, M. A., & Sutherland, P. G. 1975, Astrophysical Journal, 196, 51

Rylov, I. A. 1978, Astrophysics and Space Science, 53, 377

Salter, M. J., Lyne, A. G., & Anderson, B. 1979, Nature, 280, 477

Schopper, R., Ruhl, H., Kunzl, T. A., & Lesch, H. 2002, in Neutron Stars, Pulsars, and Supernova Remnants, ed. W. Becker, H. Lesch, & J. Trümper, 193–+

Shapiro, S. L., & Teukolsky, S. A. 1983, Black holes, white dwarfs, and neutron stars: The physics of compact objects (Research supported by the National Science Foundation. New York, Wiley-Interscience, 1983, 663 p.)

Smith, F. G. 1970, Monthly Notices of the RAS, 149, 1

Smits, J. M., Stappers, B. W., Edwards, R. T., Kuijpers, J., & Ramachandran, R. 2006, Astronomy and Astrophysics, 448, 1139

Staelin, D. H., Ewing, M. S., Price, R. M., & Sutton, J. M. 1970, Astrophysical Journal, Letters, 160, L7+

Staelin, D. H., & Reifenstein, E. C. 1968, Science, 162, 1481

Stinebring, D. R., Cordes, J. M., Rankin, J. M., Weisberg, J. M., & Boriakoff, V. 1984a, Astrophysical Journal, Supplement, 55, 247

Stinebring, D. R., Cordes, J. M., Weisberg, J. M., Rankin, J. M., & Boriakoff, V. 1984b, Astrophysical Journal, Supplement, 55, 279

Strohmayer, T. E. 1992, Astrophysical Journal, 388, 138

—. 1993, Astrophysical Journal, 417, 273

Strohmayer, T. E., Cordes, J. M., & van Horn, H. M. 1992, Astrophysical Journal, 389, 685

Sturrock, P. A. 1971, Astrophysical Journal, 164, 529

Suleymanova, S. A., Izvekova, V. A., Rankin, J. M., & Rathnasree, N. 1998, Journal of Astrophysics and Astronomy, 19, 1

Taylor, J. H., Hulse, R. A., Fowler, L. A., Gullahorn, G. E., & Rankin, J. M. 1976, Astrophysical Journal, Letters, 206, L53

Taylor, J. H., Manchester, R. N., & Huguenin, G. R. 1975, Astrophysical Journal, 195, 513

Tennant, A. F., Becker, W., Juda, M., Elsner, R. F., Kolodziejczak, J. J., Murray, S. S., O'Dell, S. L., Paerels, F., Swartz, D. A., Shibazaki, N., & Weisskopf, M. C. 2001, Astrophysical Journal, Letters, 554, L173

Terzian, Y., & Davidson, K. 1976, Astrophysics and Space Science, 44, 479

Thompson, D. J., Fichtel, C. E., Kniffen, D. A., & Ogelman, H. B. 1975, Astrophysical Journal, Letters, 200, L79

Thorne, K. S., & Ipser, J. R. 1968, Astrophysical Journal, Letters, 152, L71+

Thorsett, S. E. 1991, Astrophysical Journal, 377, 263

Thorsett, S. E., & Chakrabarty, D. 1999, Astrophysical Journal, 512, 288

Tsuruta, S., & Cameron, A. G. W. 1966, Nature, 211, 356

van Horn, H. M. 1980, Astrophysical Journal, 236, 899

van Kerkwijk, M. H., Clemens, J. C., & Wu, Y. 2000, Monthly Notices of the RAS, 314, 209

van Leeuwen, A. G. J., Kouwenhoven, M. L. A., Ramachandran, R., Rankin, J. M., & Stappers, B. W. 2002, Astronomy and Astrophysics, 387, 169

van Leeuwen, A. G. J., Stappers, B. W., Ramachandran, R., & Rankin, J. M. 2003, Astronomy and Astrophysics, 399, 223

Vivekanand, M., & Joshi, B. C. 1997, Astrophysical Journal, 477, 431

Wallace, P. T., Peterson, B. A., Murdin, P. G., Danziger, I. J., Manchester, R. N., Lyne, A. G., Goss, W. M., Smith, F. G., Disney, M. J., Hartley, K. F., Jones, D. H. P., & Wellgate, G. W. 1977, Nature, 266, 692

Weltevrede, P., Wright, G. A. E., & Stappers, B. W. 2007, Astronomy and Astrophysics, 467, 1163

Winget, D. E., van Horn, H. M., & Hansen, C. J. 1981, Astrophysical Journal,
    Letters, 245, L33

Woltjer, L. 1964, Astrophysical Journal, 140, 1309

Wright, G. A. E. 1981, Monthly Notices of the RAS, 196, 153

Wu, Y., & Goldreich, P. 2001, Astrophysical Journal, 546, 469

Xilouris, K. M., Kramer, M., Jessner, A., Wielebinski, R., & Timofeev, M. 1996,
    Astronomy and Astrophysics, 309, 481

Zheleznyakov, V. V. 1971, Astrophysics and Space Science, 13, 87